UNIVERSITY OF HELSINKI   REPORT SERIES IN PHYSICS

HU-P-D269

COMPUTATIONAL STUDIES ON CELLULOSE: PYROLYSIS, NANOSTRUCTURE AND HYDRODYNAMIC BEHAVIOUR

Antti Paajanen

Division of Materials Physics
Department of Physics
Faculty of Science
University of Helsinki
Helsinki, Finland

ACADEMIC DISSERTATION

To be presented for public discussion with the permission of the Faculty of Science of the University of Helsinki, in Auditorium PIII, Porthania, on the 25th of January, 2020 at 12 o'clock.

Helsinki 2020

Supervisors

Dr. Jukka Vaari
VTT Technical Research Centre of Finland Ltd
Espoo, Finland

Dr. Jukka Ketoja
VTT Technical Research Centre of Finland Ltd
Espoo, Finland

Pre-examiners

Prof. Eero Kontturi
Department of Bioproducts and Biosystems
Aalto University
Espoo, Finland

Dr. Jakob Wohlert
Department of Fibre and Polymer Technology
KTH Royal Institute of Technology
Stockholm, Sweden

Opponent

Dr. Yoshiharu Nishiyama
Centre de Recherches sur les Macromolécules Végétales
Centre National de la Recherche Scientifique
Grenoble, France

Custos

Prof. Kai Nordlund
Department of Physics
University of Helsinki
Helsinki, Finland

Preface

Several people have contributed to this work either directly or indirectly. I am grateful to my supervisors, Dr. Jukka Vaari and Dr. Jukka Ketoja, for their guidance and support throughout my postgraduate studies. It has been a privilege to work with and learn from them. I also want to acknowledge Prof. Kai Nordlund for his role as the responsible professor. His guidance during the later stages of this work was invaluable.

I am thankful to my co-authors and collaborators from VTT, Aalto University and Tampere University. I would especially like to thank Prof. Thaddeus Maloney for the pleasant collaboration that contributed two of the included publications.

I would like to acknowledge Prof. Eero Kontturi and Dr. Jakob Wohlert for their role as the pre-examiners of this thesis and for their valuable feedback.

I would like to express my gratitude to my colleagues at VTT for creating a warm and inspiring working environment. I especially want to thank Dr. Tuula Hakkarainen, who carefully read and commented on numerous versions of the manuscripts, always in a friendly and supportive manner. Warm thanks are also due to Dr. Topi Sikanen, Dr. Anna Matala, Mr. Tatu Pinomaa, Dr. Stefania Fortino, Dr. Sami Majaniemi, Dr. Tuukka Verho and Dr. Anssi Laukkanen. If it wasn't for the encouragement of Prof. Simo Hostikka, I might not have pursued postgraduate studies in the first place. I should not forget my fellow students from our undergraduate years either, Dr. Kirsi Svedström, Dr. Suvi Ikäläinen and Dr. Toni Viskari, who set a great example to follow.

Lastly, I want to thank my parents Oili and Risto, and my brother Niilo, for their constant support and encouragement. I am deeply grateful to my wife Jenni, whose love and patience during these years have been amazing. For all these things I am grateful to my Heavenly Father.

Helsinki, 6 January, 2020 *Antti Paajanen*

Abstract

Cellulose, the major component of plant matter, has a complex hierarchical structure that extends from the scale of cells down to the molecular level. Knowledge of the structural fundamentals of cellulose is relevant, not only for an understanding of plant life, but also for numerous technologies that use it as a raw material. The methods of computational physics are increasingly used to support experimental efforts in cellulose research. This thesis reports molecular and fluid dynamics simulations that address questions related to the pyrolytic degradation of cellulose and the aggregation and deaggregation of cellulose microfibrils.

Cellulose pyrolysis involves hundreds of chemical reactions and volatile products, the description of which remains a formidable challenge. Here, we demonstrate the use of reactive force field methods for predicting mechanisms and kinetics of cellulose pyrolysis. We show that reactive molecular dynamics simulations can reproduce essential features of the degradation process, most notably its onset via glycosidic bond cleavage, and thus offer a means to complement quantum chemistry methods and experimental analytics.

The aggregation of microfibrils is fundamental to the structural hierarchy of native cellulose and has direct implications for its processing into nanostructured forms. Here, we use atomistic simulations to elaborate on the effects of chemical modification on microfibril interactions. Our simulations reveal the sensitivity of the interaction to non-uniform substitution patterns, a feature that is not captured by continuous theoretical models. Our findings suggest a connection between uneven charge distribution and heterogeneity observed in disintegration experiments.

We also investigate the structure of microfibril bundles, and their relationship to the bound water of the cell wall, using molecular dynamics simulations. The simulations predict the spontaneous formation of a twisted ribbon-like bundle with a twist rate compatible with recent experimental evidence. This also leads to a reasonable prediction for the amount of bound water, which consists of molecular water layers surrounding the fibrils, along with several other experimental indicators.

Microfibril interactions also manifest themselves in the rheology of aqueous cellulose nanofibril suspensions. Here, we demonstrate the coordinated use of rheometry, printing experiments and computational fluid dynamics simulations in the development

of cellulose-based hydrogels for wound dressing applications. One of our key findings is the inadequacy of rotational rheometry as a basis for models of printer head flow, and the consequent need for an alternative model building strategy.

List of publications

This thesis is based on the following original publications, which are referred to in the text as **I**–**IV**.

I **Paajanen, A.**, and Vaari, J. (2017). High-temperature decomposition of the cellulose molecule: a stochastic molecular dynamics study. *Cellulose*, 24(7):2713–2725. DOI: 10.1007/s10570-017-1325-7

II **Paajanen, A.**, Sonavane, Y., Ignasiak, D., Ketoja, J. A., Maloney, T., and Paavilainen, S. (2016). Atomistic molecular dynamics simulations on the interaction of TEMPO-oxidized cellulose nanofibrils in water. *Cellulose*, 23(6):3449–3462. DOI: 10.1007/s10570-016-1076-x

III **Paajanen, A.**, Ceccherini, S., Maloney, T., and Ketoja, J. A. (2019). Chirality and bound water in the hierarchical cellulose structure. *Cellulose*, 26(10):5877–5892. DOI: 10.1007/s10570-019-02525-7

IV Leppiniemi, J., Lahtinen, P., **Paajanen, A.**, Mahlberg, R., Metsä-Kortelainen, S., Pinomaa, T., Pajari, H., Vikholm-Lundin, I., Pursula, P., and Hytönen, V. P. (2017). 3D-printable bioactivated nanocellulose-alginate hydrogels. *ACS Applied Materials & Interfaces*, 9(26):21959–21970. DOI: 10.1021/acsami.7b02756

Author's contribution

Publication I: High-temperature decomposition of the cellulose molecule: a stochastic molecular dynamics study

The author contributed to the design of the stochastic simulation approach and carried out the molecular dynamics simulations and the trajectory analyses. He developed most of the software tools used for post-processing. The author wrote the manuscript together with J. Vaari.

Publication II: Atomistic molecular dynamics simulations on the interaction of TEMPO-oxidized cellulose nanofibrils in water

The author carried out the molecular dynamics simulations and the trajectory analyses. He was responsible for the implementation of the electrostatic model for cellulose microfibril interactions and the related results. The author wrote the manuscript together with J. Ketoja, Y. Sonavane and T. Maloney.

Publication III: Chirality and bound water in the hierarchical cellulose structure

The author contributed to the design of the studied systems, developed the software tools for creating the atomistic models, and carried out the molecular dynamics simulations and the trajectory analyses. He also developed most of the software tools used for post-processing. The author wrote the manuscript together with J. Ketoja and T. Maloney.

Publication IV: 3D-printable bioactivated nanocellulose-alginate hydrogels

The author carried out the computational fluid dynamics simulations of the flow conditions within the printer head, contributed to the planning and analysis of the rheometry and 3D printing experiments, and wrote the associated parts of the manuscript. J. Leppiniemi, P. Lahtinen and the author contributed equally to the work.

Other related publications

List of publications that are relevant for this thesis but not included in it:

Vaari, J., and **Paajanen, A.** (2018). Evaluation of the reactive molecular dynamics method for research on flame retardants: ATH-filled polyethylene. *Computational Materials Science*, 153:103–112. DOI: 10.1016/j.commatsci.2018.06.032

Verho, T., **Paajanen, A.**, Vaari, J., and Laukkanen, A. (2018). Crystal growth in polyethylene by molecular dynamics: the crystal edge and lamellar thickness. *Macromolecules*, 51(13):4865–4873. DOI: 10.1021/acs.macromol.8b00857

Paajanen, A., Vaari, J., and Verho, T. (2019). Crystallisation of cross-linked polyethylene in molecular dynamics simulation. *Polymer*, 171:80–86.
DOI: 10.1016/j.polymer.2019.03.040

Contents

1   Introduction

Cellulose can be found everywhere in the natural and human environment. As a major component of plant matter, it contributes to the heat of combustion of firewood and the rigidity of wooden structures, and underlies the properties of plant-based textiles and paper. Since the late modern period, the uses of cellulose have become increasingly diverse. Chemical technologies have enabled, among others, the production of semi-synthetic fibres from regenerated cellulose (Wang et al., 2016) and the conversion of lignocellulosic biomass into commodity chemicals, including transportation fuels (Huber et al., 2006). Cellulose nanomaterials have emerged as a potential platform for a range of high-technology applications from medical implants to printed electronics. (Thomas et al., 2018) Cellulose is abundantly available, renewable, recyclable and biodegradable, and thus a potential raw material for a sustainable society.

Cellulose is a linear homopolysaccharide composed of repeating anhydroglucose units. It is found in the cell wall, a structural layer that provides plant cells with mechanical support and structural integrity and regulates their growth. (Lampugnani et al., 2018) Cellulose forms fibrous aggregates, known as microfibrils, that are intertwined with a family of other polysaccharides and—in the case of secondary cell walls—lignins. Together, they form a hierarchical structure that extends from the scale of the cells down to the molecular level. (Gibson, 2012) The cell wall construction is remarkably diverse. The dimensions and the arrangement of the microfibrils, the chemical identity of the non-cellulosic polysaccharides and the lignins, and their relative amounts vary depending on the species, the plant, and the individual cell. (Burton et al., 2010).

The discovery of cellulose began in the mid-1800s, when it was first isolated from plant tissue. (Payen, 1838) Its polymeric nature was discovered later, in the early 1900s. (Staudinger, 1920) Since then, continued research efforts have contributed to an understanding of cellulose biosynthesis (McNamara et al., 2015) and the formation of microfibrils and their assemblies within the cell wall (Jarvis, 2018). Despite the progress, knowledge of the nanoscale structure of cellulose, and its interactions with the other cell wall polymers, is still incomplete. (Cosgrove, 2018b; Lampugnani et al., 2018). Such details are relevant, not only for an understanding of plant life, but also for numerous technologies that rely on cellulose as a raw material. The recent interest in cellulose nanomaterials has motivated new efforts to understand the nanoscale structure of both native and processed forms of cellulose.

The methods of computational physics and chemistry have found increasing use in cellulose research over the past two decades. Particularly, the availability of detailed crystallographic information on native cellulose (Nishiyama et al., 2002, 2003b), carbohydrate force fields (Foley et al., 2012) and high-performance computing facilities have enabled atomistic simulations of cellulose microfibrils and their assemblies. Structural details reachable with modern electron and scanning probe microscopy can now be stud-

ied, among others, using molecular dynamics (MD) simulations. The majority of the modelling efforts have focused on individual microfibrils. This includes, among others, studies on their internal structure and morphology, mechanical properties, enzymatic degradation and dissolution in ionic liquids. At the same time, the development of reactive force field methods, including the ReaxFF (Van Duin et al., 2001) and AIR-EBO (Stuart et al., 2000) force fields, have enabled the simulation of reactive processes. Here, the few existing studies on cellulose have focused on its pyrolytic and radiolytic degradation.

This thesis reports computational studies on fundamental structural and thermochemical properties of cellulose. The work covers the structural hierarchy of native cellulose, with simulations on individual chains, microfibrils, microfibril bundles and bundle networks. The findings contribute to our understanding of the pyrolytic degradation of cellulose, its nanoscale structure, its chemical modification and the rheology of aqueous cellulose nanofibril (CNF) suspensions.

2 Purpose and structure

This thesis reports MD simulations and computational fluid dynamics (CFD) simulations on fundamental structural and thermochemical properties of cellulose. The research involves two themes: the pyrolytic degradation of cellulose, and the aggregation and deaggregation of cellulose microfibrils.

Cellulose pyrolysis underlies the combustion of lignocellulosic biomass—the burning of wood being the archetypal example—and is utilised in thermochemical conversion technologies. (Dhyani and Bhaskar, 2018) Here, our goal was to evaluate the capability of ReaxFF-MD simulations (Van Duin et al., 2001) to predict details of the pyrolysis chemistry. For this purpose, we carried out thermal decomposition simulations of cellulose molecules, gathered statistics of the primary reactions, and made predictions of the associated kinetics. Our results demonstrate the potential value of ReaxFF-MD as a computational tool in cellulose pyrolysis research.

The aggregation and deaggregation behaviour of microfibrils is fundamental to the structural hierarchy of native cellulose. (Cosgrove, 2018a) It also has direct implications for the processing of cellulose into nanostructured forms, and for the colloidal stability and rheology of aqueous CNF suspensions. (Fukuzumi et al., 2014) Here, our goal was to gain detailed information on microfibril interactions, the structure of their aggregates, and how these are reflected in the macroscopic properties of cellulosic materials. For this purpose, we carried out classical MD simulations to study the aggregation and deaggregation energetics of native and carboxylated microfibrils, and the structural consequences of aggregation. Our results suggest interesting links between molecular-level disorder, supramolecular assembly and bound water, and are compatible with a surprising number of experimental observations. In addition, we carried out CFD simulations to study the flow behaviour of CNF-based hydrogels in an additive manufacturing process. The results highlight the sensitivity of the flow behaviour to the rheological description, and the need for advanced rheological characterisation to build reliable models.

This thesis consists of an introductory part and four publications. The publications are briefly summarised in this chapter. Chapter 3 discusses cellulose: its natural sources, its molecular and supramolecular structure, and its technological significance. Chapter 4 reviews the used computational methods, and Chapter 5 the main findings. Finally, Chapter 6 presents the conclusions.

2.1   Summaries of the original publications

Publication I: High-temperature decomposition of the cellulose molecule: a stochastic molecular dynamics study

Paajanen, A., and Vaari, J. (2017). *Cellulose* 24(7):2713–2725.

We studied the thermal decomposition of individual cellulose chains using reactive molecular dynamics simulations. We observed that the decomposition usually begins with random cleavage of the glycosidic linkages, and that the associated kinetic parameters are compatible with those obtained from global mass loss measurements of cellulose pyrolysis. Moreover, we observed the formation of several low molecular weight products that are characteristic of cellulose pyrolysis. The broad agreement between our observations and the experimental literature supports further use of reactive molecular dynamics simulation in cellulose pyrolysis research.

Publication II: Atomistic molecular dynamics simulations on the interaction of TEMPO-oxidized cellulose nanofibrils in water

Paajanen, A., Sonavane, Y., Ignasiak, D., Ketoja, J. A., Maloney, T., and Paavilainen, S. (2016). *Cellulose* 23(6):3449–3462.

We used classical molecular dynamics simulations to study the aggregation and deaggregation energetics of carboxylated cellulose microfibrils at different functionalisation levels. We observed a correspondence between the averaged interaction strength and the experimental disintegration energy of TEMPO-oxidised cellulosic fibres. Moreover, we found that the interaction strength is highly sensitive to the carboxylate group distribution. This suggests heterogeneity in the behaviour of experimental systems and could explain the wide fibril size distribution observed at intermediate functionalisation levels.

Publication III: Chirality and bound water in the hierarchical cellulose structure

Paajanen, A., Ceccherini, S., Maloney, T., and Ketoja, J. A. (2019). *Cellulose* 26(10):5877–5892.

We used classical molecular dynamics simulations to study the structure of microfibril bundles and their relationship to the bound water of the cell wall. Our simulations reproduce several experimentally known features of native cellulose, including the mass fractions of bound water, the fraction of water-accessible hydroxyl groups, the specific surface area, and the conformational disorder of surface and surface-bound chains. The simulations demonstrate the chirality transfer between microfibrils and their bundles

and give reasonable predictions for the corresponding twist rates. Mismatch in the twist rates prevents co-crystallisation and leads to repeated openings along the bundle. Such openings could become initiation sites of defects during chemical and mechanical processing.

Publication IV: 3D-printable bioactivated nanocellulose-alginate hydrogels

Leppiniemi, J., Lahtinen, P., Paajanen, A., Mahlberg, R., Metsä-Kortelainen, S., Pinomaa, T., Pajari, H., Vikholm-Lundin, I., Pursula, P., and Hytönen, V. P. (2017). *ACS Applied Materials & Interfaces* 9(26):21959–21970.

We developed a 3D-printable cellulose-alginate hydrogel targeted for wound dressing applications. After benchmarking several bio-based hydrogel candidates, we found a formulation that exhibits excellent printability and dimensional stability, has mechanical properties that suggest tissue compatibility, absorbs moisture, and can be functionalised with avidin. The formulation includes alginate, TEMPO-oxidised CNFs, glycerin and water. The benchmarking involved rheometry, buffer and conditioning tests, compression measurements and printing trials, among others. In addition to the experiments, we used CFD simulations to study the hydrogel's behaviour within the printer head and during the subsequent deposition process.

3   Cellulose

Cellulose is a major component of plants. It is found in the cell wall, a structural layer that provides plant cells with mechanical support and structural integrity and regulates their growth. (Lampugnani et al., 2018) Cellulose has a complex hierarchical structure that extends from the scale of the cells down to the molecular level. This chapter reviews the structure of cellulose as found in wood, its most important commercial source. Besides the discussion on native cellulose, a brief overview is given on technologically important micro and nanostructured forms.

3.1   Wood cells

Wood cells are formed in the vascular cambium, which is a thin sheath of meristematic cells located between the inner bark (phloem) and the wood (secondary xylem). (Wiedenhoeft, 2013) There are several types of wood cells, each with their characteristic size, shape, pit structure[1] and function. The cells are, in general, elongated and oriented in two systems: (i) the axial system, with cells aligned parallel to the stem axis, and (ii) the radial system, with cells aligned perpendicular to the stem axis. Wood from gymnosperm trees, also known as softwood, consists of tracheids and parenchyma cells of both systems. The tracheids provide mechanical support and form a water-conducting tissue, whereas the parenchyma cells synthesise, store and transport vital biochemicals. Wood from angiosperm trees, also known as hardwood, is more diverse, as its axial system additionally consists of fibres[2] and vessel elements. The fibres provide mechanical support, whereas the vessel elements specialise in conducting water.

Like all eukaryotic cells, wood cells consist of a cell cavity that hosts the cytoplasm and the nucleus, and the surrounding cell membrane. The cell membrane is surrounded by the cell wall, a structural layer that goes through several stages of development during cell growth. At functional maturity, most wood cells lose their nucleus and cytoplasm, and leave behind an empty cell cavity (the lumen) and the cell wall. (Bollhöner et al., 2012) The cell wall thus accounts for the ultimate function of most wood cells. Despite variations in the size, shape, pit structure and function of the cells, the cell wall composition and architecture are fairly regular.

The cell wall is made of four primary components: cellulose, hemicelluloses, pectins and lignins. (Lampugnani et al., 2018) Cellulose, hemicelluloses and pectins are polysaccharides—polymeric carbohydrate molecules composed of simple sugar units. Lignins are a class of complex phenolic heteropolymers. Cellulose is the major component of the cell wall. For example, in softwood tracheids, the cell wall consists of roughly

---

[1]Pits are openings in the secondary cell wall that enable, among others, the transport of water between adjacent cells.

[2]In the forest industries, the term *fibre* is used to refer to any fibrous element extracted from wood. To avoid confusion, the term *cellulosic fibre* will be used for this purpose.

25–50 wt% cellulose, 20–30 wt% hemicelluloses, 20–30 wt% lignins, and trace amounts of pectins. (Marriott et al., 2016)

Cellulose is found in fibrous aggregates, known as microfibrils[3], which are the structural reinforcement units of the cell wall. (Cosgrove, 2005) The non-cellulosic polysaccharides are closely associated with the microfibrils. Together, they form a complex network that is further impregnated with lignin, which strengthens the cell wall and makes it less permeable to water. It should be noted, that the detailed organisation of the cell wall polymers, and their interactions, are not fully understood. (Cosgrove, 2018b; Lampugnani et al., 2018) Moreover, the dimensions and the arrangement of the microfibrils, the chemical identity of the non-cellulosic polysaccharides and the lignins, and their relative amounts vary depending on the species, the plant, and the individual cell. (Burton et al., 2010)

The cell wall consists of layers, distinguishable by their chemical composition and the orientation of the microfibrils (see Figure 1). (Asikainen, 2015; Donaldson, 2008; Gibson, 2012) The cell wall is surrounded by the middle lamella, a thin interfacial layer that glues adjacent cells to each other. It consists mostly of lignins and pectins. The outermost layer of the cell wall, called the primary cell wall, is formed during cell expansion. It is thin, and consists mostly of lignins and hemicelluloses, along with a sparse network of randomly oriented microfibrils. In softwood tracheids, the primary cell wall consists of roughly 15 wt% cellulose.

Moving towards the cell cavity, the next layer is called the secondary cell wall. It is formed within the primary wall after cell expansion has ended. The secondary wall is much thicker than the primary wall and consists mostly of cellulose. The microfibrils are aligned and form thin lamellae that wind around the cell axis. The angle between the cell axis and that of the microfibrils is called the microfibril angle. The secondary cell wall has three sub-layers, denoted S1, S2 and S3, which can be distinguished by their microfibril angle. The S1, or outer, layer is thin and contains several transversely oriented microfibril lamellae. In softwood tracheids, the S1 layer consists of roughly 30 wt% cellulose. The S2, or middle, layer is considerably thicker, and accounts for most of the cell wall (up to 90 wt%). It contains tens of axially oriented microfibril lamellae. In softwood tracheids, the S2 layer consists of roughly 45 wt% cellulose. The S3, or inner, layer is thin and contains several transversely oriented microfibril lamellae. In softwood tracheids, the S3 layer consists of roughly 45 wt% cellulose. The cell wall layers do not have sharp boundaries, and the transitions between them are gradual. Pulping processes, which are used to extract cellulosic fibres from wood, often remove the outer P and S1 layers. (Niskanen, 2008) The S2 layer thus becomes even more dominant and determines the properties of cellulosic fibres.

---

[3]The term *elementary fibril* is used in the context of cellulose nanomaterials. (ISO/TS 20477:2017, 2017)
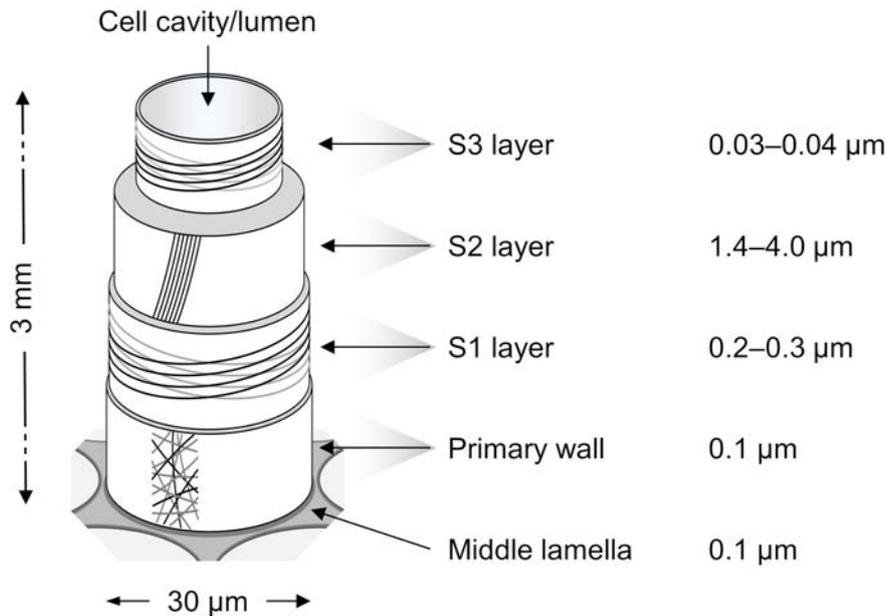
Figure 1. Structural elements of a wood cell, excluding pits: the middle lamella (M); the primary cell wall (P); and the outer (S1), middle (S2) and inner (S3) layers of the secondary cell wall. The orientation of cellulose microfibrils within each layer is indicated by the black lines. Characteristic dimensions are shown for a spruce tracheid. (Asikainen, 2015) Following the description given in (Gibson, 2012).

3.2   Molecular structure

Cellulose is synthesised at the cell membrane by the cellulose synthase complex (CSC). (McFarlane et al., 2014; McNamara et al., 2015) In vascular plants, the CSC consists of six cellulose synthase (CESA) subunits, arranged in a hexameric rosette. The CESA proteins assemble cellulose chains from uridine diphosphate glucose, and secrete them across the cell membrane. The resulting polymer is a linear chain of β-$(1 \rightarrow 4)$-linked D-glucopyranosyl units (i.e. anhydroglucose units, hereafter referred to as glucose units; see Figure 2). (French, 2017) The β-$(1 \rightarrow 4)$ glycosidic bonds link the C1 of one repeat unit to the C4 of the next, with consecutive units adopting a ribbon-like, twofold helical screw conformation.

   Cellulose is non-uniform with respect to molecular weight. (Brett, 2000) Moreover, its average molecular weight depends on the biological origin. (Hallac and Ragauskas, 2011) Determining the degree of polymerisation (DP) of native cellulose is not straight-forward, as the required isolation treatments may result in chain degradation. For wood cellulose, typically reported DPs range from several thousands to ten thousand, corresponding to chain lengths from hundreds of nanometers to micrometers. (Zugenmaier, 2008) In general, when cellulose is extracted from plant matter, its average DP tends
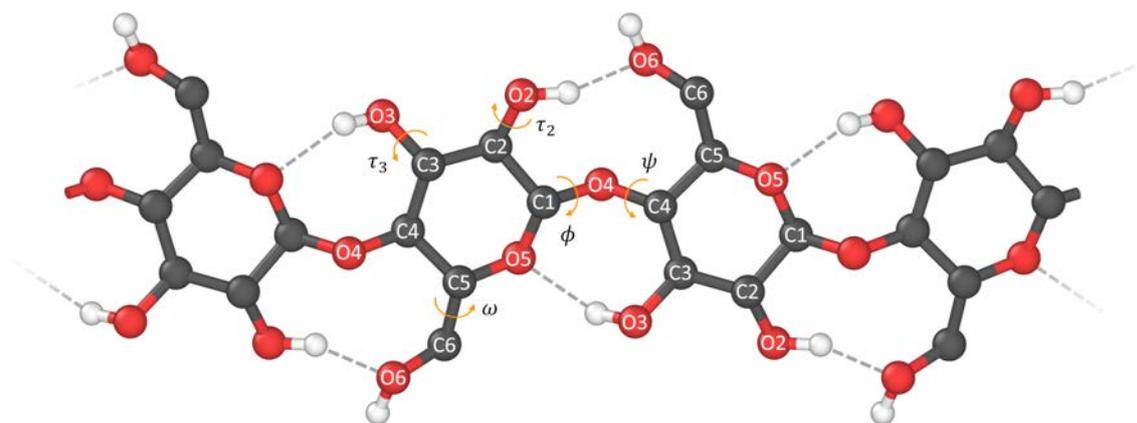
Figure 2. Ball-and-stick representation of a cellulose molecule with pyranose ring hydrogens implied. The conformation of the glycosidic bond is defined by the torsional angles ϕ and ψ, that of the primary alcohol group by the angle ω, and those of the secondary alcohol groups by the angles τ_1 and τ_2. The intramolecular hydrogen bonds O3–H$\cdots$O5 and O2–H$\cdots$O6 are indicated by dashed lines.

to decrease. The extent depends on the applied chemical and mechanical treatment. For wood pulp, typically reported DPs range from several hundreds to two thousand, corresponding to chain lengths of hundreds of nanometers.

Each glucose unit has three alcohol groups: a primary group at C6 and two secondary groups at C2 and C3. The pyranose ring adopts the energetically favourable $^4C_1$-chair conformation, which has the hydroxyl groups positioned equatorially and the carbon-hydrogen bonds axially. (Buchanan et al., 2015) The positioning of the hydroxyl groups has important consequences for intra and intermolecular hydrogen bonding, and the chemical reactivity of cellulose.

The orientation of the primary alcohol group is particularly important, as it controls the pattern of hydrogen bonding. (Nishiyama et al., 2002) Its conformation about the C5–C6 bond can be denoted by a two-letter combination that indicates the O6–O5 and O6–C4 torsional angles. Angles below 30° are referred to as *cis* (c), angles between 30° and 150° as *gauche* (g), and angles above 150° as *trans* (t). Figure 2 shows the primary alcohol groups in the *trans-gauche* (tg) conformation[4].

Each glucose unit forms two hydrogen bonds with its neighbours. The C3 hydroxyl acts as a hydrogen bond donor to the pyranose ring oxygen (O5) of the previous unit. The C2 hydroxyl pairs with the C6 hydroxyl of the following unit, and acts either as a donor or an acceptor. Similarly, the C6 hydroxyl pairs with the C2 hydroxyl of the previous unit. The intramolecular hydrogen bonds stabilise the glycosidic linkages, promoting an extended, ribbon-like, conformation. The C3 hydroxyl is occupied as an

---

[4]That is, the O6–O5 torsional angle is between 150° and 180°, or −150° and −180°, and the O6–C4 torsional angle is between 30° and 150°, or −30° and −150°.

intramolecular hydrogen bond donor, whereas the C2 and C6 hydroxyls act as donors both in intra and intermolecular hydrogen bonds. Since cellulose is linear, favours an extended conformation, and has the capability to form intermolecular hydrogen bonds, it tends to form fibrillar aggregates and crystalline forms. (Nishiyama, 2018)

The alcohol groups are also central to the chemical reactivity of cellulose. From a technological viewpoint, they enable numerous routes for chemical modification. Indeed, a host of cellulose derivatives have been developed over the years. (Heinze et al., 2018; Klemm et al., 2005) Cellulose acetate, in which part of the alcohol groups are acetylated, is both a historical example and a derivative still in use. It is, among others, spun into fibres and used in textile applications. (Law, 2004) The primary and secondary alcohol groups can have different roles according to their accessibility and characteristic reactions. Some reactions are selective. For example, 2,2,6,6-tetramethyl-piperidine 1-oxyl (TEMPO) mediated oxidation targets the primary alcohol groups (Saito and Isogai, 2004) and results in negatively charged carboxylate groups on the treated cellulose surfaces. The oxidative treatment is used, among others, to facilitate the deconstruction of cellulosic fibres into micro and nanostructured forms. (Moon et al., 2011) Nanostructured forms of TEMPO-oxidised cellulose, and their aqueous suspensions, are discussed in **Publications II** and **IV**.

The cellulose molecule has chemically distinct ends. During biosynthesis, condensative polymerisation locks the glucose units in the β-configuration—except for one terminal unit. (Buchanan et al., 2015) This unit has a hemiacetal group at C1, and it can thus undergo mutarotation between the α and β anomeric forms. The aldehyde group that is revealed in the process makes this terminal unit a reducing sugar, and it is correspondingly called the reducing end. The other end has a hydroxyl group at C4, and it is called the non-reducing end. The distinct ends are of minor importance for most chemical modification schemes. (Heinze et al., 2018) They do, however, have a role in both enzymatic (Payne et al., 2015) and pyrolytic degradation processes (Leng et al., 2018; Matsuoka et al., 2011). The latter are discussed in **Publication I**.

3.3   Supramolecular structure

Biosynthesis determines both the molecular and the supramolecular structure of cellulose. Immediately following their synthesis, the cellulose chains associate to form microfibrils, the elementary units of native cellulose (see Figure 3). (McFarlane et al., 2014) The six CESA subunits are believed to consist of three CESA proteins each, which suggests that the microfibrils are synthesised with 18 constituent chains.[5] (Nixon et al., 2016; Vandavasi et al., 2016) There are, however, small-angle neutron scattering (SANS), wide-angle X-ray scattering (WAXS) and solid-state nuclear magnetic

---

[5]Subunits of six CESA proteins have been proposed earlier (Herth, 1983), but this model has since been questioned on several grounds (Cosgrove, 2014; Nixon et al., 2016).
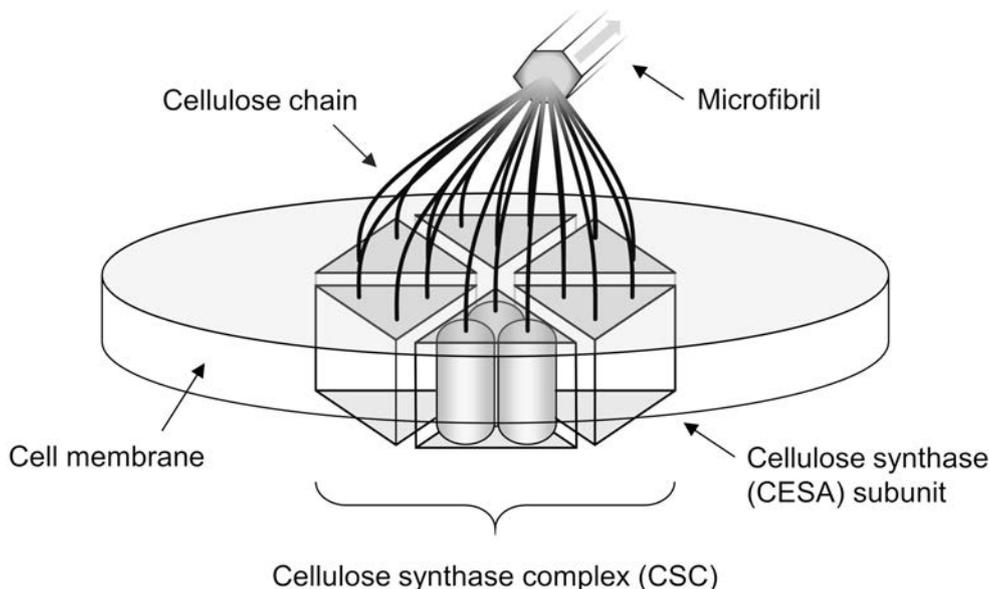
Figure 3. Schematic of a rosette CSC with 18 CESAs. The newly formed cellulose chains associate into a microfibril that lies in the plane of the cell membrane. Following the description given in (Jarvis, 2013).

resonance (NMR) spectroscopy studies that suggest slightly larger microfibrils of 24 constituent chains. (Fernandes et al., 2011; Thomas et al., 2013; Wang and Hong, 2016) Partial fusion of the microfibrils, and the accretion of hemicelluloses on their surfaces, could explain the observed variability in size. (Jarvis, 2018) Microfibrils of 18–24 chains have diameters of circa 3 nm. In contrast, their axial dimensions can be of the order of micrometres. (Moon et al., 2011)

Crystalline and disordered forms of cellulose have been shown to co-exist along the length of a microfibril. (Jarvis, 2018) Estimates of their relative abundance are, to some degree, dependent on the used measurement technique. (Himmel et al., 2010) For example, NMR spectroscopy measurements, which are sensitive to the chain conformations, indicate that 30–40 % of the cellulose in spruce wood has a flat ribbon conformation and primary alcohol groups in the tg conformation. (Fernandes et al., 2011) Both of these are characteristic of the crystalline allomorphs of native cellulose. Besides the lateral disorder, a certain amount of axial disorder exists. (Bondeson et al., 2006; Hidayat et al., 2012; Usov et al., 2015) This could be, among others, due to chain-end defects, naturally occurring kinks in the microfibrils, or ones caused by mechanical processing. However, their contribution to the molecular-level disorder is minor. (Nishiyama et al., 2003a)

Information on the cross-sectional shape of plant cellulose microfibrils, and the vari-

ation thereof, is limited. (Jarvis, 2018) The shape is consequential, as it determines the types of exposed faces and their relative abundance. These, in turn, affect the microfibrils' interactions with each other, the other cell wall polymers, and water. (Grantham et al., 2017; Oehme et al., 2015) Microfibrils of plant cellulose are expected to have both hydrophilic and hydrophobic faces, which expose the equatorial hydroxyl groups and the axial hydrogens of the pyranose rings, respectively. (Cosgrove, 2018b) Evidence for this comes from their interaction with fungal enzymes, whose carbohydrate binding modules are known to bind to the hydrophobic faces of algal cellulose microfibrils. (Lehtiö et al., 2003)

Microfibrils of wood cellulose form aggregates, sometimes referred to as macrofibrils. (Donaldson, 2007) The aggregates come in many sizes, but, in general, smaller ones are more common than larger ones. (Fahlén and Salmén, 2003; Zhang et al., 2016b) For example, in their atomic force microscopy (AFM) study, Fahlen and Salmen report an average diameter of 15–20 nm for microfibril aggregates in spruce wood. (Fahlén and Salmén, 2003, 2005) In contrast, the largest aggregates they report are more than 40 nm in diameter. SANS experiments indicate that the microfibril spacing (centre-to-centre distance) within the aggregates is comparable to the microfibril diameter. (Fernandes et al., 2011) This implies at least some direct contact between the fibrils. Moreover, the spacing widens with increasing moisture content, which suggests that at least some water can penetrate into the aggregates. Lastly, the non-cellulosic polysaccharides— hemicelluloses and pectins—are known to interact with, and bind to, the microfibrils. (Cosgrove, 2018b) However, their spatial arrangement in relation to the microfibrils remains unclear, as do the details of their interactions. Bound hemicelluloses could interfere with the aggregation of microfibrils by preventing direct contacts, and thus, co-crystallisation. They could also facilitate interactions with lignins. (Grantham et al., 2017)

3.4 Crystalline forms

Crystalline cellulose has several allomorphs, including I_α, I_β, II, III_I and III_{II}. (Zugenmaier, 2008) Two of these, cellulose I_α and I_β, account for the naturally occurring cellulose, whereas the others are semisynthetic. The I_α and I_β allomorphs are known to co-exist, not only within individual plants, but also within individual microfibrils. (Jarvis, 2018) Their proportions depend on the origin, with cellulose I_α dominant in algae and bacterial cellulose, and cellulose I_β in vascular plants and tunicates. (Moon et al., 2011)

In both cellulose I allomorphs, the chains are parallel and form hydrogen-bonded layers that are stacked on top of each other. The main difference between the allomorphs I_α and I_β lies in the stacking of these layers. Figure 4 shows the crystal structure of cellulose I_β, and the primary intralayer hydrogen bonding pattern, as reported by
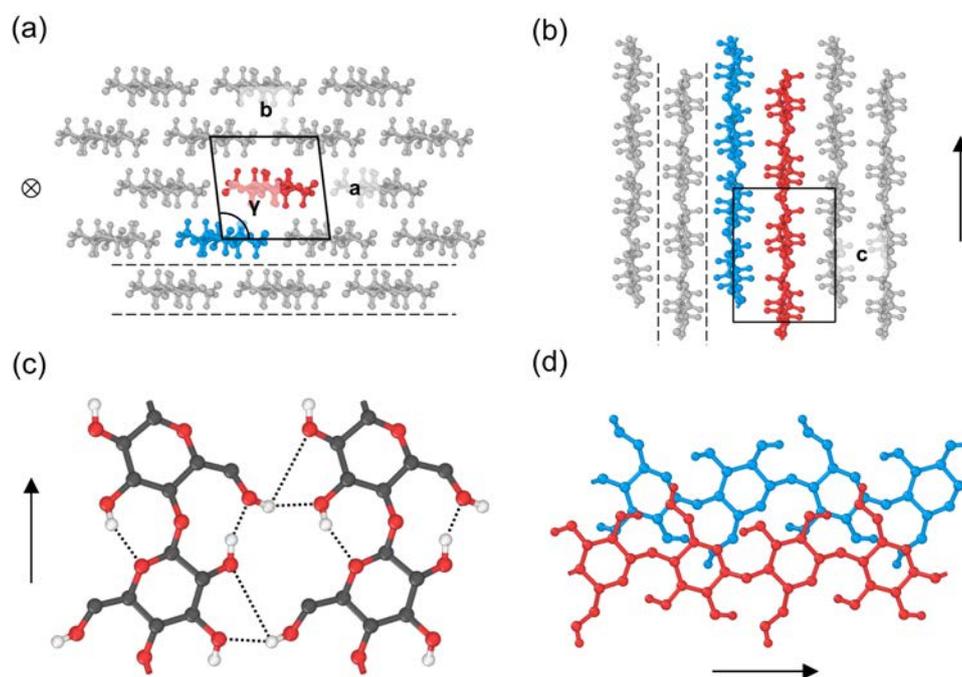
Figure 4. Cellulose I$_\beta$ crystal structure from different viewpoints: (a) along the chain axis, viewed from the non-reducing end; (b) perpendicular to the chain axis, viewed along the hydrogen-bonded layers; (c) one of the two intralayer hydrogen bonding patterns proposed by Nishiyama et al. (Nishiyama et al., 2008), indicated by the dashed lines; and (d) staggering of origin and centre chains, and their hydrogen-bonded layers. The black parallelogram indicates the unit cell, and the arrows point along the chain axis towards the reducing end. Origin and centre chains are indicated by blue and red colouring, respectively. The values of the lattice constants are: $a = 7.784$ Å, $b = 8.201$ Å, $c = 10.38$ Å and $\gamma = 96.55°$.

Nishiyama et al. (Nishiyama et al., 2002, 2008) The unit cell is monoclinic and contains two cellobiose units, referred to as the origin and centre chain according to their location within the unit cell. The intramolecular hydrogen bonds occur as discussed previously. The primary and secondary alcohol groups at C6 and C2, respectively, act as donors in the intermolecular hydrogen bonds. The research carried out in this thesis focuses on native cellulose, and the cellulose I$_\beta$ allomorph is used as a basis for the molecular models.

3.5   Cellulose micro and nanomaterials

The previous sections covered the structure and chemical environment of native cellulose, as found in the cell wall. In technological applications, the hierarchical structure of the cell wall is disintegrated to varying extent to obtain a desired functionality. For example, in the pulping process, cellulosic fibres are separated from pulpwood by

mechanical or chemical means. The resulting pulp is then used to produce paper or paperboard, or other products that are based on the characteristic properties of the fibres. Some processes, such as chemical pulping, also involve the partial removal of the other cell wall polymers.

Cellulosic fibres can be further processed into cellulose micro and nanomaterials. (Kargarzadeh et al., 2018) Their production, which can involve mechanical, chemical and enzymatic treatments, deconstructs the microfibril lamellae of the cell wall into microfibril aggregates, the aggregates into individual microfibrils, and involves, in some cases, the degradation of non-crystalline domains within the microfibrils. Cellulose micromaterials include, most notably, cellulose microcrystals (CMC). Cellulose nanomaterials are classified into two main categories: (i) cellulose nano-objects, and (ii) nanostructured cellulose (see Figure 5). (ISO/TS 20477:2017, 2017) Cellulose nano-objects include cellulose nanofibrils (CNF) and cellulose nanocrystals (CNC). Nanostructured cellulose refers to materials that have an internal or surface nanostructure predominantly composed of cellulose. The characteristic features of CNCs and CNFs are summarised below, following Moon et al. (Moon et al., 2011) and the standard terms and definitions given in (ISO/TS 20477:2017, 2017).

CNFs are fibrous nano-objects composed of at least one cellulose microfibril. They typically have diameters of 3–100 nm, and lengths up to several µm. Their aspect ratio is usually greater than 10. CNFs may be bifurcated, entangled and contain mesh-like structures. They are typically produced by mechanical fibrillation of purified cellulosic fibres. Depending on the production route, CNFs may also contain hemicelluloses, and even lignins. CNFs contain both crystalline and disordered forms of cellulose.

CNCs are rod-like nano-objects composed of at least one cellulose microfibril, or a segment thereof. They typically have diameters of 3–50 nm, and lengths from 100 nm to several µm. Their aspect ratio is usually between 5 and 50. CNCs do not exhibit bifurcations, entanglements or mesh-like structures. They are typically produced by acid hydrolysis of cellulosic fibres, or one of the other forms of cellulose nanomaterials. CNCs consist predominantly of crystalline cellulose.

Cellulose nanomaterials inherit many of the attractive features of cellulosic fibres, including their stiffness and specific strength, hydrophilicity, and capacity for chemical modification. (Klemm et al., 2005) They are renewable, recyclable and biodegradable, and considered to be broadly biocompatible. (Lin and Dufresne, 2014) They also have qualities that distinguish them from the traditional cellulosic materials. It is these qualities that make cellulose nanomaterials promising for high-technology applications, beyond the traditional uses of cellulose.

Cellulose micromaterials are already established in commercial use. They find use, among others, as emulsifiers and bulking agents in the food, pharmaceutical and cosmetics industries. Cellulose nanomaterials, on the other hand, mostly belong to emerging technologies. During the last decade, research and development efforts have in-
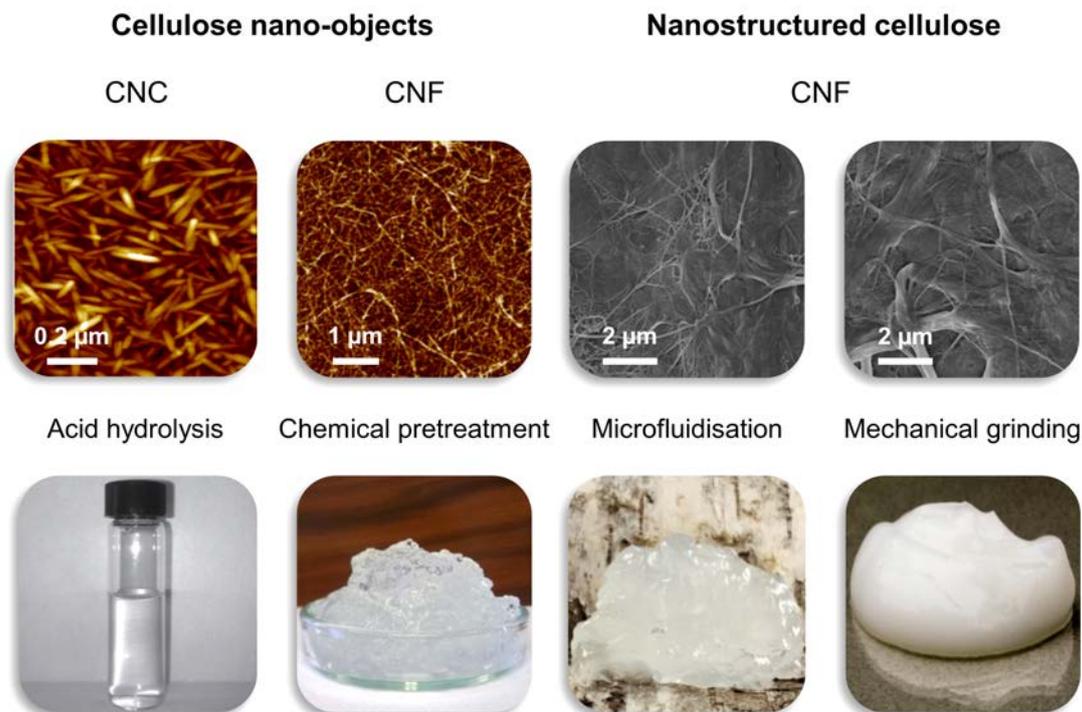
Figure 5. AFM and scanning electron microscopy (SEM) micrographs of plant-based cellulose nanomaterials, along with photographs of macroscopic samples. From left to right: cellulose nanocrystals, cellulose nanofibrils and nanostructured cellulose. Image courtesy of VTT Technical Research Centre of Finland Ltd.

creased substantially, and commercial impact is emerging. (Miller and Bodart, 2014) Among others, the following uses have been envisioned. CNFs have been considered as reinforcing agents in paper and paperboard production (Lengowski et al., 2019) and in polymer composites (Kargarzadeh et al., 2017); as barrier films in packaging applications (Hubbe et al., 2017); as industrial rheology modifiers (Sun et al., 2016); and as substrates for printed electronics (Hoeng et al., 2016). CNCs have been considered as reinforcing agents in polymer composites (Habibi et al., 2010); as barrier coatings (Chowdhury et al., 2019); and as moisture absorption modifiers in textiles (Zaman et al., 2013). Besides the above-mentioned, a variety of uses have been proposed in the field of biomedicine. (Jorfi and Foster, 2015; Lin and Dufresne, 2014) These include, among others, use in medical implants, tissue scaffolds for cell culture, excipients for drug delivery, antimicrobial materials, and materials for tissue repair, regeneration and healing. The use of CNF-based hydrogels (De France et al., 2017) in wound-healing applications are further discussed in **Publication IV**.

4 Computational methods

This chapter reviews the computational methods used in **Publications I–IV**. The first section introduces MD simulation, the primary computational tool in **Publications I–III**. The following sections elaborate on molecular force fields, simulation set-up and the analysis of molecular trajectories. Finally, the last section introduces CFD simulation, the primary computational tool in **Publication IV**.

4.1 Molecular dynamics simulation

MD simulation is a computer simulation technique for solving the time evolution of an atomistic system. The technique relies on three major approximations. Firstly, the atomic nuclei are treated as point-like particles that move according to the classical equations of motion. Secondly, the (ground state) potential energy of the system is assumed to depend only on the relative positions of the nuclei.[6] Lastly, the electrons and their motions are omitted, and the interatomic forces are described using an empirical potential energy function. From an algorithmic viewpoint, the technique can be summarised as follows:

(i) Set the initial positions and velocities of the atoms.

(ii) Calculate the interatomic forces.

(iii) Solve the equations of motion over a time step.

Repeated iteration of steps (ii) and (iii) reproduces the time-evolution of the system, its trajectory. Various structural and thermodynamic properties can be determined by analysing the generated sequence of atom positions and momenta. A practical algorithm involves several additional steps and considerations. The most important ones are discussed below. For further details, see, for example (Allen and Tildesley, 1987; Frenkel and Smit, 2002; Leach, 2001; Schlick, 2010).

    Initial configuration. The initial positions of the atoms are set to describe a structure of interest. For example, in simulations of crystalline solids, the positions can be set according to an experimentally determined crystal structure. Most often, the initial configuration is a combination of experimental and theoretical considerations. In **Publications II** and **III**, the internal structure of the cellulose microfibrils was based on the cellulose I$_\beta$ crystal structure (see Chapter 3, Section 3.4: Crystalline forms), whereas their cross-sectional shape and number of constituent chains were based on evidence from several sources (see Chapter 3, Section 3.3: Supramolecular structure). The initial velocities are either (i) sampled randomly from the Maxwell-Boltzmann distribution to represent thermal motion, or (ii) in non-equilibrium simulations, set

---

[6]This is the Born-Oppenheimer approximation (Born and Oppenheimer, 1927).

to reproduce collective motion, for example, to simulate molecular collisions. The atoms are contained within a simulation domain that has the shape of a space-filling polyhedron, often a rectangular cuboid. The domain can be made periodic in one or more dimensions to eliminate boundary effects and thus mimic a macroscopic system.

Interatomic forces. The interatomic forces are obtained as the negative gradient of an empirical potential energy function. Such potentials have been developed for different types of systems, including metallic, ionic and covalent solids, as well as organic and inorganic molecules. (Harrison et al., 2018) Interatomic potentials that describe molecular systems are referred to as force fields. They have the characteristic feature that the potential energy expression can be written as a sum of terms that describe local (covalent, intramolecular) and non-local (non-covalent, intra and intermolecular) interactions. The local terms act on pre-defined molecular topologies, whereas the non-local terms act between all atoms. The number of non-local interactions grows dramatically with the number of atoms. For this reason, they are usually described by an effective pair potential that ignores explicit many-body effects.[7] Moreover, the force calculation usually involves a cut-off distance, beyond which the interactions are neglected. Evaluating the interatomic forces is computationally expensive and sets the practical limits for the scale of a simulation. Molecular force fields are further discussed in the next section.

Equations of motion. The classical equations of motion, a system of ordinary differential equations, are solved using finite difference methods. Broadly speaking, the integrator algorithm uses the current positions, velocities and accelerations of the atoms to estimate their positions and velocities after a short interval of time (the time step). Such integrators can be derived from Taylor series expansions of the positions, velocities and accelerations (and higher-order derivatives of the positions) about the current time.[8] (Allen and Tildesley, 1987) The suitability of a particular algorithm can be evaluated in terms of its short and long-term energy conservation (referred to as accuracy and stability, respectively), time-reversibility and symplecticity (Hairer et al., 2006). Moreover, the computational complexity of the algorithm should not be prohibitive from the viewpoint of practical simulations. Variants of the so-called Verlet scheme, which include the leap-frog (Hockney, 1970) and velocity-Verlet algorithms (Swope et al., 1982), are stable, time-reversible and symplectic, and offer a suitable balance between accuracy and computational cost. The velocity-Verlet algorithm was used in the simulations of **Publication I** and the leap-frog algorithm in those of **Publications II** and **III**. Besides the integrator algorithm, another key consideration

---

[7]The potential energy of an atomistic system can be written as a sum of terms that depend on the relative positions of pairs of atoms (pair potential), triplets of atoms (three-body potential), quadruplets of atoms (four-body potential), and so on. This is the so-called many-body expansion. (Kaplan, 2006) An effective pair potential captures some of the many-body effects due to the way it is parameterised.

[8]Systematic means for deriving integrators exist. See, for example, (Tuckerman et al., 1992).

is the choice of the time step. In simulations of biomolecular systems, the time step is, in practice, restricted to one femtosecond or less due to the presence of high-frequency bond vibrations, specifically those involving hydrogen. (Leach, 2001) This restriction can be alleviated by the use of constraint dynamics methods, which are briefly discussed in the next section. Another approach are the so-called multiple time step methods, in which long-range forces are evaluated less frequently than short-range forces. (Schlick, 2010)

Trajectory analysis. Various structural and thermodynamic properties can be determined by analysing the simulated trajectory. The properties of interest will largely depend on the kind of system studied. In simulations of molecular systems, relevant structural information includes, among others, (i) dimensional indicators, such as radii of gyration, (ii) conformational indicators, such as torsional angle distributions, (iii) order parameters, for example to quantify molecular orientations, and (iv) structural distribution functions, such as the radial distribution function. Valuable information can also be gained by examining the trajectory using molecular visualisation techniques. Various transport properties can be determined based on time-correlation functions. (Leach, 2001) For example, self-diffusion coefficients can be determined by integrating the velocity autocorrelation function. Some thermodynamic properties, such as temperature and pressure, can be measured directly. For example, the instantaneous temperature is defined as the average kinetic energy per degree of freedom, in accordance with the equipartition theorem. A time average of the instantaneous temperature then yields an estimate of the thermodynamic temperature. Other thermodynamic properties, such as free energies and entropies, require the use of specialised simulation techniques. (Frenkel and Smit, 2002) Trajectory analysis techniques used in **Publications I–III** are discussed further in Section 4.3: Simulation set-up and post-processing.

Thermodynamic ensembles. A direct simulation produces trajectories that sample the microcanonical (constant NVE) ensemble of statistical mechanics. However, the canonical (constant NVT) or the isothermal-isobaric (constant NPT) ensemble is often more appropriate for the system of interest. Simulations in the other ensembles can be achieved, among others, using stochastic and extended system methods. (Allen and Tildesley, 1987) Stochastic methods, such as that of Andersen (Andersen, 1980), represent an external heat bath by randomly re-assigning atom velocities from the Maxwell-Boltzmann distribution. This represents random collisions with the atoms of the heat bath. Extended system methods, such as the Nosé-Hoover method (Hoover, 1985), represent an external heat bath by an additional degree of freedom with its own kinetic and potential energy.

A third approach to temperature and pressure control involves the scaling of atom positions and momenta. (Leach, 2001) The kinetic temperature of the system can be adjusted to a desired value by scaling the velocities of the atoms by a suitable factor. Similarly, the instantaneous pressure of the system can be adjusted by scaling the posi-

tions of the atoms and the volume of the simulation domain. The Berendsen thermostat (Berendsen et al., 1984) scales the velocities at each time step so that the heating or cooling rate is proportional to the difference between the system temperature and the target temperature. The constant of proportionality, which is a free parameter, sets the characteristic time scale of the temperature relaxation. Correspondingly, the Berendsen barostat scales the atom positions at each time step so that the rate of pressure change is proportional to the difference between the system pressure and the target pressure. Again, the constant of proportionality sets the time scale of pressure relaxation. The Berendsen thermostat was used for temperature control in **Publication I**, and a Berendsen-like thermostat with an additional stochastic term (Bussi et al., 2007) was used in **Publications II** and **III**. The Berendsen barostat was used for pressure control in **Publications II** and **III**.

The open-source software LAMMPS (Plimpton, 1995) and GROMACS (Pronk et al., 2013) were used for the simulations in **Publication I** and **Publications II** and **III**, respectively.

4.2   Molecular force fields

Force field methods describe the potential energy of an atomistic system as a function of the nuclear positions. The force acting on an atom is then obtained as the negative gradient of the potential energy function at the site of the atom. A force field consists of the functional form of the energy expression and the associated set of parameters. Biomolecular force fields, and specifically those for carbohydrates, are almost invariably of the form described below. (Foley et al., 2012)

Firstly, the potential energy function can be expressed as a sum of bonded and non-bonded terms. The bonded terms describe intramolecular covalent bonding, and they act on pre-defined n-tuples of atoms. The non-bonded terms describe non-covalent intra and intermolecular interactions, and they act, with certain exceptions, on all atoms. The bonded and non-bonded terms of a biomolecular force field are summarised in Figure 6, and briefly discussed below. For a more detailed review of force field methods, see, for example, (Leach, 2001).

4.2.1   Bonded terms

The bonded terms include potential energy contributions due to bond stretching, bond angle bending and bond (torsional) rotations. The bond stretching term introduces a dependence of the potential energy on the distance between two covalently bonded atoms (Figure 6a). The bond stretching term is usually harmonic, which means that the force contribution is directly proportional to the deviation from a reference length. The harmonic approximation is justifiable at ambient conditions, where deviations from an equilibrium geometry can be considered minor. The Morse potential (Morse, 1929), or

(a) Bond stretching

$$V_{ij} = k_{\mathrm{r}}\left(r_{ij} - r_0\right)^2$$

(b) Bond angle bending

$$V_{ijk} = k_\theta\left(\theta_{ijk} - \theta_0\right)^2$$

(c) Bond rotation (torsion)

$$V_{ijkl} = \sum_{m=1}^{4} \frac{V_m}{2}\left(1 + \cos\left(m\phi_{jk} - \phi_m\right)\right)$$

(d) Van der Waals

$$V_{ij} = f_{ij}\left(\frac{A_{ij}}{r_{ij}^{12}} - \frac{C_{ij}}{r_{ij}^{6}}\right)$$

(e) Electrostatic

$$V_{ij} = f_{ij}\frac{q_i q_j e^2}{4\pi\epsilon_0 r_{ij}}$$
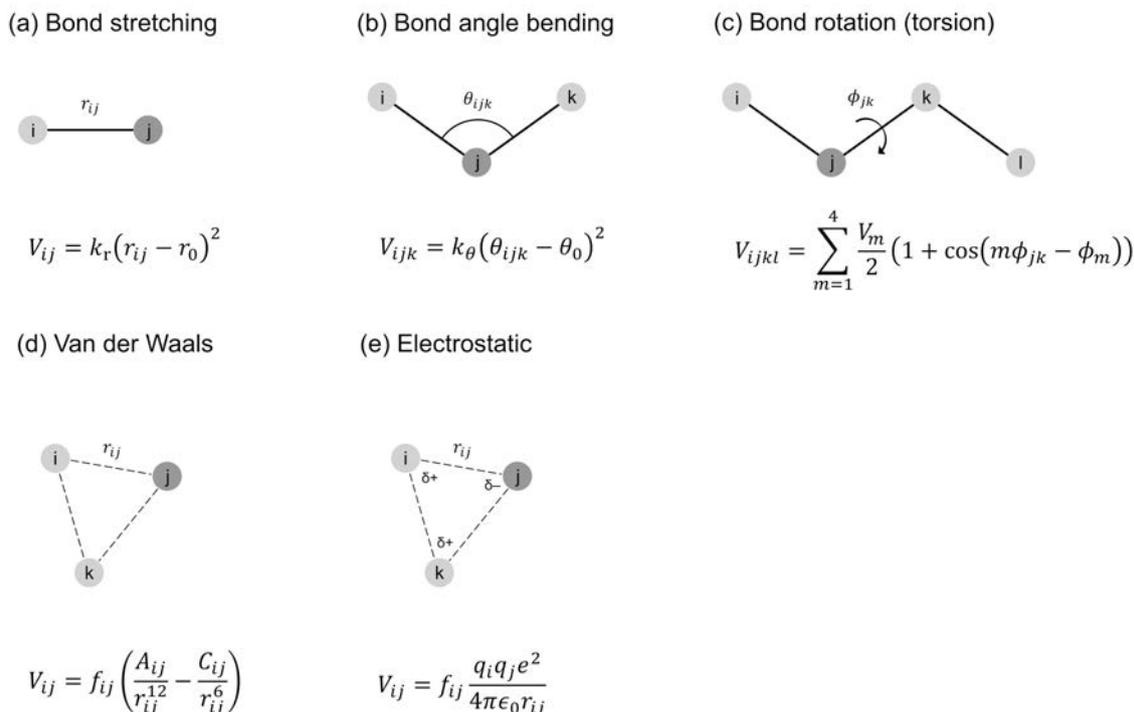
Figure 6. Bonded and non-bonded terms of a biomolecular force field. Potential energy contributions due to (a) bond stretching, (b) angle bending, (c) torsional rotation, (d) van der Waals interaction and (e) electrostatic interaction. The circles represent atoms, the solid lines represent covalent bonds, and the dashed lines represent non-covalent interactions. Some force fields also involve potential energy contributions due to improper torsions and cross-terms. Adopted from (Leach, 2001).

a series expansion thereof, can be used to improve the description of bond stretching energetics at larger deformations. This kind of refinement might be necessary, for example, to accurately reproduce vibrational spectra.

The angle bending term introduces a dependence of the potential energy on the angle formed by a sequence of three covalently bonded atoms (Figure 6b). Like the bond stretching term, the angle bending term is usually harmonic. The force contribution is then directly proportional to the deviation from a reference angle. As in the case of bond stretching, anharmonic terms can be used to improve the description of angle bending energetics.

The bond stretching and the angle bending term are of secondary importance from the viewpoint of conformational changes and other low frequency motions. (Schlick, 2010) It is thus commonplace to use so-called constraint dynamics methods to restrict the bond lengths, the bond angles or both to specific values (without affecting the non-constrained degrees of freedom). High frequency motions associated with bond length and angle vibrations are thus suppressed, and the equations of motion can be solved

using a longer time step. Commonly used methods for constraint dynamics include the LINCS (Hess et al., 1997), SHAKE (Ryckaert et al., 1977) and SETTLE (Miyamoto and Kollman, 1992) procedures.

The torsional term introduces a dependence of the potential energy on the rotation about the central bond in a sequence of four covalently bonded atoms (Figure 6c). It is used to introduce and adjust barriers to rotation about covalent bonds. Such barriers can arise, among others, due to steric repulsion and hyperconjugation effects. (Mo et al., 2004) The torsional term is usually a Fourier series with up to five terms. Moreover, so-called improper torsional terms can be used to enforce specific molecular geometries, such as the planarity of aromatic rings. An improper torsional term introduces a dependence of the potential energy on the rotation about the central bond in a sequence of four atoms that are not bonded in sequence (thus the term improper).

Lastly, so-called cross-terms are sometimes used to introduce couplings between the bonded terms. These are correction terms that compensate for the approximation of additive bond length, bond angle and torsional contributions. For example, a stretch-bend cross-term could be used to make the reference bond length (stretch) depend on the associated bond angle (bend). One can similarly define stretch-stretch, stretch-torsion, bend-bend and bend-torsion terms, as well as higher order terms (bend-bend-torsion, etc.). Force fields are sometimes classified according to the presence of cross-terms (Leach, 2001): force fields with harmonic bonded terms and no cross-terms belong to class I; force fields with anharmonic bonded terms and explicit cross-terms belong to class II; and force fields that apply corrections beyond torsional and cross-terms belong to class III.

4.2.2 Non-bonded terms

The non-bonded terms include potential energy contributions due to van der Waals and electrostatic forces. The van der Waals forces are considered to result from the interplay of attractive dispersion forces and repulsive exchange forces. The interactions are assumed to be pairwise additive, and they are usually described using the Lennard-Jones (LJ) 12-6 potential (Jones, 1924) (see Figure 6d). The r^{-6} term, which describes the dispersion forces at long distances, is motivated by quantum mechanical models, such as the Drude molecule (Leach, 2001). The r^{-12} term, which describes the exchange forces at short distances, lacks similar justification. The Buckingham potential (Buckingham, 1938) is sometimes used to improve on the description of the repulsive interaction.

The potential parameters are commonly optimised for interactions between atoms of the same species. Parameters for cross-species interactions are then obtained using so-called combination rules. The geometric combination rule[9] determines the cross-species

---

[9]Given in mathematical form in Equations 6 and 7.

interatomic zero-potential distance and potential well depth as a geometric average of the respective values for the involved species. The Lorentz-Berthelot combination rule uses an arithmetic average for the zero-potential distance and a geometric average for the potential well depth.

Since the van der Waals interactions are considered between all pairs of atoms, their computational cost grows dramatically with the system size. For this reason, the interactions are often neglected beyond a cut-off radius (with the potential shifted to zero at the cut-off distance). This approximation is justified by the r^{-6} decay of the LJ 12-6 potential. So-called dispersion correction terms for potential energy and pressure can then be added to adjust for the neglected interactions. While the correction is usually small with respect to potential energy, the corresponding effect on pressure can be significant for simulations in the isothermal-isobaric ensemble. For further details on the dispersion correction, see, for example, (Allen and Tildesley, 1987).

Electrostatic forces result from the uneven distribution of charge within molecules, and the presence of ions. The distribution of charge is usually represented using the partial atomic charge model.[10] In this model, fractional charges are assigned at the sites of the atomic nuclei. As part of the force field development, the charges are optimised to reproduce desired electrostatic properties, such as molecular multipole moments. Electrostatic interactions within and between molecules can then be calculated using the Coulomb potential (see Figure 6e). The partial charge model can be extended to involve interaction sites outside the nuclei, which enables it to describe non-spherical charge distribution around atoms. The partial charges are usually static, and thus represent the specific kind of environment for which they have been optimised. This limitation can be addressed by dynamic polarisation schemes, such as the charge equilibration method (QEq) (Rappe and Goddard, 1991) and the electronegativity equalisation method (EEM) (Mortier et al., 1986).

The electrostatic interactions are considered between all pairs of atoms. Consequently, they suffer from the same scaling issue as the van der Waals interactions. Moreover, due to their long-range character (the Coulomb potential decays as r^{-1}), the use of a potential cut-off can be problematic. (Steinbach and Brooks, 1994) Specialised techniques have been developed to address this issue. These include lattice sum methods, such as the Ewald summation (Ewald, 1921) and the Particle Mesh Ewald (PME) methods (Darden et al., 1993). Other long-range electrostatics techniques include the reaction field method (Allen and Tildesley, 1987) and the cell multipole method (Barnes and Hut, 1986).

A separate non-bonded term is sometimes introduced to describe hydrogen bonding. This can be, for example, an LJ 10-12 potential. However, a more common approach is to describe hydrogen bonding via the distribution of partial atomic charge and the

---

[10]Alternatives to the point charge approach exist, such as the bond dipole and the distributed multipole models. (Leach, 2001)

parameters of the van der Waals interactions.

The non-bonded interactions are typically excluded between atoms that share a co-
valent bond (1,2 interactions) or a bond angle (1,3 interactions), as these are described
by the bonded terms. Moreover, some force fields scale down the magnitude of the
non-bonded interactions for atoms separated by exactly three covalent bonds (1,4 in-
teractions). The non-bonded 1,4 interactions contribute to the rotational barrier about
the central bond, and the scaling is used to facilitate its parameterisation.

Two force fields were used in this thesis: the ReaxFF reactive force field in **Publica-
tion I**, and the optimised potential for liquid simulations (OPLS-AA) in **Publications
II** and **III**. These are described in further detail below.

4.2.3   Optimised potential for liquid simulations

The optimised potential for liquid simulations (OPLS) is a series of force fields de-
veloped by William L. Jorgensen and co-workers since the 1980s. The OPLS force
fields, of which there are all-atom and united-atom[11] variants, belong to the family of
class I force fields. The all-atom variant of the OPLS force field (OPLS-AA) is briefly
described below. For further details, see (Jorgensen et al., 1984).

In OPLS-AA, the potential energy of a molecular system is expressed as a sum of
bonded (covalent) and non-bonded (non-covalent) interactions. The bonded interac-
tions include terms for bond stretching, bond angle bending and torsional rotation.
Bond stretching and angle bending are both described by a harmonic potential:

$$V_{\text{bond}} = \sum_{\text{bond}} k_r \left(r - r_0 \right)^2 , \tag{1}$$

and

$$V_{\text{angle}} = \sum_{\text{angle}} k_\theta \left(\theta - \theta_0 \right)^2 , \tag{2}$$

where r is the bond length, r_0 is the equilibrium bond length, k_r is the harmonic force
constant of bond stretching, θ is the bond angle, θ_0 is the equilibrium bond angle, and
k_θ is the harmonic force constant of angle bending. The torsional potential is described
by a four-term Fourier series:

$$V_{\text{dihedral}} = \sum_{\text{dihedral}} \sum_{i=1}^{4} \frac{V_i}{2} \left(1 + \cos(i\phi - \phi_i) \right) , \tag{3}$$

where ϕ is the dihedral angle, and $\{V_i\}$ and $\{\phi_i\}$ are the amplitudes and locations of the

---

[11]United-atom force fields represent hydrogen atoms bonded to carbon atoms as a single interaction
site. By contrast, all-atom force fields represent all atoms explicitly.

constituent energy barriers. A dihedral angle of 0° corresponds to the *cis* conformation, while 180° corresponds to the *trans* conformation.

OPLS-AA describes non-bonded interactions using separate terms for electrostatic and van der Waals interactions. Electrostatic interactions are described by the Coulomb potential:

$$V_{\text{electrostatic}} = \sum_{i>j} f_{ij} \frac{q_i q_j e^2}{4\pi\epsilon_0 r_{ij}},$$
(4)

where r_{ij} is the distance between the interaction sites, q_i and q_j are their respective partial charges, ϵ_0 is the permittivity of free space, f_{ij} is the scaling factor for intramolecular interactions and e is the elementary charge. The scaling factor is used to adjust the interaction strength between atoms separated by one to three covalent bonds. Van der Waals interactions are described by the Lennard-Jones 12-6 potential:

$$V_{\text{van der Waals}} = \sum_{i>j} f_{ij} \left(\frac{A_{ij}}{r_{ij}^{12}} - \frac{C_{ij}}{r_{ij}^6} \right),$$
(5)

where A_{ij} and C_{ij} are potential parameters, r_{ij} is the distance between the interaction sites, and f_{ij} is the scaling factor for intramolecular interactions. The A_{ij} and C_{ij} parameters are related to the potential well depth, ε, and the interparticle distance at zero potential, σ, by $A_{ij} = 4\varepsilon_{ij}\sigma_{ij}^{12}$ and $C_{ij} = 4\varepsilon_{ij}\sigma_{ij}^6$. An OPLS-AA parameter set includes van der Waals parameters for interactions between atoms of the same species. Parameters for interactions between different species are obtained using the geometric combination rule:

$$A_{ij} = (A_{ii}A_{jj})^{1/2},$$
(6)

and

$$C_{ij} = (C_{ii}C_{jj})^{1/2}.$$
(7)

The non-bonded terms are evaluated for all intermolecular interactions, and for intramolecular interactions between atoms separated by three or more covalent bonds. For atoms separated by exactly three covalent bonds (1,4 interactions), the magnitude of the non-bonded interactions is scaled down by a factor of two.

OPLS-AA does not have a separate potential term for hydrogen bonding. Instead, hydrogen bonds are described using the van der Waals term and the distribution of partial charge. Atoms are classified into possible hydrogen bond donors and acceptors, and the bonds are identified based on a geometrical criterion. A hydrogen bond is considered to exist if the donor-acceptor distance is less than or equal to 3.5 Å, and

the hydrogen-donor-acceptor angle is less than or equal to 30°.

The OPLS-AA approach to parameter development emphasises the reproduction of thermodynamic and structural properties of pure organic liquids. (Jorgensen et al., 1996b) For example, the development procedure of the carbohydrate parameter set is as follows. (Damm et al., 1997) The parameter set involves atom types for saturated carbons, anomeric carbons, ether oxygens, hydroxyl oxygens, and hydrogens on carbon and oxygen, respectively. To address the non-bonded parameters, the hexopyranoses are divided into three charge neutral fragments: (i) the hydroxymethylene fragment, (ii) the C2–C4 polyol fragment, and (iii) the hemiacetal fragment. For fragments (i) and (ii), the non-bonded parameters are adopted from those of simple alcohols (Jorgensen et al., 1996b) and liquid 1,2-ethanediol (Jorgensen et al., 1996a), respectively. For the fragment (iii), the non-bonded parameters of the pyranose ring oxygen and the anomeric oxygen are adopted from those of ethers (Jorgensen et al., 1996b). The partial charge of the anomeric carbon is adjusted to obtain charge neutrality. The parameters of the bond stretching and angle bending terms are adopted from the AMBER all-atom force field (Cornell et al., 1995). Reference data for molecular geometries and conformational energetics are obtained from ab initio calculations on hexopyranoses, including the α and β anomers of D-glucopyranose, D-mannopyranose and D-galactopyranose. The torsional parameters are then optimised to reproduce the geometries and rotation barriers of a number of low-energy conformers.

The OPLS-AA force field was used in the MD simulations of **Publications II** and **III**. The force field parameters are a variant of the carbohydrate parameter set by Damm et al. (Damm et al., 1997), adapted for cellulose (Paavilainen et al., 2011). The adaptation includes using reoptimised bond torsion parameters (Jorgensen et al., 1996b; Price et al., 2001; Kony et al., 2002), and adjusting the partial charges to obtain neutral repeat units. The parameter set was chosen for backward compatibility with previous studies on cellulose microfibrils (Paavilainen et al., 2011, 2012; Orlowski et al., 2015). Further details are given in the Supporting Information of **Publication III**.

4.2.4   ReaxFF reactive force field

The ReaxFF reactive force field (Van Duin et al., 2001) is an empirical force field capable of describing chemical reactions. It achieves this by introducing a bond order dependence to the bonded and non-bonded terms. The bond order itself depends solely on interatomic distance. Thus, instead of pre-defined connectivity, the existence of covalent bonds is determined by the proximity and chemical identity of nearby atoms. ReaxFF also involves a dynamic polarisation scheme, in which the distribution of partial charge is determined by molecular geometry. An overview of the ReaxFF force field is given below. For further details, see (Chenoweth et al., 2008; Senftle et al., 2016).

The total energy expression of ReaxFF can be written as:

$$V_{\text{system}} = (V_{\text{bond}} + V_{\text{over}} + V_{\text{angle}} + V_{\text{torsion}}) + (V_{\text{vdW}} + V_{\text{Coulomb}}) + V_{\text{specific}}, \tag{8}$$

where V_{bond} is the bond energy; V_{angle} and V_{torsion} are the angle and torsional strain energy, respectively; V_{over} is the over-coordination penalty; V_{Coulomb} and V_{vdW} are the electrostatic and van der Waals energies, respectively; and V_{specific} encompasses several system specific terms, including lone-pair, conjugation, hydrogen bonding, and C_2 correction energies. The energy expression is summarised in Figure 7.

ReaxFF assumes that bond order depends only on bond length. The magnitude of the interaction is, in turn, determined by the bond order. The bond order between atoms i and j is expressed as a superposition of single (σ), double (π) and triple bond ($\pi\pi$) contributions:

$$BO_{ij} = BO_{ij}^{\sigma} + BO_{ij}^{\pi} + BO_{ij}^{\pi\pi}. \tag{9}$$

Each term has an exponential dependence on the interatomic distance, which enables a smooth transition between a non-bonded interaction and a full triple bond. For example, the bond order expression for a σ-bond is:

$$BO_{ij}^{\sigma} = \exp\left[p_{\text{bo},1}\left(\frac{r_{ij}}{r_0^{\sigma}}\right)^{p_{\text{bo},2}}\right], \tag{10}$$

where r_{ij} is the interatomic distance, r_0^{σ} is the equilibrium bond length, and $p_{\text{bo},1}$ and $p_{\text{bo},2}$ are empirical bonding parameters. The terms BO_{ij}^{π} and $BO_{ij}^{\pi\pi}$ have exactly the same form and corresponding parameters.

The functional form of BO_{ij} enables the description of long-range, partially bonded, transition states, which is necessary for an accurate description of reaction barriers. This feature requires the use of a correction factor, which reduces the bond order of partially bonded states in the case of over-coordination. The bonded contributions to the total energy (V_{bond}, V_{angle}, V_{torsion}) are calculated based on the corrected bond order. An additional energy penalty, V_{over}, is still needed to remove residual over-coordination after the bond order correction. The functional forms of the bonded terms are given in the Supporting Information of (Chenoweth et al., 2008). For brevity, they are not reproduced here.

ReaxFF considers non-bonded interactions between all pairs of atoms within a global cut-off range. Van der Waals interactions are described using the Morse-potential. A shielding term is added to avoid exaggerated repulsion between bonded atoms and atoms separated by two consecutive bonds. Electrostatic interactions are described using the Coulomb potential. Again, a shielding term is used to adjust for interactions at close distances. Partial charges are calculated at each iteration using the EEM
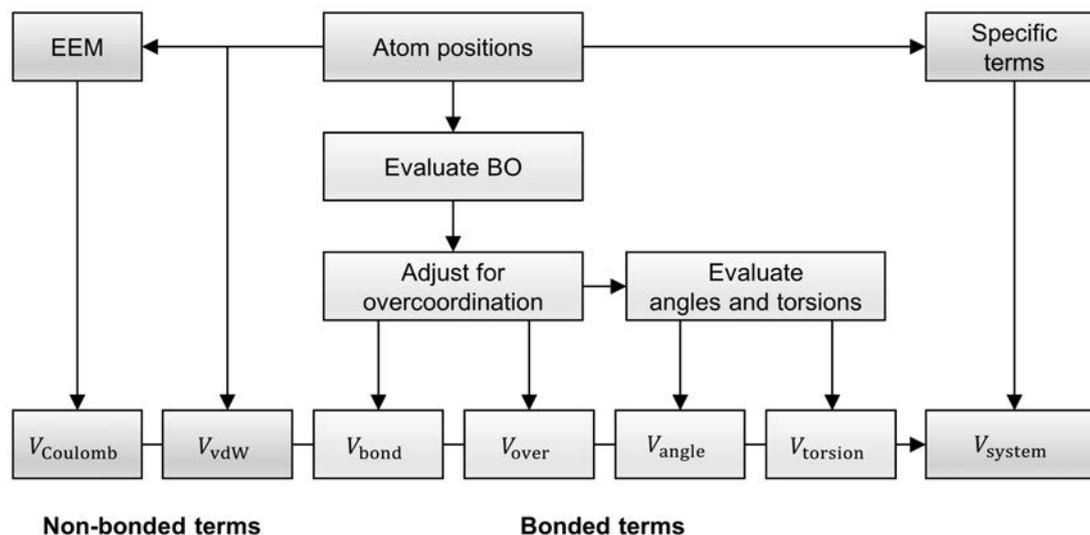
Figure 7. Summary of the ReaxFF energy calculation. Adapted from (Senftle et al., 2016) and used under CC BY 4.0 (https://creativecommons.org/licenses/by/4.0/).

(Mortier et al., 1986). Both non-bonded terms include a taper correction to avoid discontinuities at the cut-off radius. The functional forms of the non-bonded terms are given in the Supporting Information of (Chenoweth et al., 2008).

ReaxFF depends on a large set of parameters. For example, the hydrocarbon parameter set (Van Duin et al., 2001) involves 28 general and 71 element-specific parameters just for carbon and hydrogen. The parameters are optimised against what is called a training set—a collection of experimental and ab initio reference data on small molecules and a subset of their reactions. For example, the hydrocarbon training set includes reference data on: (i) molecular geometries, (ii) bond dissociation, angle bending and rotation barrier energetics; (iii) charge distributions; (iv) heats of formation; (v) relative stabilities; (vi) energetics of under and over-coordination; (vii) equations of state and (viii) cohesive energies of molecular crystals; and (ix) reaction mechanisms, such as hydrogen and methyl transfer. (Chenoweth et al., 2008)

The majority of the published parameter sets belong to one of two development branches: the combustion branch and the aqueous branch (Senftle et al., 2016). The combustion branch, which stems from the work of Chenoweth et al. (Chenoweth et al., 2008), is optimised for gas phase chemistry, while the aqueous branch is optimised for aqueous chemistry. Parameter sets within the same branch are intra-transferable. This means that an element described in one set can be transferred to another, and only the interspecies bond and angle parameters have to be added. The ReaxFF parameter set for hydrocarbon oxidation (Chenoweth et al., 2008), which belongs to the combustion branch, was used in the MD simulations of **Publication I**.

4.2.5   Force field validation

Atomistic simulation studies on cellulose have thus far relied on generic carbohydrate force fields. Their ability to describe the supramolecular structure and properties of cellulose is not self-evident. The question of transferability has been addressed in dedicated force field validation and comparison studies. These efforts have focused on the structural and mechanical properties of periodic cellulose crystals and microfibrils. Studies on periodic crystals have considered unit cell parameters, elastic constants and thermal expansion coefficients (Chen et al., 2014; Dri et al., 2015), while studies on microfibrils have considered lattice parameters, primary alcohol group conformations, hydrogen bonding patterns, and the shifting and tilting of chains. (Matthews et al., 2012; Oehme et al., 2018) Most of the considered force fields belong to the GROMOS, GLYCAM and CHARMM families.[12] The validation study by Dri et al. (Dri et al., 2015) is thus far the only one that concerns reactive force fields and cellulose.
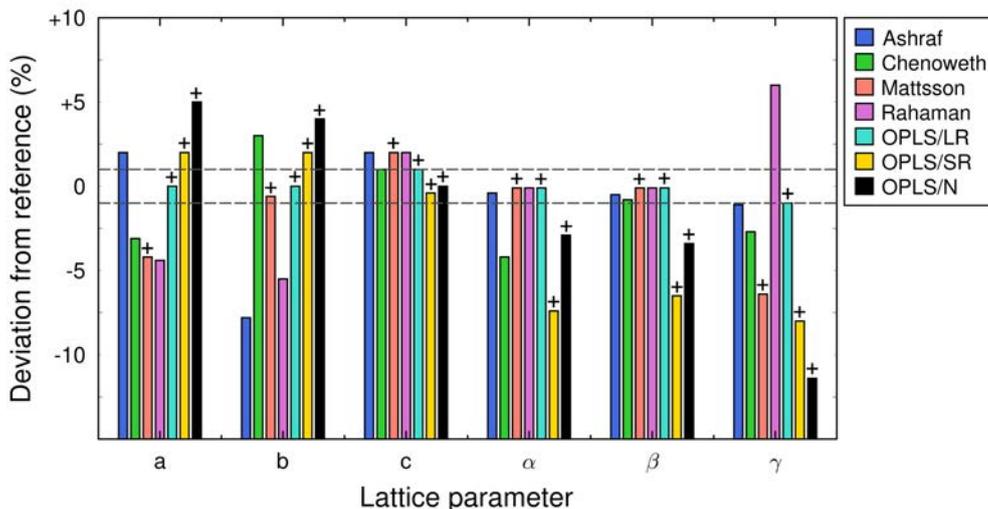
In this work, a series of simulations were carried out to determine how accurately the OPLS-AA carbohydrate force field and four variants of the ReaxFF force field reproduce the lattice parameters of crystalline cellulose I$_\beta$, and whether they retain the primary alcohol group conformations and the intralayer hydrogen bonding pattern. The considered ReaxFF parameter sets include those by Ashraf et al. (Ashraf and van Duin, 2017) (combustion branch), Chenoweth et al. (Chenoweth et al., 2008) (combustion branch), Mattsson et al. (Mattsson et al., 2010) (combustion branch) and Rahaman et al. (Rahaman et al., 2011) (aqueous branch).

The MD simulation set-up was the following. Crystallographic unit cell data for cellulose I$_\beta$ (hydrogen bonding pattern A) (Nishiyama et al., 2002, 2008) was used to construct an atomistic model of crystalline cellulose. The model consisted of a periodic system of $4 \times 4 \times 4$ (monoclinic) unit cells, which corresponds to dimensions of $3.11 \times 3.26 \times 4.15\,nm^3$. The system was brought to a local minimum of potential energy using the conjugate gradient algorithm. Besides the atomic coordinates, the size and the shape of the simulation domain were also considered. The six adjustable dimensions of the triclinic domain were included in the minimisation via additional energy terms due to external pressure and strain energy. A target pressure of 1 atm was applied to the six components of the stress tensor.

An MD simulation of 100 ns in the isothermal-isobaric (NPT) ensemble was used to equilibrate the system at 300 K temperature and 1 atm pressure. A Nosé-Hoover thermostat and barostat (Shinoda et al., 2004; Tobias et al., 1993) were used for temperature and pressure control. The associated damping constants were 10 fs and 100 fs, respectively. The velocity-Verlet algorithm was used to integrate the equations of motion with a constant time step of 0.1 fs. The system's linear and angular momentum

---

[12]Web resources: GROMOS: `http://www.gromos.net/`; CHARMM: `https://www.charmm.org/`; GLYCAM: `http://www.glycam.org/`.

Figure 8. Lattice parameters of cellulose I$_\beta$ as predicted by the OPLS-AA carbohydrate force field and four variants of the ReaxFF force field. The OPLS-AA simulations were carried out with (i) long-range electrostatics (LR), (ii) short-range electrostatics (SR) and (iii) no electrostatics (N). Plus sign (+) above a column indicates that the hydrogen-bonded layers are stable. The dashed lines indicate ±1 % deviation from the experimental reference.

were reset to zero at 1 ps intervals. The neighbour list was updated at an interval of ten time steps. Bond length or angle constraints were not applied. In the case of the OPLS-AA force field, the particle-particle-particle-mesh (PPPM) method (Hockney and Eastwood, 1988) was used to account for electrostatic interactions beyond the 1 nm cut-off range. Moreover, an additional simulation was carried out without the long-range electrostatics. The simulations were performed with the LAMMPS software.

Figure 8 shows a comparison of the lattice parameters, as predicted by the five force fields. The stability of the primary alcohol group conformations and the hydrogen-bonded layers are also indicated. The OPLS-AA force field reproduces the cellulose I$_\beta$ structure satisfactorily: the lattice parameters are within 1 % of the experimental values, and the hydrogen-bonded layers are stable. However, a visual inspection reveals that the chains are slightly tilted about their longitudinal axes. Specifically, the origin and the centre chains (see Chapter 3, Section 3.4: Crystalline forms) exhibit a right-handed and a left-handed tilt, respectively. The aberration is minor and does not disturb the hydrogen-bonded layers. Notably, the long-range electrostatics are necessary to reproduce the lattice parameters. The four ReaxFF variants do not perform as well. The best overall correspondence is obtained with the Mattsson parameter set, which is the only one that retains the intralayer hydrogen bonding pattern. This is presumably due to its wider hydrogen bonding range, as demonstrated in (Dri et al., 2015).

Reproducing the structure of a cellulose I$_\beta$ crystal does not amount to a thorough

validation for studies on wood cellulose. The experimental reference (Nishiyama et al., 2002) comes from tunicate[13] cellulose, the microfibrils of which are roughly 10–20 nm in diameter and highly crystalline. (Zhao and Li, 2014) In contrast, wood microfibrils are roughly 3 nm in diameter and contain a significant amount of disorder. As mentioned earlier, only 30–40 % of the cellulose in spruce microfibrils has a conformation compatible with the cellulose I$_\beta$ structure. (Fernandes et al., 2011). The microfibrils are believed to have a concentric structure, with disordered chains predominant at the surface. (Jarvis, 2018) As the detailed structure is not clear, the means for validation are limited.

4.3   Simulation set-up and post-processing

Simulation set-up and post-processing relied on tools provided in the LAMMPS (Plimpton, 1995) and GROMACS (Pronk et al., 2013) software distributions, as well as in-house tools specifically developed for the purpose.

In **Publication I**, the LAMMPS utility `mol_fra` was used to extract the chemical composition of product species from the ReaxFF bond information file. Further analysis involved in-house tools, as discussed below. In **Publication II**, the following GROMACS utilities were used for trajectory analysis: `hbond` was used to monitor hydrogen bonds between microfibrils; `distance` and `rotmat` were used to monitor the distance between microfibrils and their relative orientation, respectively; and `rdf` was used to determine the radial distribution function for carboxylate-sodium distance. No GROMACS utilities were used for trajectory analysis in **Publication III**. Further details of the utilities can be found in the GROMACS User Manual (Abraham et al., 2019).

In addition to the functionality provided by the LAMMPS and GROMACS software distributions, some specialised techniques and in-house software tools were needed. The most important tools and techniques are discussed below, in the order in which they appear in **Publications I–III**. Straightforward procedures, such as creating and modifying molecular geometries and topologies, determining molecular conformations and identifying hydrogen bonds, are not discussed. The Ovito Open Visualisation Tool (Stukowski, 2010) and the OpenBabel Toolkit (O'Boyle et al., 2011) provided the framework for the software tools. Molecular visualisations were created using the Ovito Open Visualisation Tool and the PyMOL Molecular Graphics System (Schrödinger LLC, 2015).

---

[13]Tunicates are marine invertebrates, the exoskeleton of which contains cellulose. The species in question is *Halocynthia roretzi*, or the sea pineapple.

4.3.1   Classification of decomposition events

In **Publication I**, chemical bonding information produced by the ReaxFF-MD simulations had to be parsed to determine details of the chemical composition and structure of the product species. Software tools were developed for this purpose using the Open-Babel C++ API.

Chemical bonding information was used to deduce the number of molecules; their chemical composition; the state of the glycosidic bonds; and the number of cyclic structures of different size. The first three are readily extracted from the atom connectivity table. The fourth involves ring perception, for which the smallest set of smallest rings (SSSR) algorithm (Figueras, 1996) of the OpenBabel Toolkit was used. The SSSR algorithm determines the minimal cycle basis of a chemical graph, and thus the number of closed rings of atoms. It is not infallible in complex situations that involve fused ring structures, but such structures were not expected to form.

Specific algorithms were developed to identify known products of cellulose pyrolysis among the product species. These include, among others, levoglucosan (LGA), glycolaldehyde, formic acid, the hydroxymethyl radical and formaldehyde. The presence of LGA-like end groups was also considered. Some of the low molecular weight products, including water and carbon dioxide, could be identified solely based on their chemical composition.

Using the obtained information, it was possible to classify each decomposition event as (i) the cleavage of a glycosidic bond, (ii) some other type of chain scission, or (iii) the release of a low molecular weight product. For glycosidic bond cleavage, the location along the cellulose chain and the bonding preference of the glycosidic oxygen (towards the reducing or the non-reducing end) could be determined. Moreover, the low molecular weight products could be identified, and the involvement of ring opening or contraction reactions could be determined.

4.3.2   Umbrella sampling

In **Publication II**, the umbrella sampling method (Torrie and Valleau, 1977) and the weighted histogram analysis method (WHAM) (Kumar et al., 1992) were used to evaluate the potential of mean force (PMF) of separating (or bringing together) two aligned microfibrils. The umbrella sampling simulations and the related analyses were carried out using tools included in the GROMACS software distribution.

Umbrella sampling is a technique for determining the free energy profile (i.e. PMF) along a reaction coordinate[14]. The free energy profile can be calculated from the probability density function[15] (PDF) along the reaction coordinate. The PDF, in turn, can be approximated by the distribution of states that are sampled during a

---

[14]An abstract coordinate that quantifies the progress of a transition between two states.

[15]Gives the probability that the system is found near a given value of the reaction coordinate.
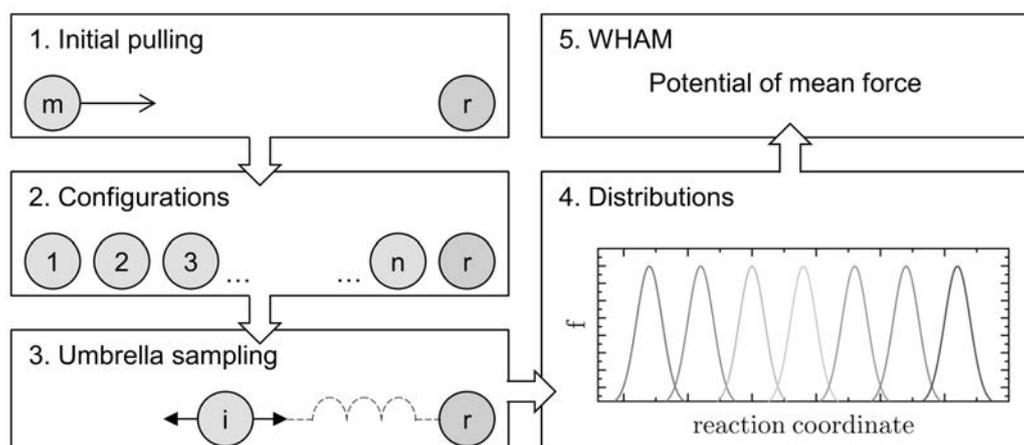
Figure 9. Workflow for determining the potential of mean force using the umbrella sampling method and the weighted histogram analysis method. The reference fibril (r) is fixed and the mobile fibril (m) is constrained at various locations (1...n) along the reaction coordinate. Reprinted from (Paajanen et al., 2016) with kind permission from Springer. Copyright Springer Science+Business Media Dordrecht 2016.

simulation. However, direct sampling is impractical when the transition of interest involves regions that are sampled rarely. This is usually the case. Umbrella sampling solves the problem as follows (see Figure 9). The chosen reaction coordinate is divided into segments, referred to as sampling windows. A bias potential is then used to restrain the reaction coordinate to a target value within each of these windows. The bias potential is typically a harmonic potential with only a single parameter—the bias strength. An independent simulation is then carried out for each sampling window. The addition of the bias potential results in a biased PDF and, consequently, a biased free energy.

The unbiased PDF can be expressed as a product of the biased PDF and terms that only depend on the bias potential (and temperature). It follows that the unbiased free energy can be expressed as a sum of three terms: one that depends on the biased PDF and two that depend on the bias potential. One of the latter terms turns out to be a constant. Since the bias potential is known and an approximation of the biased PDF can be obtained from the simulations, the free energy profile can be determined up to an additive constant.

If several sampling windows are involved, the free energy profile has to be pieced together from contributions that each have a different offset. The WHAM has been developed for this purpose. It reconstructs the PDF along the reaction coordinate as a weighted average of the PDFs of the individual windows. The weights are chosen in an iterative process that minimises the statistical error. The GROMACS software distribution includes the `g_wham` tool (Hub et al., 2010) for this purpose. Mathematical

details of the umbrella sampling method and the WHAM can be found in (Kästner, 2011) and (Kumar et al., 1992), respectively.

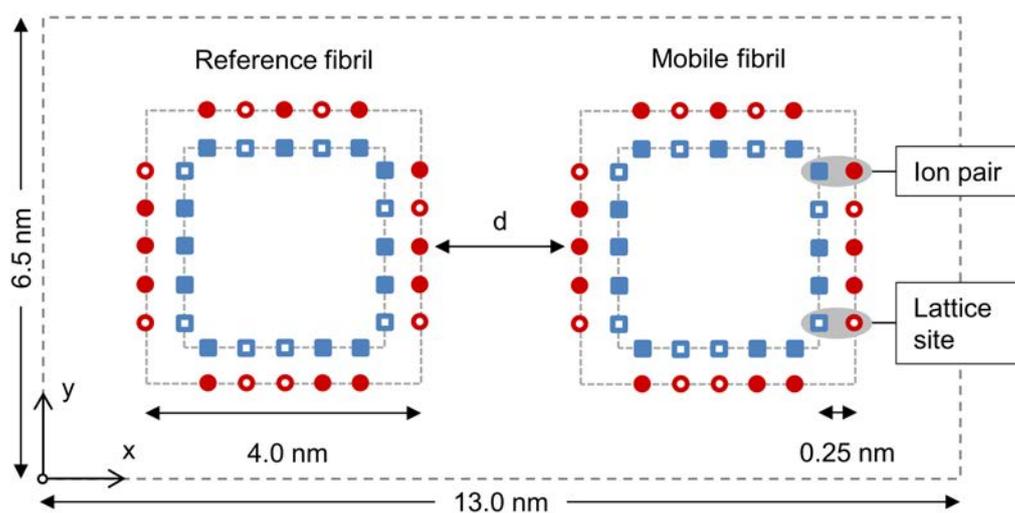### 4.3.3   Electrostatic model for microfibril interaction

In **Publication II**, an electrostatic model was developed to complement the umbrella sampling simulations on microfibril interactions. The purpose was to elaborate on the role of charged surface groups in the interaction between two carboxylated microfibrils, and the variation in interaction strength due to different patterns of substitution. The model was implemented using the Matlab software (MathWorks Inc., 2010).

Carboxylate groups on the microfibril surface were represented by point-like particles with a negative elementary charge. Similarly, sodium counter-ions were represented by point-like particles with a positive elementary charge. Pairs of carboxylate groups and sodium ions were distributed at random locations in a lattice that represented a microfibril surface (see Figure 10). Two copies of the fibril were then embedded in a simulation domain, so that the set-up mirrored that of the umbrella sampling simulations. Both periodic and free boundary conditions were considered. The distance between the fibrils was varied by making one of them stationary (reference) while moving the other (mobile). The electrostatic potential of the reference fibril was evaluated as a function of inter-fibril distance for different functionalisation levels. One hundred random charge configurations were considered in each case (with uniform probability distribution with respect to the lattice sites). In contrast to the umbrella sampling simulations, the medium was assumed to have the permittivity of free space.

4.3.4   Twist rates of microfibrils and their bundles

In **Publication III**, the twist rates of microfibrils and their bundles had to be determined from the time evolution of atomic coordinates. Scripts were developed for this purpose using the Ovito Python interface.

The twist rate of a microfibril about its longitudinal axis was determined based on the twist rates of its constituent chains. These were determined as follows (see Figure 11). Firstly, the longitudinal axis of the chain was defined as the line that passes through the centres of mass of the third and fourth glucose unit from the reducing end (point A) and the non-reducing end (point D). Secondly, the longitudinal axis of the fibril (through points B and C) was defined in a similar manner, considering glucose units from all of the constituent chains. The terminal glucose units (i.e. the first and second from both ends) were omitted, since increased conformational disorder could be expected at the solute-solvent interface. Lastly, the twist rate was defined as the dihedral angle (χ) between the planes that contain the points (A,B,C) and (B,C,D), divided by the length of the line segment BC. The twist rate of a fibril bundle about its longitudinal axis was defined in an analogous manner to that of the fibril about its

Figure 10. Electrostatic model for microfibril interactions. The two squares represent two parallel fibrils, viewed along their longitudinal axes. The solid red dots and blue squares represent positively (sodium) and negatively charged (carboxylate) ions, respectively. The red dots and blue squares with a white interior represent vacant lattice sites. The outermost dashed line indicates the periodic boundaries. Reprinted from (Paajanen et al., 2016) with kind permission from Springer. Copyright Springer Science+Business Media Dordrecht 2016.

axis, with fibrils taking the role of individual chains.

4.3.5   Specific surface area of microfibrils and their bundles

In **Publication III**, the specific surface areas of microfibrils and their bundles had to be determined from the time evolution of atomic coordinates. The purpose was to obtain values that could be compared against the results of nitrogen sorption experiments. Scripts for this purpose are included in the Ovito software.

The specific surface area of a microfibril or a microfibril bundle was determined as follows. A polyhedral mesh was constructed around the involved set of particles using the alpha-shape method (Edelsbrunner and Mücke, 1994). The exterior surface area of the mesh could then be evaluated. The specific surface area was obtained by dividing the exterior surface area of the mesh by the mass of the enclosed fibril(s). The surface area determined using the alpha-shape method is somewhat sensitive to the diameter of the used probe sphere. Probe diameters between 6 and 36 Å were used to account for this sensitivity.

4.3.6   Diffusion of water molecules

In **Publication III**, the diffusion rates of water molecules had to be determined from the time evolution of atomic coordinates. The purpose was to study the behaviour of
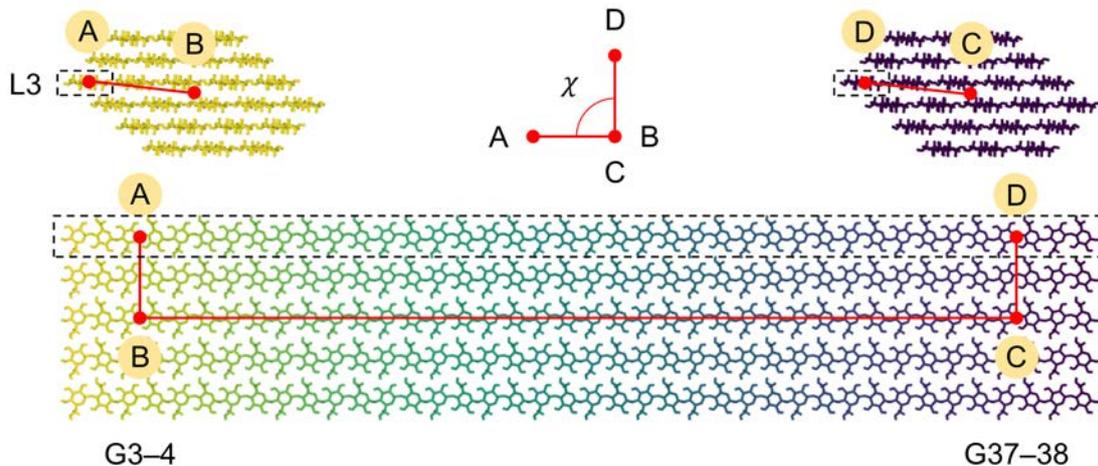
Figure 11. The twist rate of a cellulose chain about the longitudinal axis of a microfibril was defined as the dihedral angle (χ) between the planes that contain the points (A, B, C) and (B, C, D), divided by the length of the line segment BC. The figure includes references to the layers (L) of hydrogen-bonded cellulose chains (numbered from 1 to 6) and glucose units (G) (numbered from 1 to 40).

water near microfibril surfaces and within cavities found in their bundles. Scripts were developed for this purpose using the Ovito Python interface.

The diffusion of water molecules was followed by recording the mean squared displacements (MSD) of their oxygen atoms as a function of simulated time. The time-evolution of the MSD is related to the diffusion rate via the Einstein relation (for Brownian motion). (Allen and Tildesley, 1987) Thus, a linear least-squares fit could be used to determine the self-diffusion coefficients. The mobility of the water molecules was also quantified by measuring the time for which they could be found within a given distance from the microfibril surfaces.

4.4   Computational fluid dynamics

Computational fluid dynamics (CFD) refers to a family of computer simulation techniques for solving the hydrodynamic equations, the governing equations of fluid flow. These include the conservation equations for mass, momentum and energy. (Choudhuri, 1998) The mass conservation equation reads, in differential form:

$$\frac{\partial \rho}{\partial t} + \nabla \cdot (\rho \boldsymbol{v}) = 0, \tag{11}$$

where ρ is the density of the fluid and $\boldsymbol{v}$ is its velocity. That is, the rate of mass accumulation within a stationary control volume equals the difference of the mass flux into the volume and the mass flux out of the volume. The momentum conservation

equation, also known as the Navier-Stokes equation, reads:

$$\frac{\partial \boldsymbol{v}}{\partial t} + (\boldsymbol{v} \cdot \nabla)\, \boldsymbol{v} = -\frac{1}{\rho}\nabla p + \boldsymbol{F} + \frac{\mu}{\rho}\nabla^2 \boldsymbol{v}, \tag{12}$$

where μ is the dynamic viscosity of the fluid, p is the pressure and $\boldsymbol{F}$ represents external body forces. The Navier-Stokes equation states that the fluid flow is driven by pressure gradients, viscous stresses and external forces. Lastly, the energy conservation equation reads:

$$\rho\left(\frac{\partial \epsilon}{\partial t} + \boldsymbol{v} \cdot \nabla \epsilon\right) - \nabla \cdot (k\nabla T) + p\nabla \cdot \boldsymbol{v} = 0, \tag{13}$$

where ϵ is the internal energy per unit mass, T is the temperature and k is the thermal conductivity. The energy conservation equation describes the transport of internal energy via thermal conduction and its generation via viscous damping (although the latter is omitted in the given form of the equation).

Solution methods. Solving the hydrodynamic equations usually involves simplifying assumptions, such as that of incompressible flow. The solution strategy depends on the applied simplifications and involves considerations such as the choice of discretisation scheme, numerical grid, finite approximations and solution method. These are briefly discussed below, following (Ferziger and Perić, 1996) and (McGrattan and Miles, 2016).

After the simplifications have been applied, the equations are discretised, that is, approximated by a system of algebraic equations. Commonly used discretisation methods include the finite difference method, the finite volume method and the finite element method. The finite volume method, which was used in this work, is founded on the integral form of the hydrodynamic equations. The simulation domain is divided into small control volumes using a numerical grid that defines their boundaries. Both structured and unstructured grids can be applied. The solution variables are associated with one or more computational nodes that are located within each control volume.

The hydrodynamic equations are applied to each control volume, and the nearby nodal values are used to approximate the associated surface and volume integrals. This is achieved by using interpolation and numerical integration schemes. The discretisation yields a system of algebraic equations, which can be solved using various methods. The choice of the solution method depends on the problem at hand, the type of the numerical grid and the number of nearest neighbour nodes that contribute to the solution for each control volume. For further details, see, for example, (Ferziger and Perić, 1996).

Turbulence models. Turbulent flow conditions can be problematic for the direct numerical solution of the hydrodynamic equations. This is because the temporal and spatial resolution needed to capture dissipative processes makes the solution computa-

tionally expensive. To address this issue, methods have been developed for predicting turbulent flows without the need to resolve the entire spectrum of turbulent motions. Commonly used methods include Reynolds-averaged Navier-Stokes (RANS) and large eddy simulation (LES). (McGrattan and Miles, 2016) The RANS method, which was used in this work, is founded on time (or ensemble) averaging of the hydrodynamic equations. The RANS equations thus represent the evolution of the mean flow field. The temporal and spatial resolution can accordingly be lower. The Reynolds-averaging introduces an additional term to the momentum conservation equation: the Reynolds stresses. This term represents the effects of the unresolved turbulent motions. The Reynolds stresses can be approximated using a turbulence model. The standard k-ε model (Launder and Spalding, 1974), which was used in this work, relates the Reynolds stresses to mean velocity gradients via two additional field variables: the turbulent kinetic energy and the rate of its dissipation. Additional transport equations are solved for these variables.

Multiphase flows. Simulating multi-phase flows can be approached using several methods. (Prosperetti and Tryggvason, 2007) The volume-of-fluid (VOF) method (Hirt and Nichols, 1981), an Euler-Euler approach, was used in this work to simulate the stratified flow of two immiscible fluids. The VOF method uses an additional field variable, the volume fraction, to account for the presence of multiple component phases. From the viewpoint of the hydrodynamic equations, the component phases constitute a single fluid. The fluid properties, such as density and viscosity, are obtained as the volume fraction weighted average of the component properties. The solution variables, such as the velocity field, are shared by the component phases. An additional transport equation is used to solve for the evolution of the volume fraction field. Maintaining a sharp volume fraction profile across the phase boundaries is important, and requires the use of specialised discretisation schemes, such as the multi-dimensional limiter for explicit solution (MULES) method. (Damián, 2013) Surface tension effects can be addressed, for example, using the continuum surface force (CSF) model. (Brackbill et al., 1992) This model introduces an additional force term to the momentum conservation equation, which relates the surface tension to the local curvature of the phase boundary. Wall adhesion effects can be addressed using a dynamic boundary condition for the contact angle, which adjusts the curvature near rigid boundaries.

Rheological models. Fluids can be classified according to their response to shear deformation. (Bird et al., 2006) If the shear stress is directly proportional to the shear rate, as in Newton's law of viscosity, the fluid is referred to as Newtonian. Fluids that deviate from this behaviour are referred to as non-Newtonian. Shear thinning, the decrease of viscosity with increasing shear rate, is a typical non-Newtonian behaviour. It is encountered, among others, in polymeric liquids. Time-independent shear thinning behaviour can be described, for example, using the power-law fluid model, in which

the viscosity depends on the shear rate according to the power-law:

$$\mu = K\dot{\gamma}^{n-1}, \tag{14}$$

where $\dot{\gamma}$ is the shear rate, K is the flow consistency index and n is the flow behaviour index. The power-law fluid model was used in **Publication IV** to describe the shear thinning behaviour of CNF-based hydrogel formulations.

Time-dependent shear thinning behaviour, or thixotropy, is encountered in micro-structured fluids, such as hydrogels. It can be understood in terms of the breakdown and build-up of the fluid's internal structure (Barnes, 1997), and described, for example, using a kinetic thixotropy model. (Mewis and Wagner, 2009) Such models use a scalar structure parameter to describe the local state of the fluid. The parameter evolves in time according to a kinetic equation that includes terms for the formation and breaking of intermolecular bonds, as induced by thermal and convective motion. The instantaneous viscosity is linked to the structure parameter via a functional dependence.

In **Publication IV**, the open-source software OpenFOAM[16] was used to solve the hydrodynamic equations for two incompressible and isothermal immiscible fluids. The forward-Euler discretisation scheme was used for the time derivative, and the standard finite volume discretisation of Gaussian integration for the gradient, divergence and Laplace operators, along with linear, linear upwind and van Leer interpolation schemes. A block-structured numerical grid was used to describe the flow domains. A symmetric Gauss-Seidel solver was used for the volume fraction variable and velocity, whereas a preconditioned (bi)conjugate gradient solver with a diagonal incomplete-Cholesky preconditioner was used for pressure. The PIMPLE algorithm, a hybrid of the pressure-implicit split-operator (PISO) and semi-implicit method for pressure-linked equations (SIMPLE) algorithms was used for pressure-velocity coupling. (Ferziger and Perić, 1996) The power-law fluid model was used to describe time-independent shear-thinning behaviour. The RANS method and the standard k-ε model were used to account for turbulent flow conditions.


[16]Web resources: OpenFOAM: `https://openfoam.org/`.

5   Results and discussion

This chapter reviews the main findings of **Publications I–IV**. Future directions for the research are discussed at the end of each section.

5.1   Pyrolytic degradation of cellulose (I)

The pyrolytic degradation of cellulose involves hundreds of chemical reactions and volatile products. (Mettler et al., 2012a) One of the fundamental challenges of cellulose pyrolysis research is to describe these elementary reactions, which, despite long-standing experimental efforts, remain debated. (Burnham et al., 2015; Lédé, 2012; Lin et al., 2009; Mettler et al., 2012a; White et al., 2011) The methods of computational chemistry are increasingly used to complement the experimental efforts. (Agarwal et al., 2012; Hosoya and Sakaki, 2013; Liu et al., 2011; Mayes and Broadbelt, 2012; Murillo et al., 2015; Zhang et al., 2015a, 2011, 2015b, 2014) Most of the computational studies are based on electronic structure calculations, which can provide detailed information on pre-determined reaction paths. Methods based on reactive force fields, which are less accurate, but can be used to predict reaction paths, have been used in only a few studies (Paajanen and Vaari, 2017; Zheng et al., 2016). In **Publication I**, we used ReaxFF-MD simulations to predict molecular-level mechanisms of cellulose pyrolysis. Our aim was to identify primary decomposition reactions, and to give predictions of the associated kinetics. Detailed knowledge of the reaction paths would form a basis for detailed control over the pyrolysis process. Such capability would be valuable in the design, development and optimisation of flame-retardant chemistries and thermo-chemical conversion processes.

We carried out a series of ReaxFF-MD simulations of the thermal decomposition of a cellulose molecule in gas-phase conditions. The force field parameter set was that by Chenoweth et al. (Chenoweth et al., 2008). We used a stochastic approach that considered cellulose chains of different molecular weights and conformations at a range of temperatures. This involved repeated simulations for each combination of molecular weight, conformation and temperature. In each simulation, we recorded the time of the first decomposition event and the chemical composition of the products. We then determined the average rate constant of the dominant reaction based on the distribution of decomposition times. With simulations at different temperatures, we could determine the temperature dependence of the reaction rate constant, and, by fitting against the Arrhenius equation, the corresponding kinetic parameters. Figure 12 shows a visual summary of the stochastic simulation procedure. We considered cellulose chains from 8 to 64 glucose units long in elongated, slightly coiled and globular conformations. The simulation temperatures ranged from 1400 K to 2200 K. The temperatures are significantly higher than those in conventional pyrolysis experiments. Such temperatures were used for accelerated dynamics, that is, to sample a sufficient
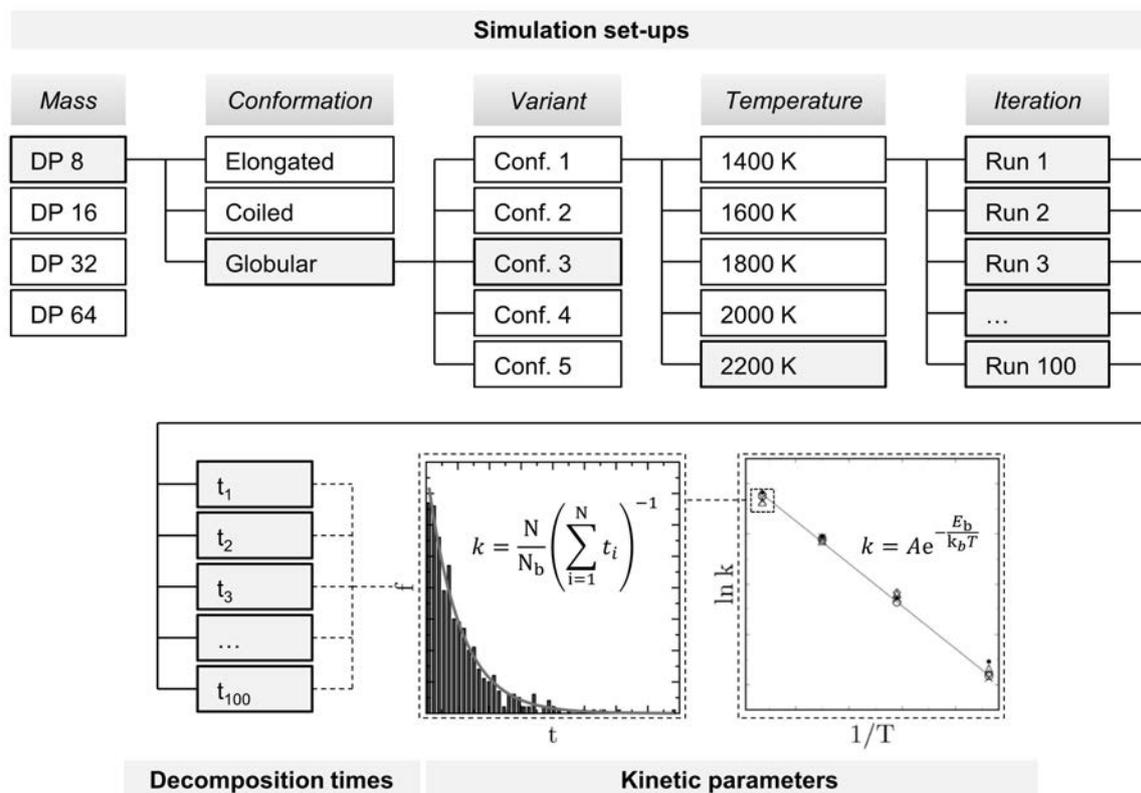
Figure 12. Visual summary of the stochastic simulation procedure. One hundred simulations were carried out for each combination of molecular weight, initial conformation (type and realisation) and temperature. The temperature dependence of the reaction rate constant was determined from the distribution of decomposition times and fitted against the Arrhenius equation. The steps leading to a single data point in the Arrhenius plot are highlighted.

number of decomposition events in a reasonable time.

Most of the observed decomposition events were depolymerisation reactions (that is, glycosidic bond cleavage; see Figure 13a). Indeed, experimental evidence suggests that the pyrolytic degradation of cellulose begins with depolymerisation, which, in the end, leads to the level of oligo and monosaccharides. (Lin et al., 2009; Mamleev et al., 2006; Pouwels et al., 1989; Várhegyi et al., 1994) We found the scission probability to be uniformly distributed across the glycosidic bonds, which implies that gas-phase conditions would not favour selective depolymerisation, such as unzipping (see Figure 13b). In two thirds of the reactions, the glycosidic oxygen remained bonded towards the anomeric carbon. Moreover, in half of the simulations, a ring opening reaction preceded or coincided with the depolymerisation event. Ring contraction reactions were also observed, but only in a minority of events.

Figure 13c shows the temperature dependence of the reaction rate constant for the depolymerisation reactions. The regular, logarithmic, behaviour implies that the
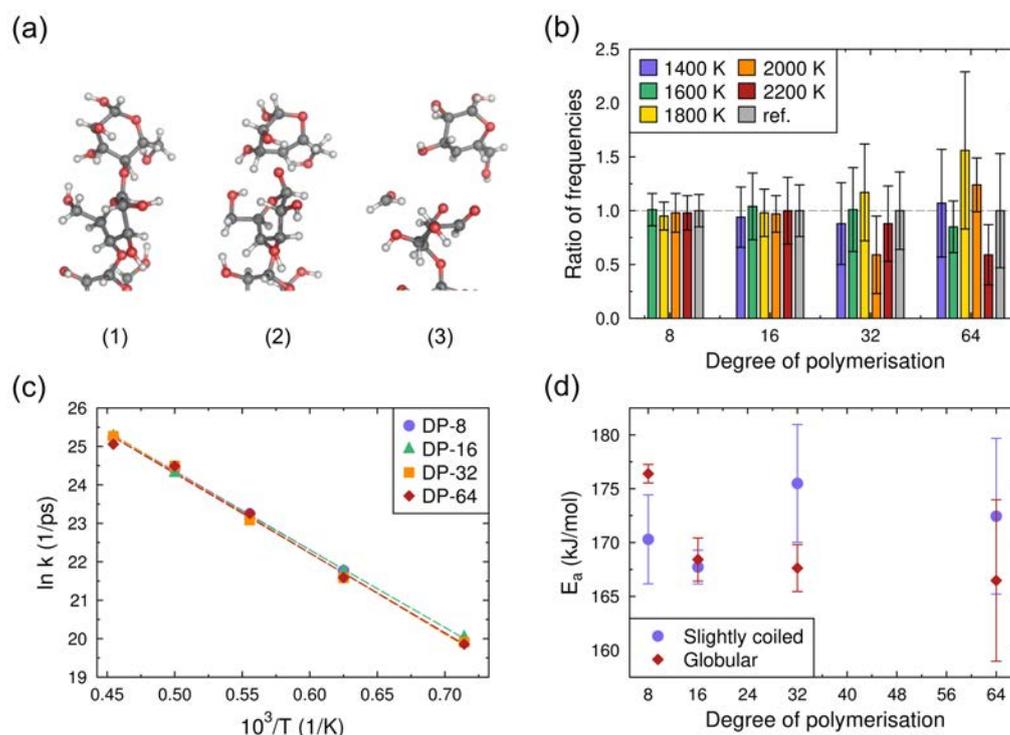
Figure 13. (a) Example of an end-chain depolymerisation reaction accompanied with the release of a hydroxymethyl radical (in three consecutive steps). (b) Uniform scission probability across the glycosidic bonds, as demonstrated by the ratio of the observed end-chain depolymerisation frequency and the corresponding expectation value when the chain scission probability is uniformly distributed. (c) Arrhenius plots for the slightly coiled chains. (d) Activation energies for the different conformations and degrees of polymerisation.

underlying reaction mechanism stays the same. The kinetic parameters have no observable dependence on the molecular weight or the initial conformation, as shown in Figure 13d. The average activation energy and frequency factor are $(171 \pm 2)\,\mathrm{kJ\,mol^{-1}}$ and $(1.07 \pm 0.12) \times 10^{15}\,\mathrm{s^{-1}}$, respectively.

Both the activation energy and the frequency factor fall within the range of values obtained from cellulose pyrolysis experiments. As the experimental values are based on global mass loss measurements, they correspond to an average over the underlying elementary reactions. (Lin et al., 2009) Comparison against the simulations is, however, sensible, as depolymerisation is believed to be a rate-limiting step. (Bradbury et al., 1979; Lédé, 2012; Mamleev et al., 2006; Várhegyi et al., 1994) The wide range of experimental values, 48–282 $\mathrm{kJ\,mol^{-1}}$ for the activation energy, does not provide a particularly useful baseline. However, a subset of the studies, with physically plausible frequency factors, report activation energies in the range 190–200 $\mathrm{kJ\,mol^{-1}}$. Compared to this subset, it would seem that ReaxFF-MD slightly underestimates the activation energy for the depolymerisation of cellulose.

Our results can also be compared against those of ab initio studies. For example, Agarwal et al. (Agarwal et al., 2012) observed several reactions leading to depolymerisation in their ab initio MD (AIMD) simulations of cellulose pyrolysis (at 600 and 873 K). They report free energy barriers in the range 130–527 kJ mol^{-1}, half of which belong to the narrower range 151–180 kJ mol^{-1}. Roughly half of the observed reactions involve ring opening, contraction or fragmentation. Our observations are compatible with the majority of the proposed mechanisms. Moreover, Hosoya and Sakaki (Hosoya and Sakaki, 2013) studied depolymerisation via a concerted mechanism using density functional theory (DFT) calculations. The concerted mechanism involves concurrent cleavage of the glycosidic bond and the formation of LGA. They report activation energies in the range 160–198 kJ mol^{-1} for gas-phase reactions, and slightly higher values in the solid-phase. Mayes and Broadbelt (Mayes and Broadbelt, 2012) studied the same mechanism, for which they determined an activation energy of 231 kJ mol^{-1}. Our simulations did not involve the formation of LGA.

Finally, we observed the release of low molecular weight products in a minority of the decomposition events. The most common species were glycolaldehyde, water, formaldehyde and formic acid, all of which belong to the known products of cellulose pyrolysis (Mettler et al., 2012a,b; Vinu and Broadbelt, 2012). We could also compare against the ReaxFF-MD simulations of Zheng et al. (Zheng et al., 2016). Our observations on LMWPs are compatible, taking into account that their simulations also involved secondary reactions.

Our work in **Publication I** demonstrates that ReaxFF-MD can be used to predict specific details of the pyrolysis chemistry of cellulose and the kinetics of the associated reactions. We chose to first look at primary reactions in the gas-phase, and, based on the lessons learned, build towards condensed-phase pyrolysis simulations involving secondary and tertiary reactions. Our intention is to continue with simulations that use microfibril models similar to those developed in **Publication III**. One of the key questions is whether ReaxFF-MD predicts the formation of LGA when the condensed-phase electrostatic environment is accounted for. Ultimately, we hope to reproduce the primary reaction paths and their associated kinetics, and probe ways of altering the degradation process.

5.2   Disintegration of chemically modified cellulose (II)

Chemical pretreatment of cellulose by TEMPO-catalysed oxidation significantly reduces the energy demand of CNF production. (Saito et al., 2006) The effect stems from the introduction of charged carboxylate groups on the fibre surfaces, and affects not only the disintegration, but also the aggregation behaviour of the constituent microfibrils. Consequently, the surface charge also affects the rheology of aqueous CNF suspensions. The effect of TEMPO-oxidation on the microfibril interactions has been

studied by theoretical means, notably the Derjaguin-Landau-Verwey-Overbeek (DLVO) theory (Fall et al., 2011; Fukuzumi et al., 2014). The continuum approach of the DLVO theory enables the prediction of average interaction potentials, but does not address the role of spatial and temporal heterogeneity. In **Publication II**, we extended the theoretical analysis of microfibril interactions to include atomistic-level details, such as local variations in the charge distribution. Our aim was to provide new insight on the mechanisms that produce the average interaction, and the behaviour observed in experimental systems. A similar approach could be used to inform the development of chemical modification methods for improved CNF dispersion.

We carried out a series of OPLS-AA MD simulations to study how carboxylation affects the disintegration energetics of cellulose microfibril aggregates. We considered a system of two aligned microfibrils in a periodic simulation domain filled with TIP3P water (Jorgensen et al., 1983). We used the umbrella sampling method (Kästner, 2011; Torrie and Valleau, 1977), along with the weighted histogram method (WHAM) (Kumar et al., 1992), to determine the potential of mean force (PMF) of separating, or bringing together, the two microfibrils while keeping them aligned. The umbrella sampling procedure involved an initial pulling simulation, from which we obtained simulation geometries along the reaction coordinate, the inter-fibril distance[17]. Notably, we only considered inter-fibril distances above the hydrogen bonding range. Configurations obtained from the pulling simulation were used as initial structures in the respective umbrella sampling simulations. A harmonic bias potential was used to keep the inter-fibril distance fixed, and thus sample all values along the reaction coordinate equally.

The microfibril model consisted of 36 cellulose chains, each 20 glucose units long, in an arrangement with a square cross-section and hydrophilic exterior surfaces[18] (see Figure 14, left). The internal structure of the fibril was cellulose I_β. We mimicked the carboxylation process by a modification scheme, which follows the experimental findings of Saito et al. (Saito et al., 2009, 2007; Saito and Isogai, 2004) with regard to the reaction sites and their availability. The procedure involved random substitution of surface hydroxymethyl groups with charged carboxylate groups, and the addition of sodium counter-ions nearby (see Figure 14, right). We considered altogether five degrees of substitution (DS), 0 % (native cellulose), 25 %, 50 %, 75 % and 100 %, with five variants of surface charge distribution in each case.

In addition to the MD simulations, we developed a simplified, static, model to investigate the role of electrostatic forces in isolation. The model considered only the carboxylate groups and the sodium counter-ions, and represented them as point-

---

[17]Measured as the distance between the centres of mass (COM) of the two fibril segments.

[18]This fibril model was adopted from (Paavilainen et al., 2011), along with the OPLS-AA parameter set. In **Publication III**, we adjusted the fibril model with respect to the number of cellulose chains and the exposed crystallographic planes.
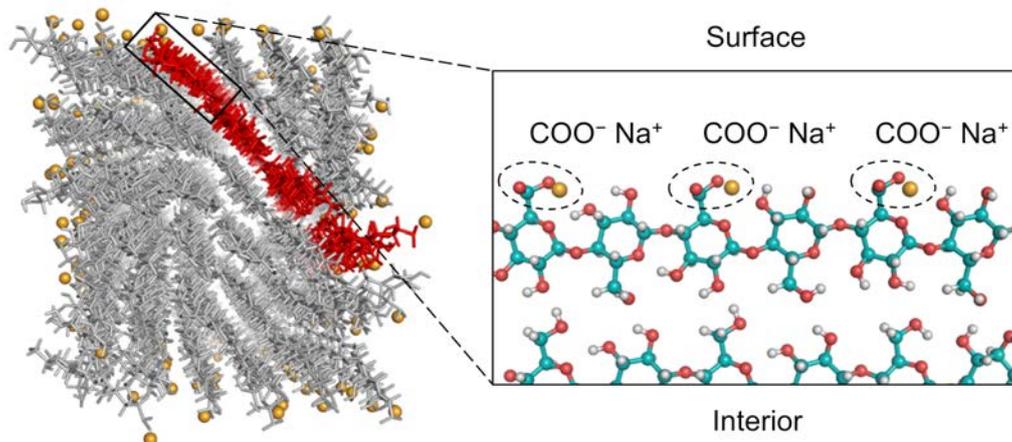
Figure 14. The 36-chain cellulose microfibril model (left) and the modification scheme (right), in which primary alcohol groups at the fibril surface are substituted with carboxylate groups and a nearby sodium counter-ion. Reprinted from (Paajanen et al., 2016) with kind permission from Springer. Copyright Springer Science+Business Media Dordrecht 2016.

like particles of negative and positive elementary charge, respectively. These particles were distributed randomly, in electrically neutral pairs, on possible carboxylate group locations on the microfibril surface.

Finally, we carried out a series of disintegration experiments on TEMPO-oxidised never-dried bleached softwood kraft pulp. Parts of this series of experiments were reported earlier by Brodin et al. (Brodin et al., 2013). Briefly, we carried out the TEMPO chemical treatment, as outlined by Saito et al. (Saito et al., 2006), with three sodium hypochlorite concentrations (2.5, 3.0 and $5.0\,\mathrm{mmol\,g^{-1}}$), and two reaction temperatures (30 and $50\,°\mathrm{C}$). We then disintegrated the TEMPO-oxidised pulps using either an Ystral Z 80-3 dispersion unit or a Microfluidics M-110P homogeniser, with two alternative rotational speeds (3000 and 5000 rpm). The disintegration involved up to 10 passes in the homogeniser. We analysed the CNF samples using a Metso FS-300 fibre analyser and AFM.

Figure 15 summarises the experimental and simulation results. As shown in Figure 15a, the grinding energy that is required to disintegrate cellulosic fibres decreases dramatically with increasing functionalisation level. This implies that the introduction of surface charge is not limited to the fibre exterior, but also takes place on the surfaces of the constituent microfibrils. The effect of increased functionalisation can also be seen in the increased homogeneity of the CNFs, as shown in the AFM images (see Figure 5 of **Publication II**). Repulsive forces between the microfibrils could explain both observations.

Figure 15b shows the averaged PMF curves determined from the umbrella sampling simulations. The decrease in PMF with increasing distance indicates an inter-fibril re-
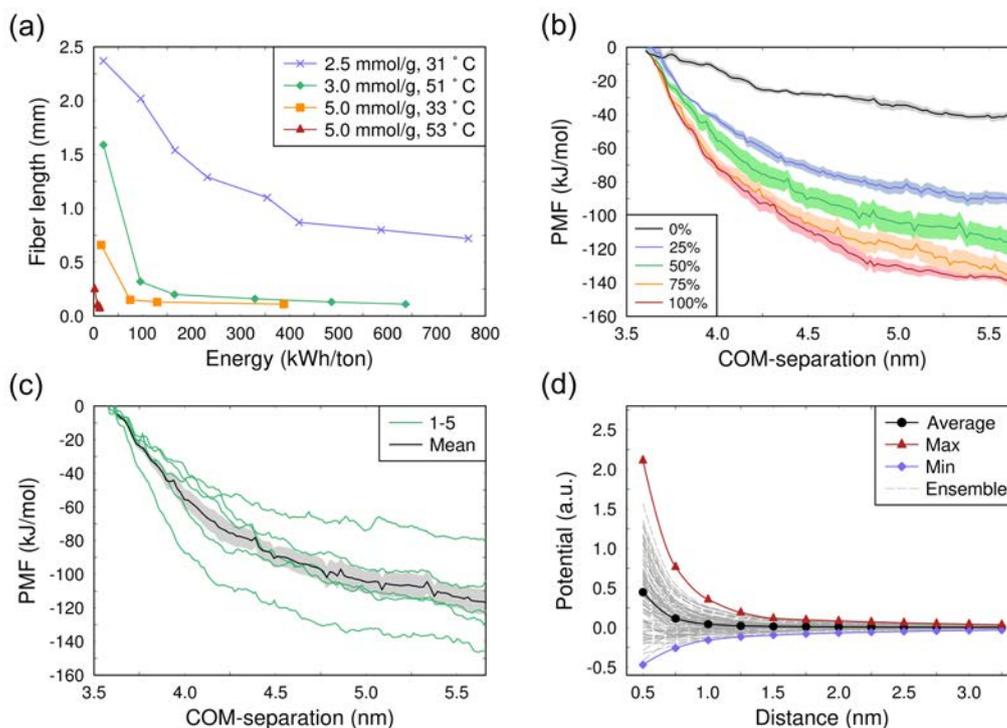
Figure 15. (a) Average fibre length as a function of grinding energy. (b) Average PMF curves, along with standard errors of the mean (solid colours). Sensitivity of the PMF to the charge distribution in (c) the umbrella sampling simulations at DS 50 %, and (d) the electrostatic calculations at DS 25 %. The inter-fibril distance is measured in terms of centre of mass separation. Reprinted from (Paajanen et al., 2016) with kind permission from Springer. Copyright Springer Science+Business Media Dordrecht 2016.

pulsion. This implies a reduction in the disintegration energy in experimental systems, or, in the case of colloidal suspensions, increased stability. Indeed, the order of the PMF curves reflects the decrease in disintegration energy with increasing functionalisation level. However, the effect is not as large as in the experiments. We could also compare the simulations against earlier DLVO predictions by Fukuzumi et al. (Fukuzumi et al., 2014), who report interaction potentials of similar magnitude but slightly longer range.

While the averaged PMF curves follow the order of the DS, there is significant variation in the curves that correspond to individual charge configurations (see Figure 15c). This is most pronounced in the case of the intermediate DS, for which the variation is as large as the separation between the averaged PMFs. This is reflected in their greater standard error of the mean (see Figure 15b). We could estimate the sensitivity of the PMF to the charge distribution using the electrostatic model. The variation turned out to be surprisingly large, with some charge configurations even leading to attractive forces (see Figure 15d). The large statistical variation suggests heterogeneous aggreg-

ation behaviour in experimental systems. Indeed, such heterogeneity was observed in the AFM micrographs (see Figure 5 of **Publication II**).

Finally, we observed the accumulation of sodium counter-ions around the surface carboxylate groups, and their dynamic exchange with the surrounding water. The resulting screening effect reduces electrostatic repulsion between the fibrils and is likely to stabilise the interaction towards larger distances. However, at shorter distances the ions can be expected to contribute to the heterogeneous behaviour, and to the instability of the parallel alignment.

Our work in **Publication II** improves the qualitative understanding of carboxylated cellulose microfibrils and their interactions. Besides reproducing the average behaviour predicted by the DLVO theory, the simulations reveal a surprising variability in the underlying contributions. Notably, local variations in the surface charge distribution could explain the heterogeneity observed in the disintegration behaviour of experimental systems. With further development, simulations of functionalised microfibrils could be used to study the effects of chemical modification on the structure of fibril aggregates. This, in turn, would help us understand the nanoscale details of fibrillation. In **Publication III**, we carried out related work on the structure of microfibril aggregates and their relationship to the bound water of the cell wall. Moreover, the aggregation and deaggregation behaviour of CNFs manifests itself in the rheology of their aqueous suspensions, which was studied in **Publication IV**.

5.3   Chirality and bound water in microfibril bundles (III)

The structural hierarchy of cellulose involves a chiral order that appears on several length scales. (Wang et al., 2013) The lowest-level observation is that of the twisting of isolated CNFs and CNCs in electron and scanning probe microscopy studies. (Arcari et al., 2019; Elazzouzi-Hafraoui et al., 2008; Hanley et al., 1997; Khandelwal and Windle, 2014; Majoinen et al., 2014; Ogawa, 2019) It is not evident that individual microfibrils behave similarly in their native environment. (Shklyaev et al., 2014; Zhang et al., 2016a) However, their organisation into helical bundles has been observed in transmission electron tomography studies (Ciesielski et al., 2013; Reza et al., 2017), and similar behaviour has been reported for bundles of isolated CNFs and CNCs (Dong and Gray, 1997; Usov et al., 2015; Conley et al., 2017). The helical winding of macrofibrils around wood cells (Barnett and Bonham, 2004) and the twisting of cellulosic fibres (Burgert et al., 2005) and fibre networks (Yu et al., 2004) continue the same pattern.

It is not obvious whether and how the behaviours at the different scales are related. Explanations for the chirality transfer from cellulose macrofibrils to fibres and fibre networks have been given using continuum models (Burgert et al., 2005; Ten Bosch, 1996). Similarly, the molecular-level origins of microfibril twist have been detailed in

several atomistic simulation studies (Bu et al., 2015; Conley et al., 2016; Hadden et al., 2013; Kannam et al., 2017; Matthews et al., 2006; Paavilainen et al., 2011; Yui et al., 2006; Yui and Hayashi, 2007; Zhao et al., 2013). In **Publication III**, we extended the computational analysis to involve microfibril bundles. We used classical MD simulations to show how chirality—as manifested by twisting about the longitudinal axis—is transferred from microfibrils to their bundles, and how interactions with water affect these structural units.

We carried out OPLS-AA MD simulations of microfibrils and their bundles in both vacuum and water environments. We first simulated individual fibrils in vacuum, until they would adopt an equilibrium twist about their longitudinal axis. We then carried out simulated aggregation of four such fibrils, and, again, simulated the bundle in vacuum until it would adopt an equilibrium twist (of the fibrils about the bundle axis). Lastly, we carried out simulations of both the individual fibrils and the bundle in water, to study their qualitative response to changing moisture content.

The microfibril model consisted of 24 cellulose chains, each 40 glucose units long, in an arrangement with a hexagonal cross-section (see Figure 16a).[19] In its initial state, the microfibril had the cellulose I$_\beta$ structure. The number of chains and their arrangement were based on combined evidence from small-angle X-ray scattering (SAXS), WAXS, solid-state NMR and Fourier-transform infrared spectroscopy (FTIR) experiments. (Fernandes et al., 2011; Wang and Hong, 2016) The hexagonal cross-section results in an amphiphilic exterior surface, while 24 is the smallest six-multiple number of chains that results in a three-layered structure with surface (that is, solvent-exposed), surface-bound, and core chains. The requirement for a six-multiple of chains comes from the structure of the cellulose synthase complex (see Chapter 3). Figure 16b shows the structure of the microfibril bundle, which consists of four fibrils and six loose cellulose chains added between to represent hemicellulose.

In addition to the MD simulations, we carried out experiments to determine the bound water content of bleached birch kraft and dissolving pulps, and, for the former, the twist rate of air-dried fibres. Measurements of the non-freezing and freezing bound water content were based on thermoporosimetry and involved both never dried and heat-treated pulps. The fibre twist rates were determined from SEM micrographs. We also considered previously published porosity measurements on the same materials (Lovikka et al., 2016). These measurements were carried out in both dry and wet states, using (i) solvent exchange, critical point drying and N$_2$ sorption, and (ii) two-point solute exclusion and dextran probes, respectively.

The simulations show a coupling between the microfibril and bundle twist, conformational disorder, and water interactions. We compared the simulations with sev-

---

[19]As noted earlier, the fibril model differs from that of **Publication II**. Here, we adjusted the number of cellulose chains and the exposed crystallographic planes according to the cited studies. For further details, see **Publication III**.
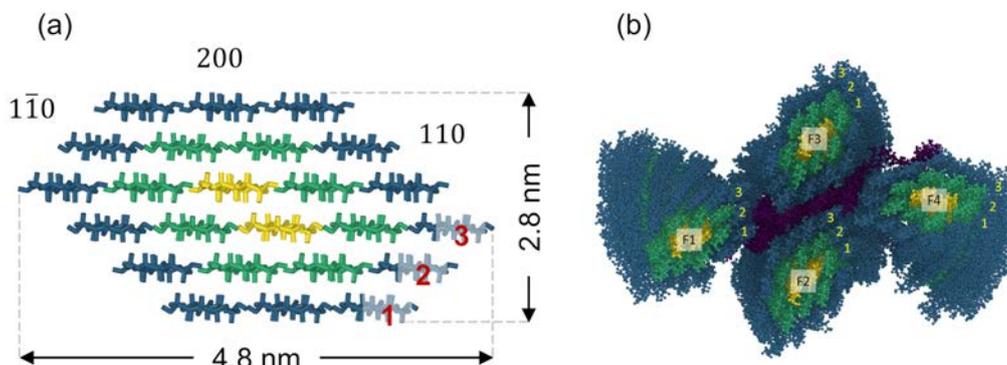
Figure 16. Geometry of the microfibril and bundle models: (a) cross-section of an individual fibril, and (b) segment of the fibril bundle, both seen from the non-reducing end. Surface, surface-bound and core chains are coloured blue, green and yellow, respectively. Loose chains between the fibrils are coloured purple. Three surface chains are labelled for improved readability.

eral measurable quantities at different levels of the structural hierarchy (see Table 1 of **Publication III**). These comparisons use both earlier experiments and the current ones.

In the vacuum simulations of single fibrils, the longitudinal twist rate converged at 3.6 °/nm. When immersed in water, the vacuum-equilibrated fibril would twist further, reaching an equilibrium rate of 4.2 °/nm. The dynamics of twisting was similar in both environments: first a rapid relaxation phase of less than one nanosecond, followed by a gradual increase over several hundreds of nanoseconds (see Figure 17a). We obtained an experimental estimate for the microfibril twist rate from previously published AFM and transmission electron microscopy (TEM) micrographs on isolated CNFs and CNCs. (Ding et al., 2014; Usov et al., 2015) The experimental twist rate, 4.2 °/nm, turns out to be the same as that observed in our simulations.

In the vacuum simulation of the fibril bundle, the longitudinal twist rate of the bundle saturated at a level of 0.8 °/nm, and, when immersed in water, further increased to 0.9 °/nm (see Figure 17c). Again, we could compare the prediction against estimates based on the micrographs. The experimental twist rates of 1.1–1.9 °/nm, which represent different-sized bundles, are remarkably close. Moreover, in their transmission electron tomography study, Reza et al. report twist rates of 0.9–1.0 °/nm for microfibril bundles in spruce secondary cell walls. (Reza et al., 2017) Conley et al. estimate a lower twist rate of 0.2 °/nm for larger CNC bundles by means of circular dichroism spectroscopy and electronic structure calculations. (Conley et al., 2017) Interestingly, the aggregation did not affect the twist rates of the constituent fibrils significantly. There seemed, however, to be a coupling between the twisting behaviour of the two
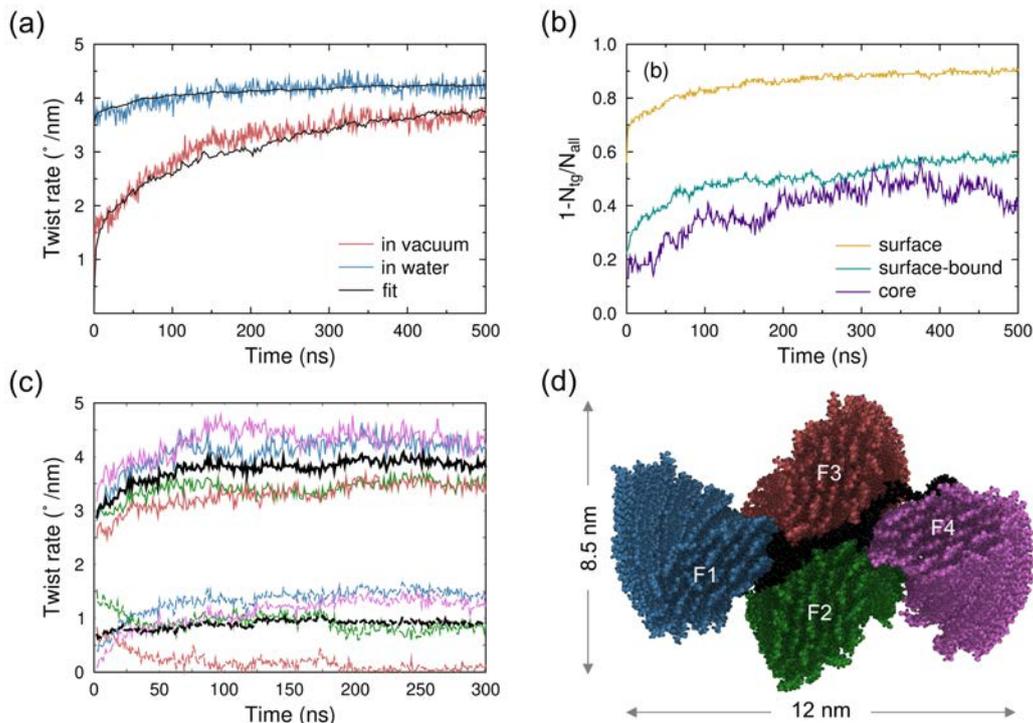
Figure 17. (a) Microfibril twist rate in the single fibril simulations, both in vacuum and in water. The black curves correspond to linear fits between the fraction of non-tg primary alcohol group conformers and the twist rate. (b) Conformational changes in water, measured as the fraction of non-tg primary alcohol group conformers. (c) Bundle (dashed curves) and microfibril (solid curves) twist rates in the bundle simulation. The colour legend is given by (d) the molecular visualisation. The black curves represent the average twist rate.

peripheral fibrils and between the two central ones.

The fibril and bundle twist rates roughly follow the inverse-diameter scaling law predicted for cellulosic fibres (Ten Bosch, 1996) and observed in atomistic simulations of individual fibrils (Hadden et al., 2013; Zhao et al., 2013). This happens despite the separate twisting of the constituent fibrils. Interestingly, the behaviour extends two orders of magnitude to the fibre level: the twist rate extrapolated to a fibre of diameter $2.5\,\mu$m, $4.1 \times 10^{-3}\,°/$nm, agrees with the experimental value $3.5 \times 10^{-3}\,°/$nm.

The microfibril twist was always associated with an increasing disorder of the primary alcohol group conformations. Starting from the solvent-exposed chains, the initial tg conformers would gradually transition to a blend of tg, gt and gg conformers, with the amount of disorder decreasing towards the core chains. The time evolution of the twist rate and that of the conformational changes were strikingly similar. Indeed, we found a linear relationship between the conversion from tg to other conformers and the twist rate (see Figure 17a, b). The overall level of conformational disorder was similar to that reported by Fernandes et al. (Fernandes et al., 2011; Jarvis, 2018) in
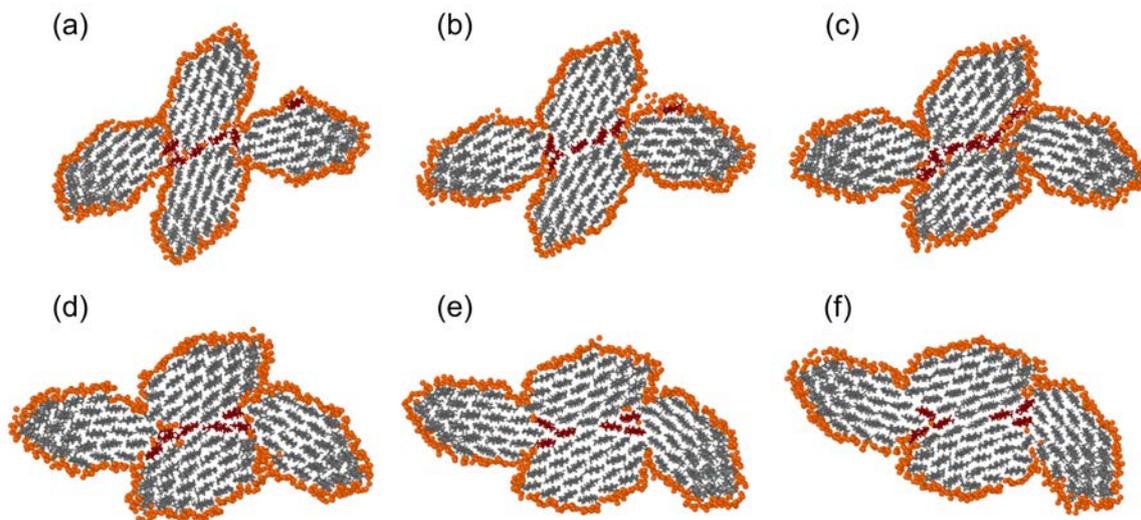
Figure 18. Microfibril bundle cross-sections at various locations along its length (a–f from non-reducing to reducing end). Microfibrils are coloured grey, interfacial cellulose chains red, and nearby water molecules orange.

their solid-state NMR experiments.

The simulated aggregation results in a bundle with significant structural variation (see Figure 18). The twisting of the constituent fibrils prevents their co-crystallisation, and results in changing surface contacts along the length of the bundle. This, in turn, results in narrow crevices at some locations, which allows water to enter the bundle. Moreover, the specific surface area (that is, circumference) of the bundle and the solvent-exposed crystallographic planes varies along its length.

We observed some diffusion of water into the bundle interior (see Figure 18c, d), but the amount of such water was negligible compared to the experimental observations on non-freezing and freezing bound water (0.52–$0.76\,\mathrm{g_{water}/g_{cellulose}}$). Another place to look for the bound water is on the microfibril surfaces. The hydration of cellulose nanocrystals has been shown to involve the adsorption of roughly three monolayers of water molecules. (Niinivaara et al., 2015) In our simulations, the amount of water within the range of hydrogen bonding corresponded to approximately one monolayer, or $0.19\,\mathrm{g/g}$. This is close to the amount of NFW in the never-dried pulps, 0.22–$0.23\,\mathrm{g/g}$. Moreover, the next two water layers constitute $0.49\,\mathrm{g/g}$, which is close to the amount of FBW in the never-dried pulps, 0.42–$0.46\,\mathrm{g/g}$.

We could also compare specific surface areas against a series of nitrogen sorption experiments (Lovikka et al., 2016). We obtained an estimate for the specific surface area of the BDHW-ND pulp by extrapolating the nitrogen sorption-based values to the fibre saturation point. The extrapolated value, $470\,\mathrm{m^2\,g^{-1}}$, is not far from the specific surface area of the bundle, 520–$630\,\mathrm{m^2\,g^{-1}}$.

Finally, we could compare the fraction of cellulose hydroxyl groups accessible to water with values obtained from deuteration-FTIR experiments (Fernandes et al., 2011; Väisänen et al., 2018). The fraction of accessible hydroxyl groups, 25 % for the microfibril and 20 % for the bundle, was somewhat lower than the experimental values, 28–50 %.

Our work in **Publication III** reveals interesting interrelations between the chirality, conformational disorder and bound water in cellulose microfibril bundles. It is notable, that the simulations reproduce several experimental observations with reasonable accuracy. These include the magnitude of the microfibril and bundle twist, the type and degree of conformational disorder, the specific surface areas, the mass fractions of non-freezing and freezing bound water, and the fraction of water-accessible hydroxyl groups. Moreover, the predicted twisting behaviour can qualitatively explain the repeating patterns observed in AFM imaging studies (Ding et al., 2014; Usov et al., 2015), which challenges the conventional picture of a cellulose microfibril with repeating amorphous segments along its length.

MD simulations of microfibril bundles can be directly applied to study many fundamental properties of cellulosic materials. One of these is the swelling behaviour of cellulosic fibres with increasing moisture content. Direct simulation of the water-induced swelling of microfibril bundles could help us understand the mechanisms by which water affects the macroscopic properties of fibres. Such simulations would look at the routes of water penetration and the associated diffusion rates, the induced morphological changes, and the implications for the strength and dimensional stability of larger structural units.

5.4   Rheology of cellulose-based hydrogels (IV)

Cellulose-based hydrogels have shown promise in medical applications that require a biocompatible material with low cytotoxicity. (De France et al., 2017) Their thixotropic quality also makes them feasible inks for 3D printing, which further extends the range of technological possibilities. As an example, CNF-based hydrogels could be used in personalised wound dressings that gradually release therapeutic agents to promote healing (Abeer et al., 2014; Kucińska-Lipka et al., 2015). Both the application environment and the manufacturing process set requirements for the material. In the wound dressing example, the printed structure should exhibit dimensional stability, support cell adhesion and proliferation, and act as a moisture regulator. At the same time, printability requires suitable rheological behaviour. The ink should be shear-thinning, so that it flows during extrusion, but it should also retain its shape after deposition. The rheological behaviour is determined by the build-up and breakdown of the gel network in changing flow conditions, which, in the case of CNF hydrogels, can be traced to the interactions between cellulose microfibrils. (Mewis and Wagner, 2009) The various

requirements pose a challenge for material design and process optimisation. In **Publication IV**, we used rheometry, printing experiments and CFD simulations to study the behaviour of a CNF-based hydrogel formulation during direct-write printing. Our aim was to predict dependencies between printing parameters, such as the geometry of the printer head and the operating pressure, and process conditions and outcomes, such as mass flux, line resolution, and shear stress levels. The work also involved several other aspects of material development and characterisation. However, the following discussion focuses on the rheology and flow behaviour.

The printing paste formulations involved TEMPO-oxidised CNFs (TCNF) and water, as well as a blend of TCNF, alginate, glycerin and water. Four paste formulations were chosen for detailed characterisation (see Table 1). In two of these, some of the water was replaced with glycerin to reduce excessive shrinking due to evaporation. The rheometry, printing experiments and CFD simulations considered the TCNF and ATG50 hydrogels.

Table 1. Printing paste formulations.

Sample ID	alginate / TCNF (% w/w)	water (% w/w)	glycerin (% w/v)
TCNF	0 / 100	99	0
AT	66 / 33	96	0
ATG30	85 / 15	65	30
ATG50	90 / 10	45	50

Never-dried bleached hardwood kraft pulp was used to prepare the TCNF. The chemical pre-treatment, TEMPO-mediated oxidation, was performed as in (Saito et al., 2006). The oxidised pulp was then diluted to 1% solids, dispersed in a high-shear mixer, and fed twice through a microfluidiser. The resulting hydrogel was viscous and transparent, and had a $1.06\,\mathrm{wt}\%$ dry matter content and a $1.1\,\mathrm{mmol\,g^{-1}}$ dry pulp carboxylate content. The TCNF hydrogel served as a basis for the formulations containing alginate. A sodium alginate powder was directly mixed with the TCNF hydrogel when no glycerin was used. Otherwise, it was first mixed with glycerin, and the TCNF hydrogel was then added and blended. The sodium alginate powder had a medium ratio of mannuronic acid to guluronic acid.

Rotational rheometer measurements were used to determine the hydrogels' dynamic viscosity at steady-state and transient shearing conditions, as well as their yield flow behaviour. An Anton Paar MCR 301 rheometer was used for the measurements, equipped with three types of measuring heads: plate-plate (PP), concentric cylinders (CC), and vane-spindle and cylindrical cup. The steady-state experiments involved measuring each shear rate long enough for the viscosity to converge. The transient experiments

began with pre-shearing at a constant rate, followed by a sudden increase or decrease by several orders of magnitude. Shear rates were considered within the limits of the equipment, between 1×10^{-4} and $3.16 \times 10^{3}\,\mathrm{s}^{-1}$. The yield flow measurements used the stress ramp method, with rates of stress increase between 0.2 and $1.7\,\mathrm{Pa\,s}^{-1}$.

Two kinds of printing experiments were used to determine dependencies between operating pressure, mass flux, printing speed and line resolution. The mass flux experiments involved dispensing hydrogel on a substrate for a given time with a given operating pressure, after which the sample was weighed. The used pressures ranged from 1 to 30 psi. The line resolution experiments involved printing straight lines of hydrogel on a graph substrate with a given printer head speed, height from the substrate, and operating pressure. The profiles of the printed lines were then determined based on image analysis of high-resolution photographs, or, alternatively, measurements with an optical profilometer. The used pressures ranged from 1 to 10 psi. The printing experiments were performed using nScrypt micro-dispensing equipment. The TCNF hydrogel was printed using cylindrical steel tips of 0.2 and 0.51 mm inner diameter, and the ATG50 hydrogel using a conical plastic tip of 0.41 mm inner diameter at the narrow end. Three repetitions of the printing experiments were carried out for each set of printing parameters.

Analogous to the printing experiments, two kinds of CFD models were used to study how the hydrogels behave during printing. Firstly, printer head simulations were used to examine how the mass flux and the associated shear stress levels depend on the operating pressure. A regular axisymmetric mesh was used to describe both printer head geometries (see Figure 19a). In the case of the steel tip, only the straight cylindrical part was considered, as it dominates the pressure losses. The printing paste inlet was treated using a uniform velocity boundary condition, the outlet using a zero-pressure boundary condition, and the interior surfaces using a no-slip[20] boundary condition.

Secondly, deposition simulations were used to predict how the printed line profile depends on the operating parameters. The deposition geometry was described using a hexahedral mesh with boundary conditions representing the printer head, the substrate, and the five open-air boundaries (see Figure 19b). The printer head, located at the upper boundary, was described using a circular inlet with a uniform velocity boundary condition. Similarly, uniform velocity boundary conditions at the substrate and the front open-air boundary were used to simulate the movement of the printer head. The remaining boundaries with open air were treated as far-field boundaries (top and sides) and an outlet boundary (back). The VOF method was used to track the hydrogel-air interface, and the air was described as a Newtonian fluid. The standard k-ε model was used to account for turbulence. The power-law fluid model was used to describe the

---

[20]The possibility of slip flow should be kept in mind when interpreting rheological data on CNF suspensions. (Turpeinen et al., 2019; Vadodaria et al., 2018)
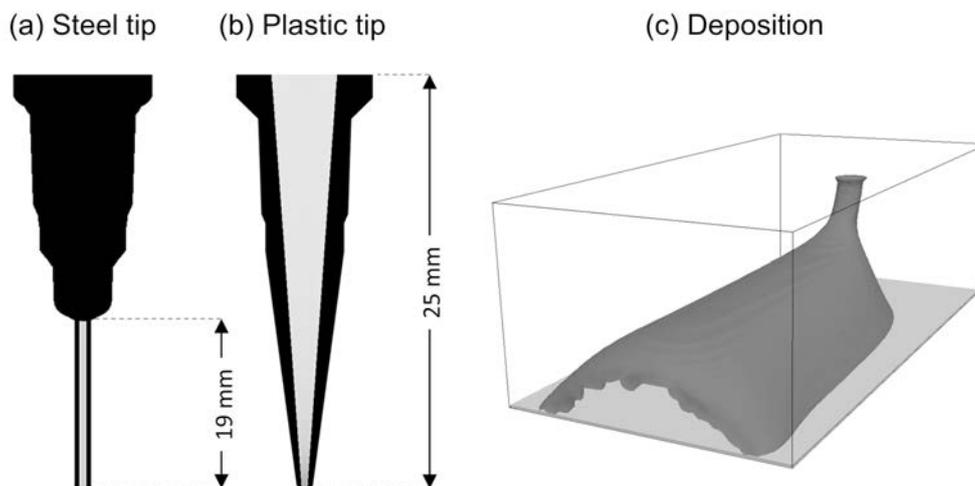
Figure 19. Simulation geometries for hydrogel flow (a) within the cylindrical steel tip and (b) within the conical plastic tip, and (c) during deposition. In (a) and (b), the light grey colouring indicates the simulation domain. In (c), the dark grey surface indicates the air-hydrogel interface.

hydrogel.

Figure 20 summarises the experimental and simulation results for the TCNF hydrogel. The ATG50 results are given in **Publication IV**, sections 3.2, 3.3 and 3.4. The steady-state rheometer results are shown in Figure 20a. The dynamic viscosity displays regular power-law behaviour, with no levelling at either low or high shear rates. That is, the asymptotic values are beyond the reach of the rotational rheometer experiments. Figure 20b demonstrates the thixotropic behaviour observed in the transient rheometer experiments. The thixotropic recovery of viscosity can be seen after the sudden decrease in shear rate. Moreover, yield flow behaviour was observed in the stress-ramp measurements, with a yield stress of 45 Pa.

Figure 20c shows the dependence between mass flux and operating pressure in the printing experiments and the corresponding CFD simulations. The simulations that rely on the rheometry-based power-law model seriously overestimate the mass flux (dashed lines in Figure 20c). Such behaviour could be expected, if the hydrogel's viscosity deviates from the power-law model beyond the experimental shear rates. Specifically, if there is less shear thinning towards higher shear rates. To investigate this possibility, we treated the situation as an inverse problem. We carried out a series of printer head simulations to fit the power-law model against the mass-flux measurements (solid line in Figure 20c). We then compared the predicted viscosities against the rheometer measurements. The comparison is shown in Figure 20a, where the dashed line indicates the power law model fitted against the printing experiments. The predicted viscosities represent, for the most part, an intermediate between the measurements
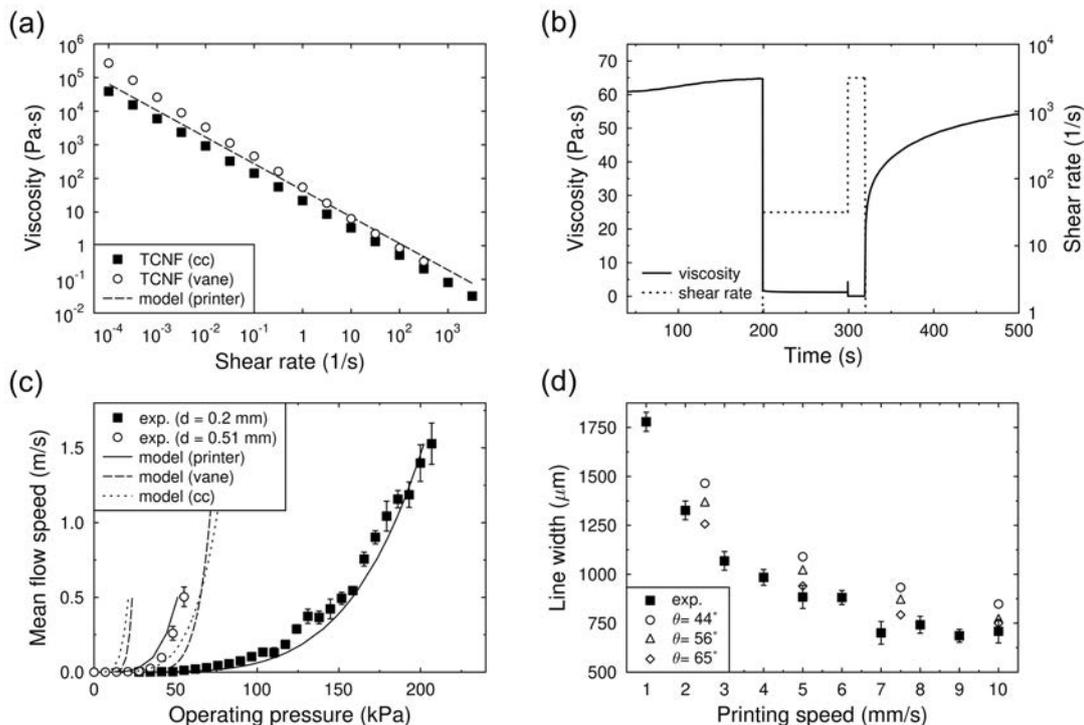
Figure 20. Results of the rheometer and printing experiments, and the corresponding simulations, for the TCNF hydrogel: (a) steady-state viscosity as a function of shear rate, and (b) thixotropic recovery of viscosity in the rheometer experiments; (c) volumetric flow within the printer head as a function of pressure, and (d) line resolution as a function of printer head speed in the printing experiments.

with different geometries. However, the flow behaviour index is slightly larger, which corresponds to less shear thinning, and a more viscous fluid, towards higher shear rates. Thus, it seems that the hydrogel's viscosity deviates from the power law model, and that the behaviour at high shear rates dictates the pressure losses within the printer head. Indeed, we observed shear rates up to $10^5 \, \mathrm{s}^{-1}$ in the printer head simulations, which is well beyond the measured range. However, others have measured CNF suspensions up to such rates, and have observed the levelling of the power-law behaviour above $10^3 \, \mathrm{s}^{-1}$. (Kumar et al., 2016)

Lastly, Figure 20d shows the dependence between line resolution and printer head speed in the printing experiments and the corresponding CFD simulations. The predictions overestimate the line resolution by 50–100 µm, depending on the pre-defined hydrogel-substrate contact angle. Indeed, much of the uncertainty can be traced to the hydrogel's behaviour in the goniometer experiments, where repeated measurements could not yield a unique value for the contact angle. Nevertheless, the deviations are systematic, and the predictions stay within 6–13 % of the measured values, which is already a reasonable accuracy for practical use. In contrast to the mass flux predic-

tions, the line resolution was not sensitive to the hydrogel's high shear rate behaviour. Thus, the rheometry-based power-law fluid model was adequate for the deposition simulations.

Our work in **Publication IV** demonstrates the coordinated use of rheometry, printing experiments and CFD simulations in the development of CNF-based hydrogel formulations for 3D printing. The rheometer experiments confirm and quantify the shear-thinning and yield flow behaviours, both of which are required from a printing paste. Moreover, they reveal the time scale of thixotropic recovery, which can have significant consequences in suddenly changing flow conditions, such as those during deposition. The printing experiments confirm the printability of the hydrogel and its dimensional stability after deposition. They also provide information on how the printing outcome depends on the operating parameters. However, the dimensionality of the parameter space is too high for a thorough experimental sampling. With a justifiable rheological model, the CFD simulations can be used to complement the mapping between operating parameters and outcomes, which gives more control over the additive manufacturing process.

Importantly, our simulations indicate that the pressure loss within the printer head is dictated by the high shear rate behaviour of the hydrogel, which can be beyond the reach of conventional rheometer experiments. The rheological characterisation should, perhaps, be complemented with methods such as capillary viscometry, which we essentially did in the mass flux experiments. The opposite is true in the deposition process, where the low shear rate behaviour dominates. It is noteworthy, that knowledge of the shear stress levels also enables the estimation of cell viability when printing biological matter. (Müller et al., 2017) An alternative approach would be to study how changes to the hydrogel's rheology affect its printing behaviour. Such simulations could be used to establish boundaries for ideal rheology, which, in turn, could steer the material development process.

6   Conclusions and outlook

This thesis consists of molecular and fluid dynamics simulation studies on fundamental structural and thermochemical properties of cellulose. The work covers the structural hierarchy of native cellulose, with simulations on individual chains (Publication I), microfibrils (Publication II), microfibril bundles (Publication III) and bundle networks (Publication IV). The findings contribute to our understanding of the pyrolytic degradation of cellulose, its hierarchical structure, its chemical modification and the rheology of CNF suspensions. Moreover, they have implications for technological applications.

Cellulose pyrolysis. We evaluated the capability of ReaxFF-MD to predict the reaction pathways and kinetics of cellulose pyrolysis. We chose to first look at primary reactions in the gas-phase, and, based on the lessons learned, build towards condensed-phase simulations involving secondary and tertiary reactions. Our results demonstrate that ReaxFF-MD can predict essential features of the degradation process, most notably its onset via glycosidic bond cleavage. Moreover, the associated reaction kinetics is compatible with the experimental literature.

Encouraged by the results, we continue to work on simulations of condensed-phase systems.[21] One of the key questions is whether ReaxFF-MD can predict the formation of LGA, an important product of cellulose fast pyrolysis. In the end, we hope to predict reaction pathways that lead to the known major products, along with the kinetics of the rate-determining reactions. We also work on simulations that address the effects of chemical modification, for example phosphorylation, on the degradation pathways. Such capability would be valuable, among others, to support the design, development and optimisation of flame-retardant chemistries.

Structure of microfibril bundles. We studied the structure of microfibril bundles and their relationship to the bound water of the cell wall. Our simulations reproduce several experimentally known features of native cellulose. They give reasonable predictions on the mass fraction of non-freezing and freezing bound water, the fraction of water-accessible hydroxyl groups, the specific surface area, and the conformational disorder of surface and surface-bound chains. The simulations suggest that microfibril bundles inherit their chirality from the constituent fibrils. Moreover, the predicted magnitudes of the microfibril and bundle twist agree with experimental data on isolated CNFs and CNCs and native microfibril bundles. Mismatch in the twist rates prevents co-crystallisation and leads to repeated openings along the bundle. Such openings could become initiation sites of defects during chemical and mechanical processing. Our results suggest that both non-freezing and freezing bound water can be associated with molecular water layers surrounding the fibrils.

Atomistic simulation of microfibril bundles opens new ways to probe fundamental properties of cellulose. Accordingly, the work can continue in several directions. For ex-

---

[21]The work continues in the FISAMA project (2016–2020).

ample, it would be interesting to study the nanoscale structure and moisture behaviour of wood using simulation-assisted X-ray scattering analysis. Specifically, simulations of moisture-induced swelling could be used to associate changes in scattering patterns with nanoscale structural changes. This would lead to an improved understanding of the wood cell wall structure, and the mechanisms by which water affects its properties. Such knowledge is essential for the optimisation of chemical and enzymatic treatments, and, consequently, for the efficient use of wood and other lignocellulosic precursors.

Chemical modification of cellulose. We studied the aggregation and deaggregation energetics of native and chemically modified microfibrils. Our work describes in detail how surface carboxylation affects the interaction between neighbouring microfibrils, and reveals a surprising variability in the electrostatic contributions that constitute the average interaction. This leads us to believe that local variations in surface charge distribution could cause molecular-level failures along fibril-fibril interfaces. Such defects could trigger local disintegration processes, and thus explain the heterogeneity observed in the disintegration behaviour of TEMPO-oxidised pulp at intermediate functionalisation levels.

With further development, simulations of functionalised microfibrils could be used to address the effects of chemical modification on the structure of microfibril bundles, and their breakdown during fibrillation. This could build on studies of moisture-induced swelling, which affects the accessibility of cellulose to chemical treatments. The interactions of functionalised microfibrils also have implications for aqueous dispersions of cellulose nanoparticles. For example, colloidally stable CNCs can form liquid crystalline phases, the behaviour of which depends on their aspect ratio and surface chemistry. Here, molecular simulations could be used to address the details of their self-assembly, or to support the development of chemical treatments for improved dispersion.

Rheology of CNF-based hydrogels. Microfibril interactions also manifest themselves in the rheology of aqueous CNF suspensions. We demonstrated the coordinated use of rheometry, printing experiments and CFD simulations to assist the development of CNF-based hydrogel formulations for 3D printing. The rheometer experiments confirm and quantify the shear-thinning and yield flow behaviours and reveal the time scale of thixotropic recovery. The printing experiments confirm the printability and dimensional stability after deposition. CFD simulations of printer head flow reveal how mass flux and shear stress levels depend on the hydrogel's rheology, the printer head geometry, and the operating parameters. Our results highlight the sensitivity of the flow behaviour to the rheological description, and the need for advanced characterisation to build reliable models.

Cellulose-based materials can exhibit complex flow behaviour, including apparent wall slip, shear banding and thixotropy. For this reason, conventional rheometry may not be enough to form an accurate rheological description. In such cases, CFD sim-

ulations could be used to support the data analysis. For example, computationally inexpensive pipe flow simulations could be used to parameterise rheological models with different levels of approximation. The predictive power of these models would provide indirect evidence on the role of wall slip and other problematic behaviour. Similarly, CFD simulations could be used to study how changes in the hydrogel's rheology affect its printing behaviour, and to establish boundaries for an ideal rheology. Such information could be used to steer the material development process, and thus reduce the need for trial and error.

In summary, the main contributions of this thesis to the field of computational cellulose research are the following: Publication I shows the applicability of reactive force field methods for predicting mechanisms and kinetics of cellulose pyrolysis. This approach, which has not been demonstrated before, complements the established methods of quantum chemistry and experimental analytics. Publication II elaborates on the effects of chemical modification on microfibril interactions. The atomistic simulations address details that are not covered by previous theoretical models, and reveal the sensitivity of the interaction to non-uniform substitution patterns. The atomistic simulations of Publication III expand on previous studies that focus on individual fibrils. Perhaps most notably, the simulations predict the spontaneous formation of a twisted ribbon-like bundle with a twist rate compatible with recent experimental evidence. Lastly, Publication IV demonstrates the parameterisation of rheological models for CNF-based hydrogels, and their use in CFD simulations of printer head flow and subsequent deposition. One of the key findings is the inadequacy of rotational rheometry as a basis for models of printer head flow, and the consequent need for an alternative model building strategy.

References

Abeer, M. M., Mohd Amin, M. C. I., and Martin, C. (2014). A review of bacterial cellulose-based drug delivery systems: Their biochemistry, current approaches and future prospects. *Journal of Pharmacy and Pharmacology*, 66(8):1047–1061.

Abraham, M., van der Spoel, D., Lindahl, E., and Hess, B. (2019). *GROMACS User Manual version 2019.3*.

Agarwal, V., Dauenhauer, P. J., Huber, G. W., and Auerbach, S. M. (2012). Ab initio dynamics of cellulose pyrolysis: Nascent decomposition pathways at 327 and 600°C. *Journal of the American Chemical Society*, 134(36):14958–14972.

Allen, M. and Tildesley, D. (1987). *Computer Simulation of Liquids*. Oxford University Press, New York.

Andersen, H. C. (1980). Molecular dynamics simulations at constant pressure and/or temperature. *The Journal of Chemical Physics*.

Arcari, M., Zuccarella, E., Axelrod, R., Adamcik, J., Sánchez-Ferrer, A., Mezzenga, R., and Nyström, G. (2019). Nanostructural properties and twist periodicity of cellulose nanofibrils with variable charge density. *Biomacromolecules*, 20(3):1288–1296.

Ashraf, C. and van Duin, A. C. (2017). Extension of the ReaxFF combustion force field toward syngas combustion and initial oxidation kinetics. *The Journal of Physical Chemistry A*, 121(5):1051–1068.

Asikainen, S. (2015). *Applicability of fractionation of softwood and hardwood kraft pulp and utilisation of the fractions*. Doctoral thesis, Aalto University.

Barnes, H. A. (1997). Thixotropy—a review. *Journal of Non-Newtonian Fluid Mechanics*, 70(1-2):1–33.

Barnes, J. and Hut, P. (1986). A hierarchical O(N log N) force-calculation algorithm. *Nature*, 324(6096):446–449.

Barnett, J. R. and Bonham, V. A. (2004). Cellulose microfibril angle in the cell wall of wood fibres. *Biological Reviews of the Cambridge Philosophical Society*, 79(2):461–472.

Berendsen, H. J. C., Postma, J. P. M., van Gunsteren, W. F., DiNola, A., and Haak, J. R. (1984). Molecular dynamics with coupling to an external bath. *The Journal of Chemical Physics*, 81(8):3684–3690.

Bird, R. B., Stewart, W. E., and Lightfoot, E. N. (2006). *Transport Phenomena*. John Wiley & Sons, Inc., revised 2nd edition.

Bollhöner, B., Prestele, J., and Tuominen, H. (2012). Xylem cell death: Emerging understanding of regulation and function. *Journal of Experimental Botany*, 63(3):1081–1094.

Bondeson, D., Mathew, A., and Oksman, K. (2006). Optimization of the isolation of nanocrystals from microcrystalline cellulose by acid hydrolysis. *Cellulose*, 13(2):171–180.

Born, M. and Oppenheimer, R. (1927). Zur quantentheorie der molekeln. *Annalen der Physik*, 389(20):457–484.

Brackbill, J., Kothe, D., and Zemach, C. (1992). A continuum method for modeling surface tension. *Journal of Computational Physics*, 100(2):335–354.

Bradbury, A. G., Sakai, Y., and Shafizadeh, F. (1979). A kinetic model for pyrolysis of cellulose. *Journal of Applied Polymer Science*, 23(11):3271–3280.

Brett, C. T. (2000). Cellulose microfibrils in plants: Biosynthesis, deposition, and integration into the cell wall. *International Review of Cytology*, 199:161–199.

Brodin, F. W., Sonavane, Y., and Theliander, H. (2013). Preparation of absorbent foam based on softwood kraft pulp: Advancing from gram to kilogram scale. *BioResources*, 8(2):2099–2117.

Bu, L., Himmel, M. E., and Crowley, M. F. (2015). The molecular origins of twist in cellulose I_β. *Carbohydrate Polymers*, 125:146–152.

Buchanan, B. B., Gruissem, W., and Jones, R. L., editors (2015). *Biochemistry and molecular biology of plants*. Wiley Blackwell, 2nd edition.

Buckingham, R. (1938). The classical equation of state of gaseous helium, neon and argon. *Proceedings of the Royal Society of London. Series A. Mathematical and Physical Sciences*, 168(933):264–283.

Burgert, I., Frühmann, K., Keckes, J., Fratzl, P., and Stanzl-Tschegg, S. (2005). Properties of chemically and mechanically isolated fibres of spruce (Picea abies[L.] Karst.). part 2: Twisting phenomena. *Holzforschung*, 59(2):247–251.

Burnham, A. K., Zhou, X., and Broadbelt, L. J. (2015). Critical review of the global chemical kinetics of cellulose thermal decomposition. *Energy & Fuels*, 29(5):2906–2918.

Burton, R. A., Gidley, M. J., and Fincher, G. B. (2010). Heterogeneity in the chemistry, structure and function of plant cell walls. *Nature Chemical Biology*, 6(10):724–732.

Bussi, G., Donadio, D., and Parrinello, M. (2007). Canonical sampling through velocity rescaling. *The Journal of Chemical Physics*, 126(1):014101.

Chen, P., Nishiyama, Y., and Mazeau, K. (2014). Atomic partial charges and one Lennard-Jones parameter crucial to model cellulose allomorphs. *Cellulose*, 21(4):2207–2217.

Chenoweth, K., van Duin, A. C. T., and Goddard, W. a. (2008). ReaxFF reactive force field for molecular dynamics simulations of hydrocarbon oxidation. *The journal of physical chemistry. A*, 112(5):1040–1053.

Choudhuri, A. R. (1998). *The Physics of Fluids and Plasmas: An Introduction to Astrophysicists*. Cambridge University Press, Cambridge.

Chowdhury, R. A., Nuruddin, M., Clarkson, C., Montes, F., Howarter, J., and Youngblood, J. P. (2019). Cellulose nanocrystal (CNC) coatings with controlled anisotropy as high-performance gas barrier films.

Ciesielski, P. N., Matthews, J. F., Tucker, M. P., Beckham, G. T., Crowley, M. F., Himmel, M. E., and Donohoe, B. S. (2013). 3D electron tomography of pretreated biomass informs atomic modeling of cellulose microfibrils. *ACS Nano*, 7(9):8011–8019.

Conley, K., Godbout, L., Whitehead, M. A., and Van De Ven, T. G. (2016). Origin of the twist of cellulosic materials. *Carbohydrate Polymers*, 135:285–299.

Conley, K., Whitehead, M. A., and van de Ven, T. G. M. (2017). Probing the structural chirality of crystalline cellulose with induced circular dichroism. *Cellulose*, 24(2):479–486.

Cornell, W. D., Cieplak, P., Bayly, C. I., Gould, I. R., Merz, K. M., Ferguson, D. M., Spellmeyer, D. C., Fox, T., Caldwell, J. W., and Kollman, P. A. (1995). A second generation force field for the simulation of proteins, nucleic acids, and organic molecules. *Journal of the American Chemical Society*, 117(19):5179–5197.

Cosgrove, D. J. (2005). Growth of the plant cell wall. *Nature Reviews Molecular Cell Biology*, 6(11):850–861.

Cosgrove, D. J. (2014). Re-constructing our models of cellulose and primary cell wall assembly. *Current Opinion in Plant Biology*, 22:122–131.

Cosgrove, D. J. (2018a). Diffuse growth of plant cell walls. *Plant Physiology*, 176(1):16–27.

Cosgrove, D. J. (2018b). Nanoscale structure, mechanics and growth of epidermal cell walls. *Current Opinion in Plant Biology*, 46:77–86.

Damián, S. (2013). *An Extended Mixture Model for the Simultaneous Treatment of Short and Long Scale Interfaces*. Doctoral thesis, National University of the Littoral.

Damm, W., Frontera, A., Tirado-Rives, J., and Jorgensen, W. L. (1997). OPLS all-atom force field for carbohydrates. *Journal of Computational Chemistry*, 18(16):1955–1970.

Darden, T., York, D., and Pedersen, L. (1993). Particle mesh Ewald: An N log(N) method for Ewald sums in large systems. *The Journal of Chemical Physics*.

De France, K. J., Hoare, T., and Cranston, E. D. (2017). Review of hydrogels and aerogels containing nanocellulose. *Chemistry of Materials*, 29(11):4609–4631.

Dhyani, V. and Bhaskar, T. (2018). A comprehensive review on the pyrolysis of lignocellulosic biomass. *Renewable Energy*, 129:695–716.

Ding, S. Y., Zhao, S., and Zeng, Y. (2014). Size, shape, and arrangement of native cellulose fibrils in maize cell walls.

Donaldson, L. (2007). Cellulose microfibril aggregates and their size variation with cell wall type. *Wood Science and Technology*, 41(5):443–460.

Donaldson, L. (2008). Microfibril angle: Measurement, variation and relationships—a review. *IAWA Journal*, 29(4):345–386.

Dong, X. M. and Gray, D. G. (1997). Induced circular dichroism of isotropic and magnetically-oriented chiral nematic suspensions of cellulose crystallites. *Langmuir*, 13(11):3029–3034.

Dri, F. L., Wu, X., Moon, R. J., Martini, A., and Zavattieri, P. D. (2015). Evaluation of reactive force fields for prediction of the thermo-mechanical properties of cellulose I$_\beta$. *Computational Materials Science*, 109:330–340.

Edelsbrunner, H. and Mücke, E. P. (1994). Three-dimensional alpha shapes. *ACM Transactions on Graphics*, 13(1):43–72.

Elazzouzi-Hafraoui, S., Nishiyama, Y., Putaux, J.-L., Heux, L., Dubreuil, F., and Rochas, C. (2008). The shape and size distribution of crystalline nanoparticles prepared by acid hydrolysis of native cellulose. *Biomacromolecules*, 9(1):57–65.

Ewald, P. P. (1921). Die berechnung optischer und elektrostatischer gitterpotentiale. *Annalen der Physik*, 369(3):253–287.

Fahlén, J. and Salmén, L. (2003). Cross-sectional structure of the secondary wall of wood fibers as affected by processing. *Journal of Materials Science*, 38(1):119–126.

Fahlén, J. and Salmén, L. (2005). Pore and matrix distribution in the fiber wall revealed by atomic force microscopy and image analysis. *Biomacromolecules*, 6(1):433–438.

Fall, A. B., Lindstrom, S. B., Sundman, O., Odberg, L., and Wagberg, L. (2011). Colloidal stability of aqueous nanofibrillated cellulose dispersions. *Langmuir*, 27(18):11332–11338.

Fernandes, A. N., Thomas, L. H., Altaner, C. M., Callow, P., Forsyth, V. T., Apperley, D. C., Kennedy, C. J., and Jarvis, M. C. (2011). Nanostructure of cellulose microfibrils in spruce wood. *Proceedings of the National Academy of Sciences*, 108(47):E1195–E1203.

Ferziger, J. H. and Perić, M. (1996). *Computational Methods for Fluid Dynamics*. Springer Berlin Heidelberg, Heidelberg.

Figueras, J. (1996). Ring perception using breadth-first search. *Journal of Chemical Information and Computer Sciences*, 36(5):986–991.

Foley, B. L., Tessier, M. B., and Woods, R. J. (2012). Carbohydrate force fields. *Wiley Interdisciplinary Reviews: Computational Molecular Science*, 2(4):652–697.

French, A. D. (2017). Glucose, not cellobiose, is the repeating unit of cellulose and why that is important. *Cellulose*, 24(11):4605–4609.

Frenkel, D. and Smit, B. (2002). *Understanding Molecular Simulation*. Elsevier, San Diego, 2nd edition.

Fukuzumi, H., Tanaka, R., Saito, T., and Isogai, A. (2014). Dispersion stability and aggregation behavior of TEMPO-oxidized cellulose nanofibrils in water as a function of salt addition. *Cellulose*, 21(3):1553–1559.

Gibson, L. J. (2012). The hierarchical structure and mechanics of plant materials. *Journal of The Royal Society Interface*, 9(76):2749–2766.

Grantham, N. J., Wurman-Rodrich, J., Terrett, O. M., Lyczakowski, J. J., Stott, K., Iuga, D., Simmons, T. J., Durand-Tardif, M., Brown, S. P., Dupree, R., Busse-Wicher, M., and Dupree, P. (2017). An even pattern of xylan substitution is critical for interaction with cellulose in plant cell walls. *Nature Plants*, 3(11):859–865.

Habibi, Y., Lucia, L. A., and Rojas, O. J. (2010). Cellulose nanocrystals: Chemistry, self-assembly, and applications. *Chemical Reviews*, 110(6):3479–3500.

Hadden, J. A., French, A. D., and Woods, R. J. (2013). Unraveling cellulose microfibrils: A twisted tale. *Biopolymers*, 99(10):746–756.

Hairer, E., Lubich, C., and Wanner, G. (2006). *Geometric Numerical Integration*, volume 31 of *Springer Series in Computational Mathematics*. Springer-Verlag, Berlin/Heidelberg.

Hallac, B. B. and Ragauskas, A. J. (2011). Analyzing cellulose degree of polymerization and its relevancy to cellulosic ethanol. *Biofuels, Bioprod. Bioref.*, 5:215–225.

Hanley, S. J., Revol, J. F., Godbout, L., and Gray, D. G. (1997). Atomic force microscopy and transmission electron microscopy of cellulose from micrasterias denticulata; evidence for a chiral helical microfibril twist. *Cellulose*, 4:209.

Harrison, J. A., Schall, J. D., Maskey, S., Mikulski, P. T., Knippenberg, M. T., and Morrow, B. H. (2018). Review of force fields and intermolecular potentials used in atomistic computational materials research. *Applied Physics Reviews*, 5(3):031104.

Heinze, T., El Seoud, O. A., and Koschella, A. (2018). *Cellulose Derivatives: Synhtesis, Structure and Properties*. Springer.

Herth, W. (1983). Arrays of plasma-membrane "rosettes" involved in cellulose microfibril formation of Spirogyra. *Planta*, 159(4):347–356.

Hess, B., Bekker, H., Berendsen, H. J. C., and Fraaije, J. G. E. M. (1997). LINCS: A linear constraint solver for molecular simulations. *Journal of Computational Chemistry*, 18(12):1463–1472.

Hidayat, B. J., Felby, C., Johansen, K. S., and Thygesen, L. G. (2012). Cellulose is not just cellulose: A review of dislocations as reactive sites in the enzymatic hydrolysis of cellulose microfibrils. *Cellulose*, 19(5):1481–1493.

Himmel, M. E., Park, S., Johnson, D. K., Baker, J. O., and Parilla, P. A. (2010). Cellulose crystallinity index: measurement techniques and their impact on interpreting cellulase performance. *Biotechnology for Biofuels*, 3(1):10.

Hirt, C. and Nichols, B. (1981). Volume of fluid (VOF) method for the dynamics of free boundaries. *Journal of Computational Physics*, 39(1):201–225.

Hockney, R. W. (1970). The potential calculation and some applications. *Methods in Computational Physics*, 9:136–211.

Hockney, R. W. and Eastwood, J. W. (1988). *Computer simulation using particles*. CRC Press.

Hoeng, F., Denneulin, A., and Bras, J. (2016). Use of nanocellulose in printed electronics: a review. *Nanoscale*, 8(27):13131–13154.

Hoover, W. G. (1985). Canonical dynamics: Equilibrium phase-space distributions. *Physical Review A*, 31(3):1695–1697.

Hosoya, T. and Sakaki, S. (2013). Levoglucosan formation from crystalline cellulose: Importance of a hydrogen bonding network in the reaction. *ChemSusChem*, 6(12):2356–2368.

Hub, J. S., de Groot, B. L., and van der Spoel, D. (2010). g_wham: A free weighted histogram analysis implementation including robust error and autocorrelation estimates. *Journal of Chemical Theory and Computation*, 6(12):3713–3720.

Hubbe, M. A., Ferrer, A., Tyagi, P., Yin, Y., Salas, C., Pal, L., and Rojas, O. J. (2017). Nanocellulose in thin films, coatings, and plies for packaging applications: A review. *BioResources*, 12(1):2143–2233.

Huber, G. W., Iborra, S., and Corma, A. (2006). Synthesis of transportation fuels from biomass: Chemistry, catalysts, and engineering. *Chemical Reviews*, 106(9):4044–4098.

ISO/TS 20477:2017 (2017). Nanotechnologies—standard terms and their definition for cellulose nanomaterial. Standard, International Organization for Standardization, Geneva.

Jarvis, M. C. (2013). Cellulose biosynthesis: Counting the chains. *Plant Physiology*, 163:1485–1486.

Jarvis, M. C. (2018). Structure of native cellulose microfibrils, the starting point for nanocellulose manufacture. *Philosophical transactions. Series A, Mathematical, physical, and engineering sciences*, 376(2112):20170045.

Jones, J. E. (1924). On the determination of molecular fields. II. from the equation of state of a gas. *Proceedings of the Royal Society A: Mathematical, Physical and Engineering Sciences*, 106(738):463–477.

Jorfi, M. and Foster, E. J. (2015). Recent advances in nanocellulose for biomedical applications. *Journal of Applied Polymer Science*, 132(14).

Jorgensen, W. L., Chandrasekhar, J., Madura, J. D., Impey, R. W., and Klein, M. L. (1983). Comparison of simple potential functions for simulating liquid water. *The Journal of Chemical Physics*, 79(2):926–935.

Jorgensen, W. L., Damm, W., Frontera, A., and Lamb, M. L. (1996a). Molecular recognition of carbohydrates: Interaction of diols with acetate ion. *NATO ASI Ser. C*, 485:115–126.

Jorgensen, W. L., Madura, J. D., and Swenson, C. J. (1984). Optimized intermolecular potential functions for liquid hydrocarbons. *Journal of the American Chemical Society*, 106(22):6638–6646.

Jorgensen, W. L., Maxwell, D. S., and Tirado-Rives, J. (1996b). Development and testing of the OPLS all-atom force field on conformational energetics and properties of organic liquids. *Journal of the American Chemical Society*, 118(45):11225–11236.

Kannam, S. K., Oehme, D. P., Doblin, M. S., Gidley, M. J., Bacic, A., and Downton, M. T. (2017). Hydrogen bonds and twist in cellulose microfibrils. *Carbohydrate Polymers*, 175:433–439.

Kaplan, I. G. (2006). *Intermolecular Interactions: Physical Picture, Computational Methods and Model Potentials*, volume 121. John Wiley & Sons, Ltd, Chichester, UK.

Kargarzadeh, H., Mariano, M., Gopakumar, D., Ahmad, I., Thomas, S., Dufresne, A., Huang, J., and Lin, N. (2018). *Advances in cellulose nanomaterials*, volume 25. Springer Netherlands.

Kargarzadeh, H., Mariano, M., Huang, J., Lin, N., Ahmad, I., Dufresne, A., and Thomas, S. (2017). Recent developments on nanocellulose reinforced polymer nanocomposites: A review. *Polymer*, 132:368–393.

Kästner, J. (2011). Umbrella sampling. *Wiley Interdisciplinary Reviews: Computational Molecular Science*, 1(6):932–942.

Khandelwal, M. and Windle, A. (2014). Origin of chiral interactions in cellulose supramolecular microfibrils. *Carbohydrate Polymers*, 106:128–131.

Klemm, D., Heublein, B., Fink, H. P., and Bohn, A. (2005). Cellulose: Fascinating biopolymer and sustainable raw material. *Angewandte Chemie - International Edition*, 44(22):3358–3393.

Kony, D., Damm, W., Stoll, S., and Van Gunsteren, W. F. (2002). An improved OPLS-AA force field for carbohydrates. *Journal of Computational Chemistry*, 23(15):1416–1429.

Kucińska-Lipka, J., Gubanska, I., and Janik, H. (2015). Bacterial cellulose in the field of wound healing and regenerative medicine of skin: recent trends and future prospectives. *Polymer Bulletin*, 72(9):2399–2419.

Kumar, S., Rosenberg, J. M., Bouzida, D., Swendsen, R. H., and Kollman, P. A. (1992). The weighted histogram analysis method for free-energy calculations on biomolecules. I. the method. *Journal of Computational Chemistry*, 13(8):1011–1021.

Kumar, V., Elfving, A., Koivula, H., Bousfield, D., and Toivakka, M. (2016). Roll-to-roll processed cellulose nanofiber coatings. *Industrial and Engineering Chemistry Research*, 55(12):3603–3613.

Lampugnani, E. R., Khan, G. A., Somssich, M., and Persson, S. (2018). Building a plant cell wall at a glance. *Journal of Cell Science*, 131(2):6.

Launder, B. and Spalding, D. (1974). The numerical computation of turbulent flows. *Computer Methods in Applied Mechanics and Engineering*, 3(2):269–289.

Law, R. C. (2004). Cellulose acetate in textile application. *Macromolecular Symposia*, 208(1):255–266.

Leach, A. R. (2001). *Molecular Modelling: Principles and Applications*. Pearson Education Ltd, Harlow, 2nd edition.

Lédé, J. (2012). Cellulose pyrolysis kinetics: An historical review on the existence and role of intermediate active cellulose. *Journal of Analytical and Applied Pyrolysis*, 94:17–32.

Lehtiö, J., Sugiyama, J., Gustavsson, M., Fransson, L., Linder, M., and Teeri, T. T. (2003). The binding specificity and affinity determinants of family 1 and family 3 cellulose binding modules. *Proceedings of the National Academy of Sciences*, 100(2):484–489.

Leng, E., Costa, M., Peng, Y., Zhang, Y., Gong, X., Zheng, A., Huang, Y., and Xu, M. (2018). Reactivity of cellulose reducing end in pyrolysis as studied by methyl glucoside-impregnation. *Combustion and Flame*, 96(7):267–277.

Lengowski, E. C., Bonfatti, E. A. J., Kumode, M. M. N., Carneiro, M. E., and Satyanarayana, K. G. (2019). Nanocellulose in the paper making. In Inamuddin, Mishra, R. K., Thomas, S., and Asiri, A. M., editors, *Sustainable Polymer Composites and Nanocomposites*, pages 1027–1066. Springer, Cham.

Lin, N. and Dufresne, A. (2014). Nanocellulose in biomedicine: Current status and future prospect. *European Polymer Journal*, 59:302–325.

Lin, Y.-C., Cho, J., Tompsett, G., Westmoreland, P. R., and Huber, G. W. (2009). Kinetics and mechanism of cellulose pyrolysis. *Journal of Physical Chemistry C*, 113(46):20097–20107.

Liu, C., Huang, J., Huang, X., Li, H., and Zhang, Z. (2011). Theoretical studies on formation mechanisms of CO and CO_2 in cellulose pyrolysis. *Computational and Theoretical Chemistry*, 964(1-3):207–212.

Lovikka, V. A., Khanjani, P., Väisänen, S., Vuorinen, T., and Maloney, T. C. (2016). Porosity of wood pulp fibers in the wet and highly open dry state. *Microporous and Mesoporous Materials*, 234:326–335.

Majoinen, J., Haataja, J. S., Appelhans, D., Lederer, A., Olszewska, A., Seitsonen, J., Aseyev, V., Kontturi, E., Rosilo, H., Österberg, M., Houbenov, N., and Ikkala, O. (2014). Supra-colloidal multivalent interactions and wrapping of dendronized glycopolymers on native cellulose nanocrystals. *Journal of the American Chemical Society*, 136(3):866–869.

Mamleev, V., Bourbigot, S., Le Bras, M., Yvon, J., and Lefebvre, J. (2006). Model-free method for evaluation of activation energies in modulated thermogravimetry and analysis of cellulose decomposition. *Chemical Engineering Science*, 61(4):1276–1292.

Marriott, P. E., Gómez, L. D., and Mcqueen-Mason, S. J. (2016). Unlocking the potential of lignocellulosic biomass through plant science. *New Phytologist*, 209(4):1366–1381.

MathWorks Inc. (2010). Matlab version 7.10.0 (R2010a).

Matsuoka, S., Kawamoto, H., and Saka, S. (2011). Reducing end-group of cellulose as a reactive site for thermal discoloration. *Polymer Degradation and Stability*, 96(7):1242–1247.

Matthews, J. F., Beckham, G. T., Bergenstrahle-Wohlert, M., Brady, J. W., Himmel, M. E., and Crowley, M. F. (2012). Comparison of cellulose iβ simulations with three carbohydrate force fields. *Journal of Chemical Theory and Computation*, 8(2):735–748.

Matthews, J. F., Skopec, C. E., Mason, P. E., Zuccato, P., Torget, R. W., Sugiyama, J., Himmel, M. E., and Brady, J. W. (2006). Computer simulation studies of microcrystalline cellulose I$_\beta$. *Carbohydrate Research*, 341(1):138–152.

Mattsson, T. R., Lane, J. M. D., Cochrane, K. R., Desjarlais, M. P., Thompson, A. P., Pierce, F., and Grest, G. S. (2010). First-principles and classical molecular dynamics simulation of shocked polymers. *Physical Review B*, 81(5):054103.

Mayes, H. B. and Broadbelt, L. J. (2012). Unraveling the reactions that unravel cellulose. *Journal of Physical Chemistry A*, 116(26):7098–7106.

McFarlane, H. E., Döring, A., and Persson, S. (2014). The cell biology of cellulose synthesis. *Annual Review of Plant Biology*.

McGrattan, K. and Miles, S. (2016). Modeling fires using computational fluid dynamics (CFD). In *SFPE Handbook of Fire Protection Engineering*, pages 1034–1065. Springer New York, New York, NY.

McNamara, J. T., Morgan, J. L. W., and Zimmer, J. (2015). A molecular description of cellulose biosynthesis. *Annual Review of Biochemistry*, 84:895–921.

Mettler, M. S., Mushrif, S. H., Paulsen, A. D., Javadekar, A. D., Vlachos, D. G., and Dauenhauer, P. J. (2012a). Revealing pyrolysis chemistry for biofuels production: Conversion of cellulose to furans and small oxygenates. *Energy and Environmental Science*, 5(1):5414–5424.

Mettler, M. S., Vlachos, D. G., and Dauenhauer, P. J. (2012b). Top ten fundamental challenges of biomass pyrolysis for biofuels. *Energy and Environmental Science*, 5(7):7797–7809.

Mewis, J. and Wagner, N. J. (2009). Thixotropy. *Advances in Colloid and Interface Science*, 147-148(C):214–227.

Miller, J. and Bodart, A.-C. (2014). Nanocellulose: Technology, applications and markets. Technical report, RISI Inc.

Miyamoto, S. and Kollman, P. A. (1992). Settle: An analytical version of the SHAKE and RATTLE algorithm for rigid water models. *Journal of Computational Chemistry*, 13(8):952–962.

Mo, Y., Wu, W., Song, L., Lin, M., Zhang, Q., and Gao, J. (2004). The magnitude of hyperconjugation in ethane: A perspective from ab initio valence bond theory. *Angewandte Chemie International Edition*, 43(15):1986–1990.

Moon, R. J., Martini, A., Nairn, J., Simonsen, J., and Youngblood, J. (2011). Cellulose nanomaterials review: structure, properties and nanocomposites. *Chemical Society Reviews*, 40(7):3941.

Morse, P. M. (1929). Diatomic molecules according to the wave mechanics. II. vibrational levels. *Physical Review*, 34(1):57–64.

Mortier, W. J., Ghosh, S. K., and Shankar, S. (1986). Electronegativity-equalization method for the calculation of atomic charges in molecules. *Journal of the American Chemical Society*, 108(15):4315–4320.

Müller, M., Öztürk, E., Arlov, Ø., Gatenholm, P., and Zenobi-Wong, M. (2017). Alginate sulfate–nanocellulose bioinks for cartilage bioprinting applications. *Annals of Biomedical Engineering*, 45(1):210–223.

Murillo, J. D., Moffet, M., Biernacki, J. J., and Northrup, S. (2015). High-temperature molecular dynamics simulation of cellobiose and maltose. *AIChE Journal*, 61(8):2562–2570.

Niinivaara, E., Faustini, M., Tammelin, T., and Kontturi, E. (2015). Water vapor uptake of ultrathin films of biologically derived nanocrystals: Quantitative assessment with quartz crystal microbalance and spectroscopic ellipsometry. *Langmuir*, 31(44):12170–12176.

Nishiyama, Y. (2018). Molecular interactions in nanocellulose assembly. *Philosophical Transactions of the Royal Society A: Mathematical, Physical and Engineering Sciences*, 376(2112):20170047.

Nishiyama, Y., Johnson, G. P., French, A. D., Forsyth, V. T., and Langan, P. (2008). Neutron crystallography, molecular dynamics, and quantum mechanics studies of the nature of hydrogen bonding in cellulose I$_\beta$. *Biomacromolecules*, 9(11):3133–3140.

Nishiyama, Y., Kim, U.-J., Kim, D.-Y., Katsumata, K. S., May, R. P., and Langan, P. (2003a). Periodic disorder along ramie cellulose microfibrils. *Biomacromolecules*, 4(4):1013–1017.

Nishiyama, Y., Langan, P., and Chanzy, H. (2002). Crystal structure and hydrogen-bonding system in cellulose I$_\beta$ from synchrotron x-ray and neutron fiber diffraction. *Journal of the American Chemical Society*, 124(31):9074–9082.

Nishiyama, Y., Sugiyama, J., Chanzy, H., and Langan, P. (2003b). Crystal structure and hydrogen bonding system in cellulose I$_\alpha$ from synchrotron x-ray and neutron fiber diffraction. *Journal of the American Chemical Society*, 125(47):14300–14306.

Niskanen, K. (2008). *Paper Physics*. "Paper physics", ed. K. Niskanen, Finnish Paper Engineers' Association/Paperi ja Puu Oy, 2nd edition.

Nixon, B. T., Mansouri, K., Singh, A., Du, J., Davis, J. K., Lee, J. G., Slabaugh, E., Vandavasi, V. G., O'Neill, H., Roberts, E. M., Roberts, A. W., Yingling, Y. G., and Haigler, C. H. (2016). Comparative structural and computational analysis supports eighteen cellulose synthases in the plant cellulose synthesis complex. *Scientific Reports*, 6:28696.

O'Boyle, N. M., Banck, M., James, C. A., Morley, C., Vandermeersch, T., and Hutchison, G. R. (2011). Open Babel: An open chemical toolbox. *Journal of cheminformatics*, 3(1):33.

Oehme, D. P., Doblin, M. S., Wagner, J., Bacic, A., Downton, M. T., and Gidley, M. J. (2015). Gaining insight into cell wall cellulose macrofibril organisation by simulating microfibril adsorption. *Cellulose*, 22(6):3501–3520.

Oehme, D. P., Yang, H., and Kubicki, J. D. (2018). An evaluation of the structures of cellulose generated by the CHARMM force field: comparisons to in planta cellulose. *Cellulose*, 25(7):1–23.

Ogawa, Y. (2019). Electron microdiffraction reveals the nanoscale twist geometry of cellulose nanocrystals. *Nanoscale*, 11(45):21767–21774.

Orlowski, A., Róg, T., Paavilainen, S., Manna, M., Heiskanen, I., Backfolk, K., Timonen, J., and Vattulainen, I. (2015). How endoglucanase enzymes act on cellulose nanofibrils: role of amorphous regions revealed by atomistic simulations. *Cellulose*, 22(5):2911–2925.

Paajanen, A., Sonavane, Y., Ignasiak, D., Ketoja, J. A., Maloney, T., and Paavilainen, S. (2016). Atomistic molecular dynamics simulations on the interaction of TEMPO-oxidized cellulose nanofibrils in water. *Cellulose*, 23(6):3449–3462.

Paajanen, A. and Vaari, J. (2017). High-temperature decomposition of the cellulose molecule: a stochastic molecular dynamics study. *Cellulose*, 24(7):2713–2725.

Paavilainen, S., McWhirter, J. L., Róg, T., Järvinen, J., Vattulainen, I., and Ketoja, J. A. (2012). Mechanical properties of cellulose nanofibrils determined through atomistic molecular dynamics simulations. *Nordic Pulp & Paper Research Journal*, 27(2):282–286.

Paavilainen, S., Róg, T., and Vattulainen, I. (2011). Analysis of twisting of cellulose nanofibrils in atomistic molecular dynamics simulations. *The Journal of Physical Chemistry B*, 115(14):3747–3755.

Payen, A. (1838). Mémoire sur la composition du tissu propre des plantes et du ligneux. *C R Hebd Séances Acad Sci.*, 7:1062–56.

Payne, C. M., Knott, B. C., Mayes, H. B., Hansson, H., Himmel, M. E., Sandgren, M., Stahlberg, J., and Beckham, G. T. (2015). Fungal cellulases. *Chemical Reviews*, 115(3):1308–1448.

Plimpton, S. (1995). Fast parallel algorithms for short-range molecular dynamics. *Journal of Computational Physics*, 117(1):1–19.

Pouwels, A. D., Eijkel, G. B., Arisz, P. W., and Boon, J. J. (1989). Evidence for oligomers in pyrolysates of microcrystalline cellulose. *Journal of Analytical and Applied Pyrolysis*, 15:71–84.

Price, M. L. P., Ostrovsky, D., and Jorgensen, W. L. (2001). Gas-phase and liquid-state properties of esters, nitriles, and nitro compounds with the OPLS-AA force field. *Journal of Computational Chemistry*, 22(13):1340–1352.

Pronk, S., Páll, S., Schulz, R., Larsson, P., Bjelkmar, P., Apostolov, R., Shirts, M. R., Smith, J. C., Kasson, P. M., van der Spoel, D., Hess, B., and Lindahl, E. (2013). GROMACS 4.5: a high-throughput and highly parallel open source molecular simulation toolkit. *Bioinformatics (Oxford, England)*, 29(7):845–54.

Prosperetti, A. and Tryggvason, G., editors (2007). *Computational Methods for Multiphase Flow*. Cambridge University Press, Cambridge.

Rahaman, O., van Duin, A. C. T., Goddard, W. A., and Doren, D. J. (2011). Development of a ReaxFF reactive force field for glycine and application to solvent effect and tautomerization. *The Journal of Physical Chemistry B*, 115(2):249–261.

Rappe, A. K. and Goddard, W. A. (1991). Charge equilibration for molecular dynamics simulations. *The Journal of Physical Chemistry*, 95(8):3358–3363.

Reza, M., Bertinetto, C., Ruokolainen, J., and Vuorinen, T. (2017). Cellulose elementary fibrils assemble into helical bundles in S1 layer of spruce tracheid wall. *Biomacromolecules*, 18(2):374–378.

Ryckaert, J.-P., Ciccotti, G., and Berendsen, H. J. (1977). Numerical integration of the cartesian equations of motion of a system with constraints: molecular dynamics of n-alkanes. *Journal of Computational Physics*, 23(3):327–341.

Saito, T., Hirota, M., Tamura, N., Kimura, S., Fukuzumi, H., Heux, L., and Isogai, A. (2009). Individualization of nano-sized plant cellulose fibrils by direct surface carboxylation using TEMPO catalyst under neutral conditions. *Biomacromolecules*, 10(7):1992–1996.

Saito, T. and Isogai, A. (2004). TEMPO-mediated oxidation of native cellulose. the effect of oxidation conditions on chemical and crystal structures of the water-insoluble fractions. *Biomacromolecules*, 5(5):1983–1989.

Saito, T., Kimura, S., Nishiyama, Y., and Isogai, A. (2007). Cellulose nanofibers prepared by TEMPO-mediated oxidation of native cellulose. *Biomacromolecules*, 8(8):2485–2491.

Saito, T., Nishiyama, Y., Putaux, J.-L. L., Vignon, M., and Isogai, A. (2006). Homogeneous suspensions of individualized microfibrils from TEMPO-catalyzed oxidation of native cellulose. *Biomacromolecules*, 7(6):1687–91.

Schlick, T. (2010). *Molecular Modeling and Simulation: An Interdisciplinary Guide*, volume 21 of *Interdisciplinary Applied Mathematics*. Springer New York, New York, NY.

Schrödinger LLC (2015). The PyMOL molecular graphics system, version 1.8.

Senftle, T. P., Hong, S., Islam, M. M., Kylasa, S. B., Zheng, Y., Shin, Y. K., Junkermeier, C., Engel-Herbert, R., Janik, M. J., Aktulga, H. M., Verstraelen, T., Grama, A., and van Duin, A. C. T. (2016). The ReaxFF reactive force-field: development, applications and future directions. *npj Computational Materials*, 2:15011.

Shinoda, W., Shiga, M., and Mikami, M. (2004). Rapid estimation of elastic constants by molecular dynamics simulation under constant stress. *Physical Review B*, 69(13):134103.

Shklyaev, O. E., Kubicki, J. D., Watts, H. D., and Crespi, V. H. (2014). Constraints on I_β cellulose twist from *dft* calculations 13C NMR chemical shifts. *Cellulose*, 21(6):3979–3991.

Staudinger, H. (1920). Über polymerisation. *Ber Dtsch Chem Ges*, 53:1073–1085.

Steinbach, P. J. and Brooks, B. R. (1994). New spherical-cutoff methods for long-range forces in macromolecular simulation. *Journal of Computational Chemistry*, 15(7):667–683.

Stuart, S. J., Tutein, A. B., and Harrison, J. A. (2000). A reactive potential for hydrocarbons with intermolecular interactions. *The Journal of Chemical Physics*, 112(14):6472–6486.

Stukowski, A. (2010). Visualization and analysis of atomistic simulation data with OVITO— the open visualization tool. *Modelling and Simulation in Materials Science and Engineering*, 18(1).

Sun, X., Wu, Q., Lee, S., Qing, Y., and Wu, Y. (2016). Cellulose nanofibers as a modifier for rheology, curing and mechanical performance of oil well cement. *Scientific Reports*, 6(1):31654.

Swope, W. C., Andersen, H. C., Berens, P. H., and Wilson, K. R. (1982). A computer simulation method for the calculation of equilibrium constants for the formation of physical clusters of molecules: Application to small water clusters. *The Journal of Chemical Physics*, 76(1):637–649.

Ten Bosch, A. (1996). On the chirality of paper. *Macromolecular Theory and Simulations*, 5(2):225–230.

Thomas, B., Raj, M. C., B, A. K., H, R. M., Joy, J., Moores, A., Drisko, G. L., and Sanchez, C. (2018). Nanocellulose, a versatile green platform: From biosources to materials and their applications. *Chemical Reviews*, 118(24):11575–11625.

Thomas, L. H., Forsyth, V. T., Sturcova, A., Kennedy, C. J., May, R. P., Altaner, C. M., Apperley, D. C., Wess, T. J., and Jarvis, M. C. (2013). Structure of cellulose microfibrils in primary cell walls from collenchyma. *Plant Physiology*, 161(1):465–476.

Tobias, D. J., Martyna, G. J., and Klein, M. L. (1993). Molecular dynamics simulations of a protein in the canonical ensemble. *The Journal of Physical Chemistry*, 97(49):12959–12966.

Torrie, G. M. and Valleau, J. P. (1977). Nonphysical sampling distributions in Monte Carlo free-energy estimation: Umbrella sampling. *Journal of Computational Physics*, 23(2):187–199.

Tuckerman, M., Berne, B. J., and Martyna, G. J. (1992). Reversible multiple time scale molecular dynamics. *The Journal of Chemical Physics*, 97(3):1990–2001.

Turpeinen, T., Jäsberg, A., Haavisto, S., Liukkonen, J., Salmela, J., and Koponen, A. I. (2019). Pipe rheology of microfibrillated cellulose suspensions. *Cellulose*, doi: 10.1007/s10570-019-02784-4.

Usov, I., Nyström, G., Adamcik, J., Handschin, S., Schütz, C., Fall, A., Bergström, L., and Mezzenga, R. (2015). Understanding nanocellulose chirality and structure-properties relationship at the single fibril level. *Nature Communications*, 6:7564.

Vadodaria, S. S., Onyianta, A. J., and Sun, D. (2018). High-shear rate rheometry of micro-nanofibrillated cellulose (cmf/cnf) suspensions using rotational rheometer. *Cellulose*, 25(10):5535–5552.

Väisänen, S., Pönni, R., Hämäläinen, A., and Vuorinen, T. (2018). Quantification of accessible hydroxyl groups in cellulosic pulps by dynamic vapor sorption with deuterium exchange. *Cellulose*, 25(12):6923–6934.

Van Duin, A. C. T., Dasgupta, S., Lorant, F., and Goddard, W. A. (2001). ReaxFF: A reactive force field for hydrocarbons. *Journal of Physical Chemistry A*, 105(41):9396–9409.

Vandavasi, V. G., Putnam, D. K., Zhang, Q., Petridis, L., Heller, W. T., Nixon, B. T., Haigler, C. H., Kalluri, U., Coates, L., Langan, P., Smith, J. C., Meiler, J., and O'Neill, H. (2016). A structural study of cesa1 catalytic domain of arabidopsis cellulose synthesis complex: Evidence for cesa trimers. *Plant Physiology*, 170(1):123–135.

Várhegyi, G., Jakab, E., and Antal, M. J. (1994). Is the Broido-Shafizadeh model for cellulose pyrolysis true? *Energy and Fuels*, 8(6):1345–1352.

Vinu, R. and Broadbelt, L. J. (2012). A mechanistic model of fast pyrolysis of glucose-based carbohydrates to predict bio-oil composition. *Energy and Environmental Science*, 5(12):9808–9826.

Wang, J.-S., Wang, G., Feng, X.-Q., Kitamura, T., Kang, Y.-L., Yu, S.-W., and Qin, Q.-H. (2013). Hierarchical chirality transfer in the growth of towel gourd tendrils. *Scientific Reports*, 3(1):3102.

Wang, S., Lu, A., and Zhang, L. (2016). Recent advances in regenerated cellulose materials. *Progress in Polymer Science*, 53:169–206.

Wang, T. and Hong, M. (2016). Solid-state NMR investigations of cellulose structure and interactions with matrix polysaccharides in plant primary cell walls.

White, J. E., Catallo, W. J., and Legendre, B. L. (2011). Biomass pyrolysis kinetics: A comparative critical review with relevant agricultural residue case studies. *Journal of Analytical and Applied Pyrolysis*, 91(1):1–33.

Wiedenhoeft, A. C. (2013). Structure and function of wood. In *Handbook of Wood Chemistry and Wood Composites*, chapter 2, pages 9–32. 2nd edition.

Yu, M., Abitbol, T., and Gray, D. G. (2004). Evidence for a chiral internal stress in paper sheets. *Journal of Pulp and Paper Science*, 30(4):91–94.

Yui, T. and Hayashi, S. (2007). Molecular dynamics simulations of solvated crystal models of cellulose I_α and III_I. *Biomacromolecules*, 8(3):817–824.

Yui, T., Nishimura, S., Akiba, S., and Hayashi, S. (2006). Swelling behavior of the cellulose I$_\beta$ crystal models by molecular dynamics. *Carbohydr Res*, 341(15):2521–2530.

Zaman, M., Liu, H., Xiao, H., Chibante, F., and Ni, Y. (2013). Hydrophilic modification of polyester fabric by applying nanocrystalline cellulose containing surface finish. *Carbohydrate Polymers*, 91(2):560–567.

Zhang, M., Geng, Z., and Yu, Y. (2015a). Density functional theory (dft) study on the pyrolysis of cellulose: The pyran ring breaking mechanism. *Computational and Theoretical Chemistry*, 1067:13–23.

Zhang, T., Li, X., Qiao, X., Zheng, M., Guo, L., Song, W., and Lin, W. (2016a). Initial mechanisms for an overall behavior of lignin pyrolysis through large-scale ReaxFF molecular dynamics simulations. *Energy and Fuels*, 30(4):3140–3150.

Zhang, T., Zheng, Y., and Cosgrove, D. J. (2016b). Spatial organization of cellulose microfibrils and matrix polysaccharides in primary plant cell walls as imaged by multichannel atomic force microscopy. *Plant Journal*, 85(2):179–192.

Zhang, X., Li, J., Yang, W., and Blasiak, W. (2011). Formation mechanism of levoglucosan and formaldehyde during cellulose pyrolysis. *Energy and Fuels*, 25(8):3739–3746.

Zhang, Y., Liu, C., and Chen, X. (2015b). Unveiling the initial pyrolytic mechanisms of cellulose by DFT study. *Journal of Analytical and Applied Pyrolysis*, 113:621–629.

Zhang, Y., Liu, C., and Xie, H. (2014). Mechanism studies on β-d-glucopyranose pyrolysis by density functional theory methods. *Journal of Analytical and Applied Pyrolysis*, 105:23–34.

Zhao, Y. and Li, J. (2014). Excellent chemical and material cellulose from tunicates: diversity in cellulose production yield and chemical and morphological structures from different tunicate species. *Cellulose*, 21(5):3427–3441.

Zhao, Z., Shklyaev, O. E., Nili, A., Mohamed, M. N. A., Kubicki, J. D., Crespi, V. H., and Zhong, L. (2013). Cellulose microfibril twist, mechanics, and implication for cellulose biosynthesis. *The Journal of Physical Chemistry A*, 117(12):2580–2589.

Zheng, M., Wang, Z., Li, X., Qiao, X., Song, W., and Guo, L. (2016). Initial reaction mechanisms of cellulose pyrolysis revealed by ReaxFF molecular dynamics. *Fuel*, 177:130–141.

Zugenmaier, P. (2008). *Crystalline Cellulose and Derivatives*. Springer Series in Wood Science. Springer Berlin Heidelberg, Berlin, Heidelberg.